THE UNIVERSITY of ADELAIDE

Blast Analysis of Normal Concrete, High Strength Concrete and Ultra-High Performance Concrete Members

Juechun Xu

B.Eng

Thesis submitted in fulfilment of the requirements for the degree of

Doctor of Philosophy

School of Civil, Environmental and Mining Engineering

The University of Adelaide, Australia

[THIS PAGE IS INTENTIONALLY LEFT BLANK]

TABLE OF CONTENTS

Abstract

The understanding of different failure modes of reinforced concrete members is essential in the blast analysis and design of civil and defence structures. Normal concrete (NC) is a widely used material in structures; high strength concrete members (HSC) is undergoing widespread use in civil engineering and construction processes and ultra-high performance concrete (UHPC) is deemed to be a promising material due to its high ductility, impact resistance and energy absorption capacity and it has drawn intense interests for the purpose of blast resistant design of structures. This thesis contains five journal papers, which aim to extend, or produce new analytical techniques for investigating both shear and flexural failure modes of structural members made of these three kinds of materials by considering both experimental and theoretical studies. The thesis has been divided into three chapters. Chapter 1 is the introduction and problem statement of this research work. Chapter 2 contains two journal papers and it provides the absence of method for assessing direct shear failure mode of reinforced concrete (RC) members against blasts. Chapter 3 includes three journal papers, which present experimental and theoretical study of failure modes of high strength reinforced concrete (HSRC) members and ultra-high performance fibre reinforced concrete (UHPFRC) members under explosion loads. Finally, Chapter 4 presents conclusions of this research program.

The experimental investigations on behaviour of reinforced concrete structures subjected to blast loading have revealed that direct shear mechanisms play an important role in the overall response and failure mode of structures. However, most of previous studies are based on the assumption that only flexural response dominates failure mode without taking shear failure into consideration. Therefore, the first journal paper in Chapter 2 is to use single degree of freedom (SDOF) system as a tool for predicting direct shear response of blast loaded reinforced concrete members. In addition, as there are no design provisions that are available to predict shear stress to slip relationship for design of NRC members, the second journal paper assesses direct shear response of NRC members is numerically evaluated using finite element software LS-DYNA, which has not been investigated in the previous literature. The two papers in Chapter 2 provide new insights concerning the mechanics of dynamic shear failure of NRC members against blast loading.

Chapter 3 presents a blast testing program on ultra-high performance fibre reinforced concrete (UHPFRC) and high strength reinforced concrete (HSRC) columns and a one dimensional (1D) finite element model (FEM) is then adopted for further investigations, due to its inherent accuracy and stability despite its numerical efficiency. The third journal paper represented herein is devoted to investigating experimentally the mechanical properties and dynamic responses of ultra-high performance twisted steel fibre reinforced concrete and HSRC columns under both quasi-static and blast loads. Afterwards, the fourth journal paper gives a detailed investigation of the capabilities of ultra-high performance micro steel fibre reinforced concrete columns and high strength reinforced (HSRC) columns against close-in blasts. To achieve this objective, a series of blast tests were conducted to investigate the behaviour of UHPFRC columns HSRC columns subjected to blast loading. Lastly, the fifth journal paper uses 1D FEM to accurately analyse the response of UHPFRC and HSRC columns subjected to blasts.

This thesis deals with a broad range of topics in analysing the static and dynamic response of structural members including RC members, HSRC and UHPFRC columns. The static loading regimes include the direct shear response. The dynamic loading regimes include impulse loading due to real blast experiments. The failure modes under blast loading conditions have been addressed in great details both in experimental study and numerical simulations.

Statement of Originality

I certify that this work contains no material which has been accepted for the award of any other degree or diploma in my name, in any university or other tertiary institution and, to the best of my knowledge and belief, contains no material previously published or written by another person, except where due reference has been made in the text. In addition, I certify that no part of this work will, in the future, be used in a submission in my name, for any other degree or diploma in any university or other tertiary institution without the prior approval of the University of Adelaide and where applicable, any partner institution responsible for the joint-award of this degree.

I give consent to this copy of my thesis when deposited in the University Library, being made available for loan and photocopying, subject to the provisions of the Copyright Act 1968.

The author acknowledges that copyright of published works contained within this thesis resides with the copyright holder(s) of those works.

I also give permission for the digital version of my thesis to be made available on the web, via the University's digital research repository, the Library Search and also through web search engines, unless permission has been granted by the University to restrict access for a period of time.

…….. ……..……

Juechun Xu Date

Acknowledgements

My greatest appreciation goes to my supervisor, Associate Professor Chengqing Wu, for all his support, expert advice, patience, and understanding throughout my PhD studies.

I would like to thank Dr Ching-Tai Ng who was never too busy to meet with me. Thanks to him, my stay at University of Adelaide was a rich learning experience.

I would also like to thank Dr Phillip Visintin, who were always willing to provide their expertise when needed.

Also, my friends deserve my thanks and much more, they made this experience truly enjoyable and rewarding.

Finally, I dedicate this thesis to my parents, Xiangming Xu and Buke Zhang who has provided me with the confidence and support to complete my PhD journey to the best of my abilities.

List of Publications

A number of manuscripts, which have been published in, or accepted in, or submitted to, internationally recognised journals and international conferences, have been list as below.

Journal papers:

1. **Xu J.**, Wu C., and Li Z.X. (2014). "Analysis of Direct Shear Failure Mode for RC Slabs under External Explosive Loading". International Journal of Impact Engineering, 69:136-148.
2. **Xu J.**, Wu C., Li Z.X. and Ng C.T. (2015). "Numerical Analysis of Shear Transfer across an Initially Uncrack Reinforced Concrete Member". Engineering Structures, 102:296-309.
3. **Xu J.**, Wu C., Xiang H., Su Y., Li Z.X., Fang Q., Hao H., Liu Z., Zhang Y. and Li J. (2015). "Behaviour of Ultra High Performance Fibre Reinforced Concrete Columns Subjected to Blast Loading". Submitted to Engineering Structures. (tentatively accepted subject to revision)
4. **Xu J.**, Wu C., Su Y., Li Z.X. and Li J. (2015). "Experimental Study on Blast Resistance of Ultra High Performance Twisted Steel Fibre Reinforced Concrete Columns". Submitted to Cement and Concrete Composites.
5. **Xu J.**, Wu C., Li J. and Cui J. (2015). "Simplified FEM Analysis of Ultra-High Performance Fibre Reinforced Concrete Columns under Blast Loads". Submitted to Advances in Structural Engineering (Invited Special Issue paper).

Conference papers:

1. **Xu J.** and Wu C. (2012). "Analysis of the Direct Shear Failure Mode for Elastic Structural Member under External Blasts". The 6th International Composites Conference (ACUN6), 14-16 November 2012, Melbourne, Victoria, CD-ROM.
2. **Xu J.** and Wu C. (2014) "Static and Dynamic Performance of a Newly Developed Steel Fibre-reinforced Self-Compacting Concrete". The 23rd Australasian Conference on the Mechanics of Structures and Materials (ACMSM23). 9-12 December 2014, Byron Bay, Australia, pp.71-76.

3. **Xu J.** and Wu C. (2014). "Experimental Study on the Response of Ultra-High Performance Reinforced Concrete Columns under Blast Loading". The 6th International Conference on Protection of Structures against Hazards, 16-17 October 2014, Tianjing, China, CD-ROM. ***[Highly commendable paper award]***
4. **Xu J.** and Wu C. (2014). "Static and Dynamic Performance of Ultra High Performance Reinforced Concrete Columns". The 13th International Symposium on Structural Engineering (ISSE-13), 24-27 October 2014, HeFei, China, CD-ROM.
5. **Xu J.** and Wu C. (2015). "Experimental Analyses of Ultra-high performance Reinforced Concrete Columns under Blast Loading". The 11th International Conference on Shock & Impact Loads on Structure, 14-15 May 2015, Ottawa, Canada, 393-398, CD-ROM.

[THIS PAGE IS INTENTIONALLY LEFT BLANK]

Chapter 1
Introduction and Problem Statement

In the past few years, many nations have become victims of terrorism. Bombs have exploded in and around buildings in many countries, causing massive damages to civilian lives and the structure itself. In response to a potential threat of terrorist bombings against civilian structures, various defence agencies and research councils are examining design methodologies and construction techniques to protect buildings and their occupants from the threat of bombings. Generally, there are two major research aspects that cover this area in recent years: firstly, developing advanced materials for achieving superior properties such as ultra-high strength, durability, and energy absorption capacity; and the secondly, updating various techniques for analysing dynamic response of structural members subjected to blast loads.

Development of advanced concrete materials including ultra-high performance fibre reinforced concrete (UHPFRC) is one of major approaches. Normal strength concrete (NSC) is one of the most widely used materials in the world. In recent years the use of high strength concrete (HSC) due to its improved deformation behaviour and faster construction pace has increased for different structures such as bridges and high rise buildings. However, although compressive strength of HSC has a dramatic increase by its mix components, its brittleness increases as well. Most recently advanced concrete materials such as ultra-high performance fibre reinforced concrete (UHPFRC) used for critical components of blast-resistant structures is increasingly recognized.

Due to high technical requirements, high costs of manufacturing advanced concrete material and security restrictions required for full-scale blast tests, experimental research on UHPFRC is very limited. Instead of using real blast testing, nonlinear dynamic analysis is usually used to predict structural response under blasts. Techniques used for nonlinear dynamic analysis are usually divided into two categories: the first being single degree of freedom (SDOF) method; and the second being Finite Element (FE) method. The employment of SDOF system utilizes the first mode of vibration or the first few modes to predict structural response to blast loading. This approach usually requires a limited number input data and easy to implement. Due to the complexity of theoretical study in this field, this simplified method is often used for practical design purposes. However, SDOF-based approaches oversimplify the complexity of blast-

loaded RC structural members, application of this method is limited to flexural response of simple structural members such as beams and slabs, and lack of reliable predictions from SDOF-based approaches is repeatedly reported. In order to overcome limitations of the simplified methods, advanced numerical methods, such as finite element analysis can be helpful. This permits for detailed analyses of failure modes and stiffness degradation as well as time history of strains and stresses in different parts of an element. Although, such as approach allows analysis of structures with various geometries and provide accurate results under different load cases, numerical modelling of response of reinforced concrete, in particular shear mechanism is still a challenging topic for researchers. Furthermore, when considering the nonlinear dynamic analysis using FEM which typically requires the implementation of a three dimensional mesh is perceived time-consuming, requiring a large number of input parameters and, generally, demanding significant experience and knowledge to obtain reliable and realistic results, and it also produces major difficulties for practical design purposes. Therefore, a simplified 1D FEM [1] which satisfy both fast-running and provides an accurate dynamic member response can be implemented as an alternative of high cost experiments, to study the effects of different factors such as concrete strength, amount and placement of reinforcement, various geometry and boundary conditions on the response of blast loaded structure elements. The results can be used as a reference for developing the design guidelines and simplified methods for practical design purposes. In the current research, both of SDOF and 1D FEM will be applied to tackle different problems by utilizing their advantages and details will be explained in the following paragraphs.

Chapter 2 of this thesis is focusing on simulation of shear responses of normal reinforced concrete members, and two journal papers are presented in this chapter. Considerable research has been conducted on flexural responses of normal reinforced concrete (NRC) members subjected to explosions; however, in the previous studies no analytical method is used to assess and explore dynamic direct shear failure. Under highly impulsive dynamic loads, it is commonly observed that direct shear failure is a sudden and catastrophic type of failure mode in reinforced concrete structural members before flexural response is initiated. A direct shear failure mode is a premature and brittle failure mechanism where the member has no time to deflect and it also can compromise the integrity of the member and possibly causes collapse failure. As it is not straightforward to derive closed form solutions for responses of a RC member subjected to blast loading, SDOF method which provides a simple mathematical

approximation and offers relative good results is used to model direct shear failure mode at the support under blast loading. The previous SDOF method has not been thoroughly investigated to confirm whether it can account for the support slip response, causing vertical direct shear crack adjacent to the supports of RC beams and slabs subjected to blasts. Therefore, the first objective of the research is to successfully incorporate flexural responses of NRC members with the absent direct shear responses into SDOF system for improving the prediction of dynamic responses of NRC members against blast loading. For accurate simulating dynamic direct shear response of NRC members, shear transfer model is an essential element for the SDOF system. So far, the direct shear to slip model proposed by Krauthammer [2] is the only published model based on Mattock's effort and gave a complete description of the whole interface shear transfer relationship curve of reinforced concrete members, taking the compression and rate effect of dynamic loading into considerations. Although this model still re-examines by many researches currently, there is no published advanced model for describing the direct shear–slip relationship. Thus the current study attempts to investigate an effective and quick method to predict shear failure under explosions, and the Krauthammer's model is chosen to model the shear slip relationship for normal strength reinforced concrete slab under blast loading.

As discussed above, among the previous publications, there is only one empirical model for describing the shear stress to slip relationship proposed by Krauthammer et al. [2]. They presented a tri-linear direct shear resistance-slip model for RC members relied upon analysing the shear transfer in the static domain without contributions of in-plane compression on shear strength. However, this model may underestimate the value of shear strength and slip for larger specimens. This is because larger diameter bars are usually associated with larger slip at yielding [3]. In addition, the simplified tri-linear model may underestimate the energy absorption capacity under shear failure. This absence of accurate assessing the relevant issues associated with direct shear failure provides the genesis for development of shear model and evaluation of their shear strength. Thus the second objective of the study attempts to rationally predict the shear stress to slip characteristics of a RC member using mathematical expressions and develops fully nonlinear resistance functions for describing the shear stress to slip behaviour. With this goal, the shear failure is studied using the direct shear push-off test configuration for normal reinforced concrete. A finite element model (FEM) is used to simulate the shear behaviour of push-off specimens under various loading conditions. The FEM is

developed using LS-DYNA program and the FEM is calibrated against the push-off testing data. The failure mode and the stress-slip relationship are analysed. Toughness parameters and equivalent shear strength based on the test results are defined for structural design.

Chapter 3 contains three journal papers, which utilises experimental or simplified finite element method analysis technique for determining response of high strength reinforced concrete (HSRC) and ultra-high performance fibre reinforced concrete (UHPFRC) members subjected to blasts. Various investigations have been carried out using different blast tests to evaluate blast resistant capacity of HSRC and UHPFRC structural members. Some full scale and small blast tests have been carried out in this field and the results have demonstrated that UHPFRC structural members can be very effective for blast resistance than normal reinforced concrete members. However, most of the experiments focused on HSRC and UHPFRC slabs under blast loads. There are very limited studies focused on behaviour of columns under such extreme loads. Considering beams is always subjected to transverse loads while columns need to be exposed to both transverse and axial loads. The axial load may create an additional bending moment, and hence, lateral deflection of a column could be enhanced. In order to prevent partial or complete progressive collapse and enhancing the building's resistant features, it is necessary to investigate use of UHPFRC for construction of new buildings. Two series of blast testings have been conducted for the UHPFRC columns with selecting of two different mixtures of steel fibres, i.e. twisted steel fibre and micro steel fibre. The first journal paper in this chapter is to investigate capabilities of UHPFRC columns adding the twisted steel fibre (1480 MPa tensile strength with diameter of 0.3 mm and length of 30 mm) and high strength reinforced concrete (HSRC) columns against close-in blasts. To achieve this objective, compression and three points bending tests were performed for providing some additional and quantitative information on evaluating the static mechanical characterization of UHPFRC material, afterwards, a total of eight UHPFRC and two HSRC columns were tested under blast loading. Columns were exposed to varying blast loading and axial loading conditions and the results of different failure modes, reflected blast pressure, as well as column deflection profile were compared. The second journal paper is presented for describing the second series of blast tests which were conducted to investigate the behaviour of UHPFRC columns mixed with micro steel fibre (MF) (0.12 mm diameter with 6 mm length). In total four 0.2m×0.2m×2.5m UHPFRC columns were tested under different designed explosion loads at a standoff distance 1.5m. Blast tests were also performed on four high strength reinforced concrete (HSRC)

columns with the same size and reinforcement as UHPFRC columns to evaluate their behaviour under the same blast loading conditions. The data collected from each specimen included reflected overpressures, column deflections at centre and near the supports. Three major damage modes, including flexural, shear and concrete spalling failure modes, were observed.

The final objective of this thesis is to use a simplified 1D FEM to achieve a high accuracy and computational efficiency for predicting the actual behaviour of UHPFRC columns under explosion. Due to the complexity of structural members under close-range blasts SDOF method cannot accurately predict structural response. In order to overcome the limitations of SDOF method, advanced numerical methods, such as simplified finite element analysis can be helpful. A one dimensional (1D) finite element model (FEM) consists of one dimensional element as opposed to use of the three dimensional elements in commercial FEM software. The use of 1D FEM as a numerical model is paramount to SDOF model, as it doesn't suffer from the limitations of SDOF method while still being numerically efficient, as opposed to the use of three-dimensional finite elements in commercial FEM software. The 1D FEM with incorporation of a new segmental analysis technique can be used for a dynamic analysis so as to accurately, but efficiently, determine the response of UHPFRC and HSRC columns against blasts.

Chapter 2
Numerical Analysis of Reinforced Concrete Structural Members Subjected to blast loading

Introduction

In this chapter, direct shear response of reinforced concrete (RC) structural members subjected to blasts is studied. Two papers were adopted in this chapter, and the first paper is focusing on developing a SDOF model to analyse the flexural and direct shear responses of RC structural members against blasts. The second paper is to develop an accurate physics-based direct shear resistance function for describing the direct shear transfer of RC members by using finite element modelling for more accurate analysis of direct shear responses of RC members in the future.

Within the first paper entitled "Analysis of direct shear failure mode for RC slabs under external explosive loading", three different shear resistance-slip models – elastic, plastic and elastic-plastic – are considered for shear response analysis. Analytical solutions for the shear response equations are derived from SDOF approaches. There are two loosely coupled SDOF systems that consider both flexural failure mode and direct shear failure mode to predict the structural response under external blast loading. For each time step, the motions of the flexural response at the centre are computed, from which it is possible to derive a distribution of inertia force and then combine such force with the applied load for obtaining a shear force at the support. That shear force is used to derive the second SDOF system which provides the shearing motions at the supports. In addition, although a great deal of progress has been made on the development of P-I diagrams for different structures under blast loads, the shortcoming of the existing works on P-I diagrams is mainly regarding the flexural response, P-I diagrams for direct shear response haven't been derived before. Since many experiments prove that some structures can fail in a combined shear and flexural response under explosions, both the flexural and direct shear failure modes need to be considered. To achieve this purpose, pressure-impulse diagrams for both flexural and shear failure modes are developed based on the solutions which generated by using SDOF system, and the effects of various flexural and direct shear resistance-deflection/slip models on the P-I curves are investigated. Afterwards, empirical formulae are derived to predict pressure-impulse curves in a simplified way. In order to examine the accuracy of the empirical formulae, various P-I curves generated by the SDOF systems are

compared with those generated by the derived empirical formulae. The final stage of this research is to confirm the efficacy of the empirical formulae by evaluating the formulae of the pressure asymptote and impulsive asymptote.

Considering the previous developed simplified shear resistance function may not be accurate enough for modelling the shear transfer of RC structures, substantial improvements can be made to improve the simplified shear resistance model into a physical based non-linear model. Thus the second paper titled "Numerical Analysis of Shear Transfer across an Initially Uncrack Reinforced Concrete Member" developed a model for prediction of shear behaviour by using the direct shear push-off test configuration for normal reinforced concrete with various concrete strength and reinforcement.

The shear failure of e reinforced concrete members under static and impact loads has been one of the major safety concerns of designers in recent years. Some experimental studies have been performed to evaluate the shear strength between two concrete layers, and it is widely accepted that the following parameters contribute to shear strength: the roughness of the substrate surface known as chemical connection between concrete, dowel action and friction which appears when relative slippage between concrete layers takes place in the presence of normal stresses to the interface. However, as experimental investigations result in extensive costs; up to now, no generally admitted conclusions or predictions of shear stress to slip relationships can be derived merely based on the existing experimental results. As a consequence, physics-based numerical analyses have become important resources for both academics and structural engineers to reliably predict structural damage in a cost effective way. In addition, the available finite element investigation in the literature, on the scope of shear transfer of reinforced concrete member is very limited, and most of the existing literatures are to validate the capabilities of numerical modelling of various types of push-off specimens or discuss the effect of vary parameters on shear strength, but the expressions of shear-slip behaviour haven't been further discussed. Therefore, in the current study, authors are first looking for verified and validated numerical models with experimental results, so that consistent sets of simulated response data can be generated confidently for studying shear behaviour in design and assessments shear failure. LS-DYNA program is used as a numerical tool to investigate individual parameters affecting the concrete to concrete interface of push-off test specimens

and capture the effect of important issues. After the validation, the ultimate shear stress and slip are derived based on the shear theory. Finally, the shear stress to slip relationship is derived.

This chapter adopts the following journal publications:

- Xu J., Wu C., and Li Z.X. (2014). "Analysis of Direct Shear Failure Mode for RC Slabs under External Explosive Loading". International Journal of Impact Engineering, 69:136-148.
- Xu J., Wu C., Li Z.X. and Ng C.T. (2015). "Numerical Analysis of Shear Transfer across an Initially Uncrack Reinforced Concrete Member". Engineering Structures, 102:296-309.

Journal Article 1:
Analysis of direction shear failure mode for RC slabs under external explosive loading

[THIS PAGE IS INTENTIONALLY LEFT BLANK]

Statement of Authorship

Title of Paper	Analysis of direct shear failure mode for RC slabs under external explosive loading
Publication Status	☑ Published ☐ Accepted for publication ☐ Submitted for Publication ☐ Unpublished and Unsubmitted w ork w ritten in manuscript style
Publication Details	International Journal of Impact Enigneering, 69, pp.136-148

Principal Author

Name of Principal Author (Candidate)	Juechun Xu		
Contribution to the Paper	Carry out numerical simulations, data analysis and preparation of manuscript.		
Overall percentage (%)	85%		
Certification:	This paper reports on original research I conducted during the period of my Higher Degree by Research candidature and is not subject to any obligations or contractual agreements with a third party that would constrain its inclusion in this thesis. I am the primary author of this paper.		
Signature		Date	21 October 2015

Co-Author Contributions

By signing the Statement of Authorship, each author certifies that:

i. the candidate's stated contribution to the publication is accurate (as detailed above);

ii. permission is granted for the candidate in include the publication in the thesis; and

iii. the sum of all co-author contributions is equal to 100% less the candidate's stated contribution.

Name of Co-Author	Chengqing Wu		
Contribution to the Paper	Guidance of numerical simualtions and review of manuscript.		
Signature		Date	19 October 2015

Name of Co-Author	Zhong-Xian Li		
Contribution to the Paper	Review of manuscript		
Signature		Date	25 October 2015

Please cut and paste additional co-author panels here as required.

[THIS PAGE IS INTENTIONALLY LEFT BLANK]

International Journal of Impact Engineering 69 (2014) 136–148

Contents lists available at ScienceDirect

International Journal of Impact Engineering

journal homepage: www.elsevier.com/locate/ijimpeng

Analysis of direct shear failure mode for RC slabs under external explosive loading

Juechun Xu [a], Chengqing Wu [a,b,*], Zhong-Xian Li [b]

[a] School of Civil, Environmental and Mining Engineering, The University of Adelaide, Australia
[b] TCU-UA Joint Research Centre on Disaster Prevention and Mitigation, Tianjin Chengjian University, China

ARTICLE INFO

Article history:
Received 11 July 2013
Received in revised form
20 February 2014
Accepted 25 February 2014
Available online 5 March 2014

Keywords:
Elasto-plastic model
Direct shear
P-I diagram
Blast loading
SDOF

ABSTRACT

The single degree of freedom system (SDOF) is used to predict the shear responses of RC (reinforced concrete) members under external blast loading in the present study. An RC member suffering a blast may experience both flexural and shear failure modes. Under very high amplitude short duration shock, structural failure is usually governed by direct shear loading, whereas under low amplitude long duration shock, the structural failure is most likely governed by flexural damage. However, most previous studies are based on the assumption that flexural response dominates the failure mode without taking shear failure into consideration. In the present study, dynamic response equations of a structural member experiencing direct shear failure are derived for elastic, plastic and elasto-plastic shear resistance–slip models. With these equations the P–I curves of both flexural and direct shear failure modes are generated for an RC slab. Furthermore, a parametric study is conducted to investigate the effect of different parameters of RC slabs on the pressure–impulse (P–I) diagrams based on the elasto-plastic model. Finally, based on the results from the parametric studies, curve fitting technique is used to generate the P–I curves for RC slabs in a simplified way.

1. Introduction

Due to an increase in terrorist attacks and various accidental explosions in recent years, structural responses to blast loading have become increasingly important issues for governments and engineers who seek to minimize harm to both public and private structures. More and more investigation, therefore, has been conducted on the response of structures subjected to blasts.

It is known that when an RC member is subjected to high amplitude blast loads, its failure is dominated by the crushing and spalling of concrete and by direct shear damage; whereas under low amplitude overpressure, its failure is most likely governed by flexural damage. Flexural responses have, in fact, been the subject of considerable research, while direct shear failure is seldom taken into account during blast response analysis [1], as it is very difficult to analyze RC members under high amplitude shock loading of an extremely short duration.

Experimentally, however, it has been observed that when an RC member is subjected to a distributed load of extremely short duration, some of the structural members may fail at the positions near the support instead of the flexural failure occurring at mid-span [2], it is because the maximum shear force may cause a failure plane parallel to the loading direction [3]. As noted by Ma et al. [4], compared with bending failure, shear failure is sometimes a kind of brittle failure that may cause the collapse of structural members. Therefore, direct shear failure may dominate the damage caused by an explosion, especially when the detonation is very close to the structural member [5].

As it is not straightforward to derive the closed form solutions for the responses of an RC member subjected to blast loading, approximation techniques such as single-degree-of-freedom (SDOF) models provide quick evaluation for assessment of structural members and offer relatively good results [6]. The SDOF system is therefore used to model direct shear failure of a support under external blast loading.

Pressure–Impulse (P–I) diagrams are commonly used to assess the structural damage of a member subjected to a blast load. Based on the assumption that a structure is often damaged owing to the flexure response; several momentous developments on using different methods for generated the P–I curved can be summarized as following: The earliest works on P–I diagrams are included in the work of Abrahamson and Lindberg [7] for concerning the linear elastic to rigid–plastic beams and plates against blasts. Afterwards,

* Corresponding author. School of Civil, Environmental and Mining Engineering, The University of Adelaide, Australia. Tel.: +61 8 83034834.
E-mail address: cwu@civeng.adelaide.edu.au (C. Wu).

http://dx.doi.org/10.1016/j.ijimpeng.2014.02.018
0734-743X/

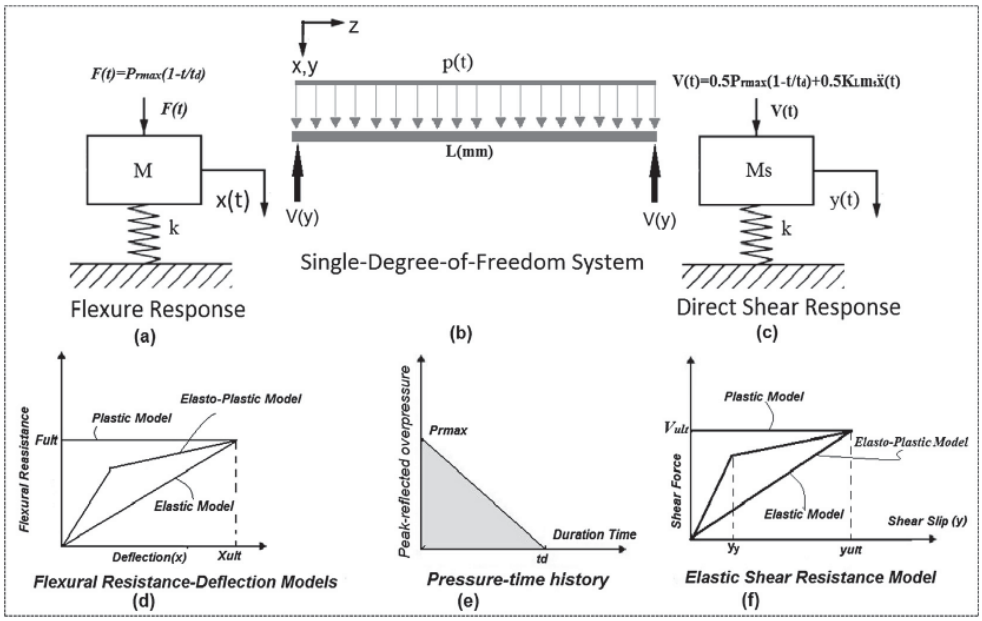

Fig. 1. SDOF systems of flexure and direct shear response.

many researchers have worked extensively on the subject of pressure–impulse diagrams, for example, Fallah and Louca [8], the flexural response resistance functions in their research have been categorized into elastic, elastic–plastic hardening, elastic–plastic–softening, rigid–plastic–hardening and rigid–plastic–softening. Furthermore, both bilinear and nonlinear flexural resistance functions have been considered to obtain the P–I diagrams of concrete structures [9]. After comparing the suitability, applicability and reliability of various methods in constructing P–I diagrams for structural components, Shi et al. [10,11] have used numerical method and analytical formulae for predicting the P–I curves of RC column. Recently, a great deal of progress has been made on the development of P–I diagrams for different structures under blast loads such as RC and FRC (fiber reinforced concrete) circular plates [12], continuous beams [13] and simply supported ultra high performance reinforced concrete (UHPRC) slabs [14]. However, the shortcoming of the discussed existing works on P–I diagrams is mainly regarding to the flexural response, the need for considering the different failure modes such as direct shear response hasn't been conducted. Beside failure in flexural mode, many experiments prove that some structures can be failed in a combined shear and flexural response under explosion [15,16]. In addition, a unique form of shear failure at the supports of RC beams and slabs is also observed in some experiments [17]. In order to determine the overall survivability of an RC member, both the flexural and direct shear failure modes need to be considered. Thus a P–I interaction diagram exhibiting two curves is required to indicate the combination of load and impulse.

Normally, the current dynamic systems for modeling the P–I diagrams of the shear and flexural response for structural members against blasts consist of two major approaches. The first approach is based on an approximate yield curve relating limiting values of shear force and bending moment and various deformations are found to occur with combination of bending and shear sliding depending upon the velocity profile [18]. By taken the transverse shear effects, boundary conditions, pulse shape effects into considerations, considerable research has been conducted for using theoretical analysis to evaluate the dynamic plastic responses of various metallic structural members, such as, beams, plates, and shells [18–28]. Although Jones and Li have shown in numerous studies moving plastic hinges of purely flexural nature where a plastic hinge is formed near the support and moves inward as a consequence of the minimum upper bound theorem of plasticity, the closed form solutions can only be derived for beams with a rigid–plastic shear–slip and moment rotation relationship which

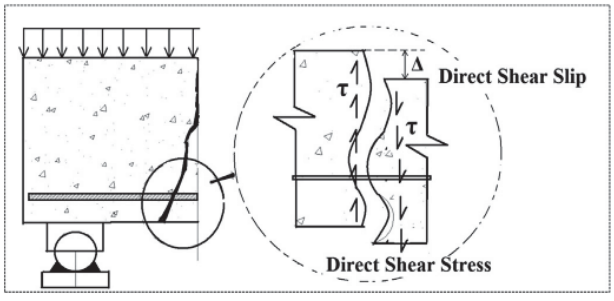

Fig. 2. Direct shear resistance–slip models.

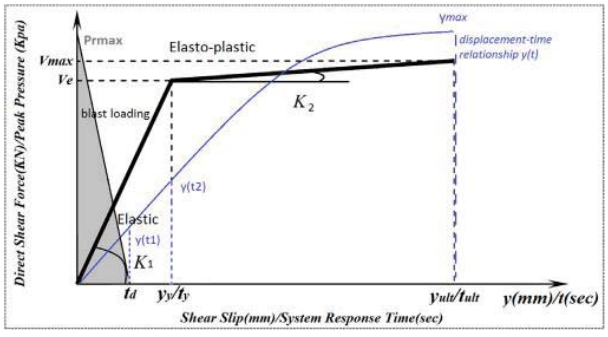

Fig. 3. Response in elastic phase of the elasto-plastic model of direct shear mode.

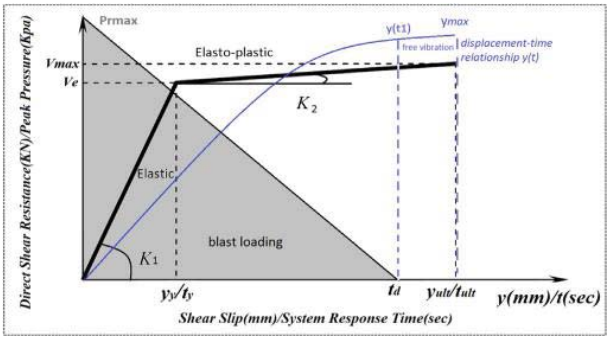

Fig. 4. Response in plastic phase of elasto-plastic model of direct shear mode.

obviously cannot be applied to our case in which simply supported RC slabs with bi-linear or non-linear behavior are being analyzed. Therefore, for the bi-linear or non-linear behavior, the development of the closed form solutions will be very difficult and complex and so far none of the published papers have been successful in using this approach to determine RC member response under blast loading in this research field.

In order to get a valid P–I relationship for a broad spectrum of structural resistance behavior, the second approach proposed by Krauthammer [29–31], Low and Hao [1,32] has widely been used to model the interaction of the direct shear and flexural response of RC slabs under blast loads by applying the bi/tri-linear structural resistant functions. Some efforts have been carried out to estimate the failure probabilities and P–I diagram for a flexural failure of RC slabs subjected to blast loading [1,17,32]. However, P–I diagrams for direct shear failure are usually less taken into consideration and the sensitivity of the P–I curves to various structural responses and member properties are not mentioned in those studies [29–31]. In the present study, by extending the results derived by Krauthammer [29–31], and Low and Hao [1,32], the P–I curves based on elastic, plastic and elastic–plastic resistance model considering both direct shear and flexural effects are developed.

Therefore, in order to develop a simple mathematical way to analyze the flexure and direct shear responses of an RC slab, instead of considering the form and moving plastic hinges, the SDOF approximation was adopted in the present study as it can be calculated for an RC slab with bi-linear or non-linear behavior. The works in this area include the references [29,30,33–35] and the behavior prediction of more advanced Timoshenko beam theory proposed by Krauthammer et al. [36], which have shown to provide exactly the same results as those determined using the SDOF system. In addition, Krauthammer et al. [30] concluded that the flexural failure modes and direct shear failure modes are always independent to each other. It is always acceptable because of the two failure modes do not occur simultaneously; the structure always enter the flexural failure mode when it can sustain the direct

Table 1
RC slab variables adopted in the analysis.

Structural variables		Slab parameters	
f_{cu}	32 MPa	L	2000 mm
Ec	25680.8 MPa	B	400 mm
f_y	500 MPa	h	100 mm
Es	200 GPa	D	85 mm
ρ	1.4%	Mass	1.92 kN
ε_{cu}	0.0054	No. Bars in compression area	5
Steel diameter	12 mm	No. Bars in tension area	5

shear failure [1]. In all these studies, the two failure modes, direct shear and flexure, are modeled independently and none of the above studies considers the interaction diagram between the two failure modes. In the present studies, there are two loosely coupled SDOF systems that consider both flexural failure mode and the direct shear failure mode to predict the structural response under external blast loading. For each time step, the motions of the flexural response located at the center are computed, from which it is possible to derive a distribution of inertia force and then combine such forces with the applied load for obtaining a shear force at the support [29]. That shear force is used to derive the second SDOF equation which provides the shearing motions at the supports. This loosely coupled SDOF system has been described by Krauthammer [29] and analysis by using this approach has also been carried out to estimate the failure probabilities of RC slab under blast loading by Low and Hao [1]. In addition, although the traveling shear hinges is a possible form in the hardening case, with separated calculation process of flexural and shear response, the traveling shear hinges cannot be considered in the SDOF study and this is acceptable by many researchers [1,30]. Also, a comparison between the P–I curves derived by using the SDOF elastic, perfectly plastic model and rigid–plastic model has been made by Ma et al. [4]and it shows that although the rigid–plastic beam model has advantages in characterizing the combined beam failure modes, results generated by these two different methods still have general good agreement. The discrepancy between whether or not taking the transverse shear effect into account is acceptable in practical engineering, especially when the peak pressure and impulse of pulse load is large [4]. To retain the consistency of the elastic cases in the SDOF system and provide quick evaluation for assessment, the traveling shear hinges have not been considered in the present study.

In the present paper, three different shear resistance–slip models – elastic, plastic and elastic–plastic – are considered for shear response analysis. Analytical solutions for the shear response equations are derived from the SDOF models. Based on the solutions, pressure–impulse diagrams for both flexural and shear failure modes are generated, and the effects of various flexural and direct shear resistance-deflection/slip models on the P–I curves are investigated. Afterwards, empirical formulae are derived to predict pressure–impulse curves in a simplified way. In order to examine the accuracy of the empirical formulae, various P–I curves

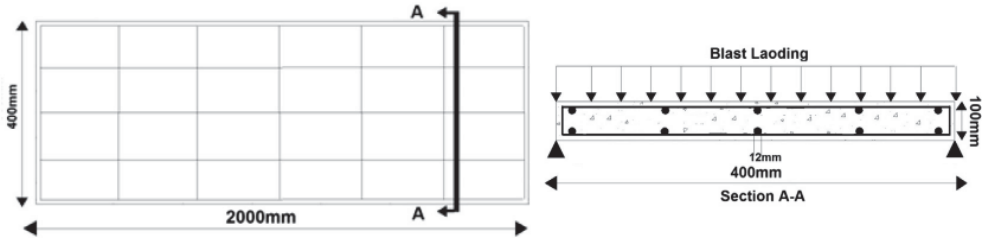

Fig. 5. Geometry details of the reinforced concrete slab.

Table 2
Charge information.

Predicted blast information	
Charge distance	1.5 m
Charge weight (TNT)	8.3 kg
Scaled displace	0.74 m/kg$^{1/3}$
Predicted impulse	1.72 KPa s
Predicted peak reflected over pressure	12420 KPa
Duration time	0.000276 s

Table 3
Flexural and direct shear response value adopted in analysis.

Slab strength (flexure)				Slab strength (direct shear)			
K_{f1}	41454.5 kN/m	F_y	182.4 kN	K_{s1}	4.22×10^6 kN/m	V_y	422.3 kN
K_{f2}	186.1 kN/m	F_{ult}	190.7 kN	K_{s2}	4642.9 kN/m	V_{ult}	598.7 kN
x_y	0.0044 m			y_y	0.1 mm		
x_{ult}	0.049 m			y_{ult}	0.6 mm		

generated by the SDOF system are compared with those generated by the derived empirical formulae. The final stage of this research is to confirm the efficacy of the empirical formulae by evaluating the formulae of the pressure asymptote and impulsive asymptote.

2. Single-degree-of-freedom systems (SDOF)

The SDOF system has been widely used for predicting the dynamic response of RC members subjected to blast loading [27]. As indicated by Krauthammer et al. [37], the direct shear failure and flexural failure mode of an RC member under blasts usually do not occur simultaneously. Therefore, the direct shear and flexural responses of a structural member as shown in Fig. 1(b) are modeled using separate SDOF systems [Fig. 1(a) and (c)] based on their resistance to slip or deflection respectively.

Without considering the damping, the direct shear response of the member in Fig. 1(c) can be described by the following equation of motion

$$m_s\ddot{y} + V(y) = V(t) \tag{1}$$

where y is the direct shear slip response; $V(y)$ is the shear resistance function; $V(t)$ is the equivalent direct shear force on the RC members over the duration; and m_s is the equivalent mass of the member. As shown in Fig. 1(c), the direct shear force $V(t)$ applied on the support includes two parts: the first part is contributed by half of the blast force; the other part is the inertia force of the structure due to the acceleration of the flexural response. Thus direct shear force can be described by

$$V(t) = 0.5P(t) + 0.5K_L m_S\ddot{x}(t) \tag{2}$$

where $P(t)$ is the total blast force acting on the member; $\ddot{x}(t)$ is acceleration of the flexural response of the member; and K_L is the load factor.

The direct shear failure mode tends to occur in members under close range blast loading. This kind of failure usually appears near the supports or the joints of the elements as shown in Fig. 2, the shear force may cause a sliding type failure along the plane while the direct shear slip appears parallel to the axis of the member [5]. In the current study, three different direct shear failure responses which are Elastic, Plastic and Elasto-Plastic models [Fig. 1(f)] have been used for describing the direct shear stress and direct shear slip relationship as shown in Fig. 2. The arbitrarily selected direct shear resistance functions used in this research adds value by highlighting the evaluation of the shear response of different types of structural members against external blast loading. For instances, elastic direct shear models are often used when considering the failure of plain concrete or concrete members, such as corbels and ledger beams, in which shear failure can be sudden. Plastic models are of assistance when assessing the structural response to explosions in terms of the shear behavior of rigid–plastic beams made from isotropic materials, such as steel and aluminum-alloy cantilever slabs. Furthermore, the elasto-plastic model mentioned in section 5 assists in evaluating the direct shear failure mode of conventional reinforced concrete slabs having well-anchored main reinforcements.

According to the research by Krauthammer et al. [37], the direct shear failure won't cause tremendous deformation of the structure due to the very short duration after the initial blast loading, and the fact that the failure plane is so close to the support. The result is much like a sudden collapse. Therefore when considering the equivalent direct shear force function, the structural shape function can be taken as unity without taking deflection into account. The shear mass transformation factor can be taken as unity as well [32].

When developing the SDOF model for direct shear failure mode, three different shear resistance–slip models can be considered – elastic, plastic and elastic–plastic [Fig. 1(f)]. For the elastic model, the shear–slip relationship is treated as linear and the plastic resistance–slip model as a constant line. The elasto-plastic model has a bi-linear shear stress–slip relationship.

Because the acceleration of the flexural response is treated as the inertia force that appears in the direct shear equation, the SDOF system of flexural response which is incorporated into the direct shear response is also included in this analysis. The SDOF system for

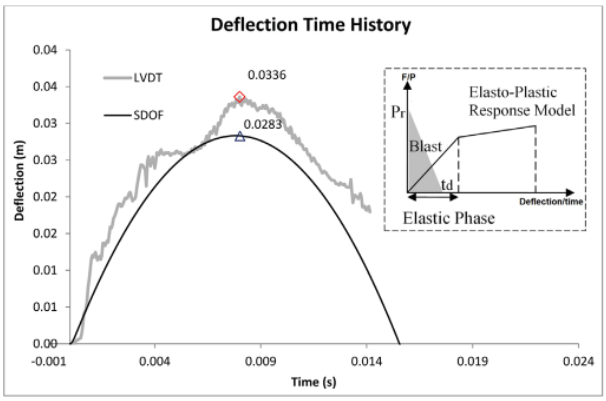

Fig. 6. Comparison of SDOF deflection-time history and measured testing data (LVDT).

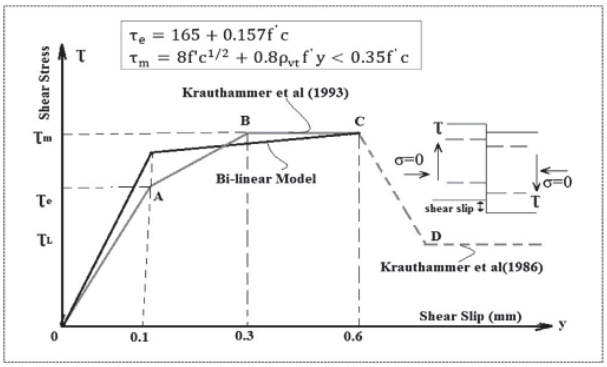

Fig. 7. Shear stress–slip relationships of the direct shear failure mode (Krauthammer et al. 1986).

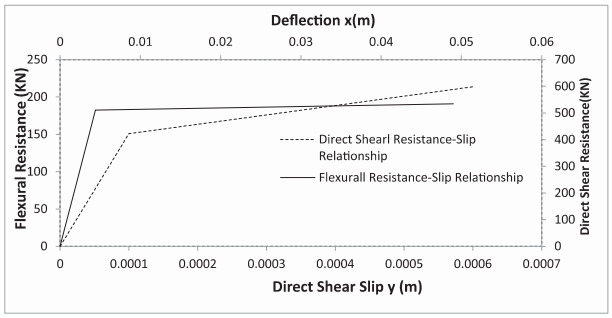

Fig. 8. Resistance functions of flexural and direct shear failure modes.

modeling the flexural response is based on Low and Hao [32] where the structural deflected shape is considered to be the same as that resulting from the static application of a dynamic load. The triangular blast load as shown in Fig. 1(e) is used in this study. The deflection of flexural response [Fig. 1(a)] can be represented as the following equation

$$m\ddot{x}(t) + R(x) = F(t) \tag{3}$$

where x is the displacement response of the member; $R(x)$ is the flexural resistance-deflection function; $F(t)$ is the equivalent force function on the member over the duration; and m is the equivalent mass of the member. The damping is neglected in the present study. Using the support conditions associated with the required plastic hinge, the flexural resistance-deflection curve can be derived in terms of the calculated ultimate moment using the method proposed by Low and Hao [1].

In order to compare the direct shear failure modes with flexural ones, three different resistance-deflection curves [shown in Fig. 1(d)] are also included in the present study. The details of the method by which a flexural response can be generated using the SDOF system can be referred to the theoretical derivation proposed by Vugts et al. [38]. It should be noted that the two SDOF equations (Equation (1) and Equation (3)) are loosely coupled through the acceleration of the flexural response and they will be used model the interaction of the direct shear and flexural response of RC slabs under blast loads.

3. Shear response analysis

A simplified triangular shape representing a blast load, as shown in Fig. 1(e), was used in the dynamic analysis of the shear response.

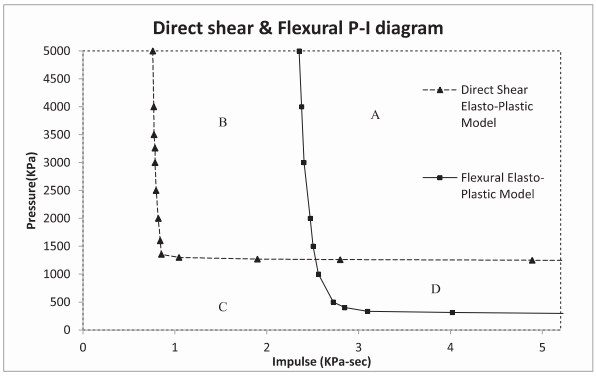

Fig. 9. Pressure–impulse relationships of flexural and direct shear failure modes.

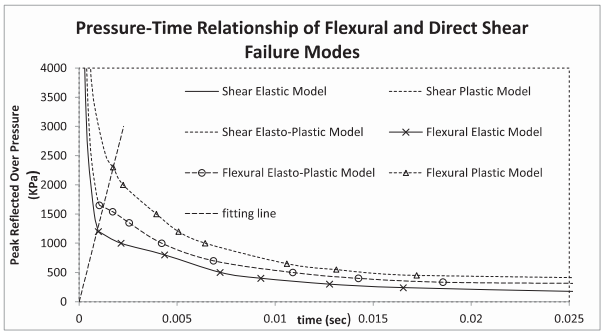

Fig. 10. Peak reflected overpressure–time relationships of flexural and direct shear failure modes with different structural resistances.

Conservation of force (energy) in the SDOF system means that the inertia force and shear resistance force on the left hand side of the equation must equal the direct shear force applied on the member support. The equations of motion related to various structural response modes can be derived as explained in the following sections.

3.1. Development of shear response for an elastic model

Based on the research of Low and Hao [1], shear force is composed of the pressure loading and inertia force of a structure, where the acceleration of flexural responses is represented as the inertia force in the direct shear equation because the two SDOF systems are loosely coupled through it. By transforming the member into the equivalent direct shear SDOF system, the elastic shear response of the system subjected to the triangular blast loading can be described by

$$m\ddot{y} + k_1 y = 0.5P_{r\max}\left(1 - \frac{t}{t_d}\right) + 0.5K_L m_S \ddot{x}(t) \tag{4}$$

where y is the shear slip at its support; k_1 is the pre-yielding direct shear stiffness; $P_{r\max}$ is the applied blast force resulting from peak reflected overpressure. When analyzing for the RC slabs or beams, the applied blast force can be calculated as $p_{r\max}bL$, where b and L

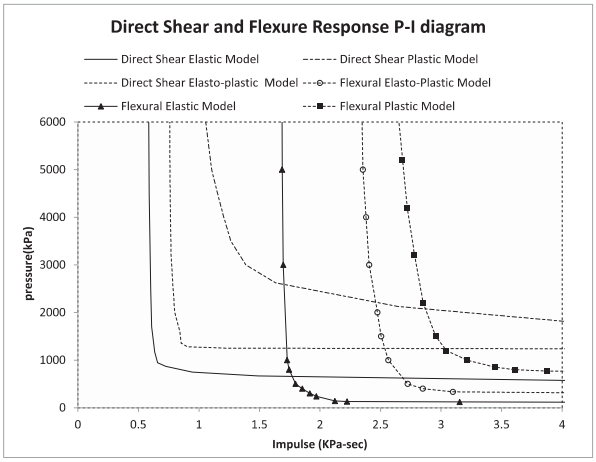

Fig. 11. Pressure–impulse relationships of direct shear and flexure failure modes with different structural resistances.

Table 4
Parameters of Equation (43).

Model type	P_0 (KPa)	I_0 (KPa s)	n_1	n_2
Elastic	669	0.58	0.00074	1.5
Plastic	1800	0.94	0.00065	2
Elasto-Plastic	1230	0.75	0.0006	1.6

are the length and width of the member, respectively; t_d is the duration of the blast loading. It should be noted that $\ddot{x}(t)$ as the acceleration of the flexural response is obtained from the flexural response equations and that the flexural elastic–plastic model has been selected as the structural resistance deflection curve in the flexure response analysis.

The corresponding shear slip y at the support of the member, subjected to triangular peak reflected overpressure–time history can be solved as

$$y(t) = A\sin\omega_1 t + B\cos\omega_1 t - \frac{P_{r\max}}{2t_d\omega_1^2 m_s}t + \frac{P_{r\max} + K_L m_s \ddot{x}(t)}{2\omega_1^2 m_s} \tag{5}$$

$$y(t)' = A\omega_1\cos\omega_1 t - B\omega_1\sin\omega_1 t - \frac{P_{r\max}}{2t_d\omega_1^2 m_s} \tag{6}$$

For the response before time t_d $(0 < t < t_d)$, taking the initial condition as $y(0) = 0, y'(0) = 0$, the constants A and B in Equations (5) and (6) can be solved

$$A = \frac{P_{r\max}}{2t_d\omega_1^3 m_s} \tag{7}$$

$$B = -\frac{P_{r\max} + K_L m_s \ddot{x}(t)}{2\omega_1^2 m_s} \tag{8}$$

When no forcing function is applied after the time t_d, the free vibrations response of the elastic model can be derived by rewriting Equation (4) as

$$m\ddot{y} + k_1 y = 0.5K_L m_S \ddot{x}(t) \tag{9}$$

The solution of this equation is

$$y(t) = A\sin\omega_1(t - t_1) + B\cos\omega_1(t - t_1) + C \tag{10}$$

$$y'(t) = A\omega_1\cos\omega_1(t - t_1) - B\omega_1\sin\omega_1(t - t_1) \tag{11}$$

Taking the initial condition as $y(0) = y(t_d), y'(0) = y(t_d)'$; $y(t_d)$ represents the shear slip that the elastic model can achieve whenever the system response time reaches the maximum loading

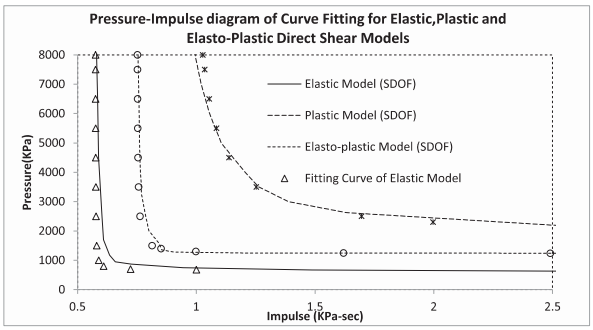

Fig. 12. Curves fitting for elastic, plastic and elasto-plastic direct shear models.

Table 5
Benchmark model in parametric studies.

Structural variables		Slab parameters	
f_{cu}	46.9 MPa	L	3000 mm
Ec	38500 MPa	B	1000 mm
f_y	594 MPa	h	170 mm
Es	200 GPa	D	145 mm
ρ	2.8%	Mass	1240 kg

duration t_d. The constants A and B in Equations (10) and (11) can be solved as

$$A = y'_{td}/\omega_1 \tag{12}$$

$$B = y_{td} - C \tag{13}$$

$$C = \frac{0.5K_L m_S \ddot{x}(t)}{\omega_1^2 m_s} \tag{14}$$

3.2. Development of shear response for a plastic model

The derivation of shear response for a plastic model is very similar to that for the elastic model; however, the shear resistance–slip function for a plastic model becomes a constant. The differential equation that governs the shear response of the member is

$$m\ddot{y} + V_{ult} = 0.5P_{r\max}\left(1 - \frac{t}{t_d}\right) + 0.5K_L m_S \ddot{x}(t) \tag{15}$$

where V_{ult} is the ultimate shear resistance force that the member can experience before the shear failure occurs. It should be noted that $\ddot{x}(t)$ as the acceleration of the flexural response can be obtained from the flexural elastic–plastic model using the process obtained by Vugts et al. [1]. Solving Equation (15), the corresponding shear slip at the support of the member subjected to peak reflected overpressure–time history can be found. For the shear response before time t_d $(0 < t < t_d)$, the solution of Equation (15) with the initial conditions $y(0) = 0, y'(0) = 0$ is

$$y(t) = \frac{1}{m_s}\left(\frac{P_{r\max}}{4}t^2 - \frac{P_{r\max}}{12t_d}t^3 + \frac{K_L m_s \ddot{x}(t)}{4}t^2 - \frac{V_{ult}}{2}t^2\right) \tag{16}$$

$$y(t)' = \frac{1}{m_s}\left(\frac{P_{r\max}}{2}t - \frac{P_{r\max}}{4t_d}t^2 + \frac{K_L m_s \ddot{x}(t)}{2}t - V_{ult}t\right) \tag{17}$$

When no forcing is applied after the time t_d, the free vibrations response for the plastic model can be derived by rewriting Equation (15) as

$$m\ddot{y} + R_{ult} = 0.5K_L m_S \ddot{x}(t) \tag{18}$$

Solving the above equation, the corresponding shear slip at the support of the member subjected to different blast loads can be obtained. For the shear response before time t_d $(0 < t < t_d)$, the

Table 6
Parametric studies of $f'c$, f_y and reinforcement ratio.

Concrete strength			Steel strength			Reinforcement ratio		
$f'c$ (MPa)	P_0 (KPa)	I_0 (KPa s)	f_y (MPa)	P_0 (KPa)	I_0 (KPa s)	ρ%	P_0 (KPa)	I_0 (KPa s)
30	1680	1.22	294	1242	1.09	1.15%	1259	1.11
46.9	1851	1.27	394	1367	1.15	1.50%	1421	1.16
60	2006	1.38	594	1851	1.27	1.92%	1617	1.2
70	2107	1.43	694	2096	1.35	2.80%	1851	1.27

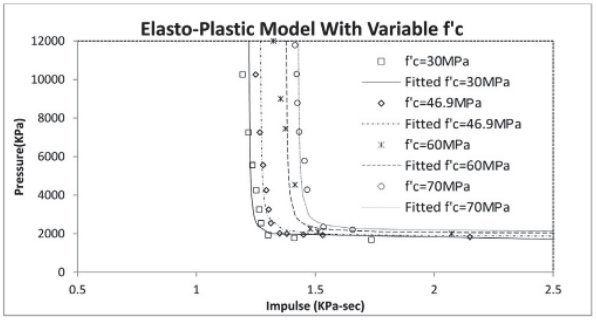

Fig. 13. Pressure–impulse relationships of direct shear failure modes with different $f'c$.

solution of Equation (18) with the initial conditions $y(0) = y(t_d)$, $y'(0) = y(td')$ is

$$y(t) = \frac{1}{m_s}\left(\frac{K_L m_s \ddot{x}(t)}{4}t^2 - \frac{V_{ult}}{2}t^2\right) + y'_{td}t + y_{td} \tag{19}$$

$$y(t)' = \frac{1}{m_s}\left(\frac{K_L m_s \ddot{x}(t)}{2}t - V_{ult}t\right) + y'_{td} \tag{20}$$

where $y(t_d)$ describes the shear slip which in the system deformation response corresponds to time t_d

3.3. Development of shear response for an elastic–plastic model

3.3.1. Elastic phase of elastic–plastic model

For an elastic–plastic model under an external blast, the shear resistance–slip function is bi-linear as shown in Fig. 3.

In order to develop the slip-time relationship based on this bi-linear shear–slip relationship, there are three conditions which form the basis of three different analyses:

1. When the system shear response time is less than or equal to the time t_d, the shear slip is limited to the elastic phase of the structural behavior. In stage one, as illustrated in the Fig. 3, when the blast loading is applied to the member until t_d the shear resistance slip function is still in the elastic phase. The procedure is exactly the same as in the elastic model, and the derivations can be referred to the solutions in the elastic model [Equations (4)–(8)].
2. When the system shear response time is more than the time t_d but less than t_y (i.e., the time when the member reaches the maximum elastic slip y_y), the free vibrations response occurs in the elastic phase of the structural behavior. In stage two, as illustrated in Fig. 3, when no shear forcing function is applied after the time t_d, the free vibrations response at the elastic phase can be derived. The scenario is the same as those for the elastic model, and the solutions can also be referred to the elastic model [free vibration phase Equations (9)–(14)].

Table 7
Parametric studies of slab span, width and depth.

Slab span			Slab width			Slab depth		
L (mm)	P_0 (KPa)	I_0 (KPa s)	B (mm)	P_0 (KPa)	I_0 (KPa s)	H (mm)	P_0 (KPa)	I_0 (KPa s)
2000	2777.9	1.615	1000	1816.157	1.267	85	953.171	0.635
3000	1850.5	1.267	1200	1816.157	1.159	170	1850.5	1.267
4000	1338.5	1.155	1400	1826.057	0.981	225	3621.38	1.975
5000	1014.9	0.979	1500	1829.5	0.981	306	4850.662	2.415

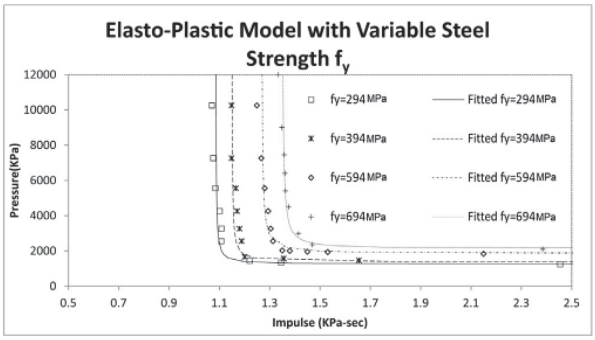

Fig. 14. Pressure–impulse relationships of direct shear failure modes with different f_y.

3. When the system shear response time is more than the time t_y (i.e., the time is less than or equal to the time t_{ult} when member reaches the maximum shear slip y_{ult}), the free vibrations response occurs in the plastic phase of the structural behavior. In stage three, the free vibrations response at the plastic phase can be derived as

$$m\ddot{y} + k_2 y + y_y(k_1 - k_2) = 0.5K_L m_S \ddot{x}(t) \tag{21}$$

The solution of this equation is

$$y(t) = A\sin\omega_2 t + B\cos\omega_2 t + C \tag{22}$$

$$y'(t) = A\omega_2\cos\omega_2 t - B\omega_2\sin\omega_2 t \tag{23}$$

Taking the initial condition as $y(0) = y(t_2)$, $y'(0) = y(t_2)'$, the constants A, B and C in Equations (22) and (23) can be solved as

$$A = \frac{y'_{t_2}}{\omega_2} \tag{24}$$

$$B = y_{t_2} - C \tag{25}$$

$$C = \frac{0.5K_L m_S \ddot{x}(t) + y_y(k_2 - k_1)}{\omega_2^2 m} \tag{26}$$

3.3.2. Plastic phase of elasto-plastic model

Fig. 4 shows the plastic phase of the elasto-plastic model. As can be seen from the figure, the three conditions include: firstly, when the system response time t_y at y_y is less than t_d; secondly, when the system response time is less than or equal to t_d, shear response

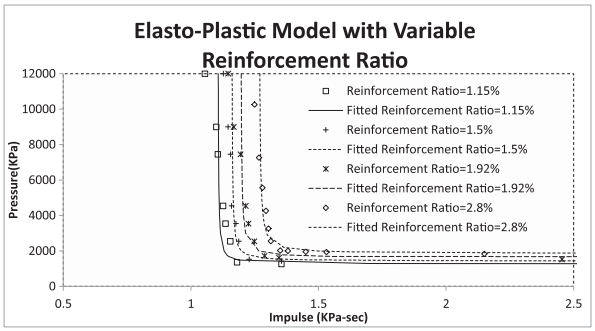

Fig. 15. Pressure–impulse relationships of direct shear failure modes with different ρ.

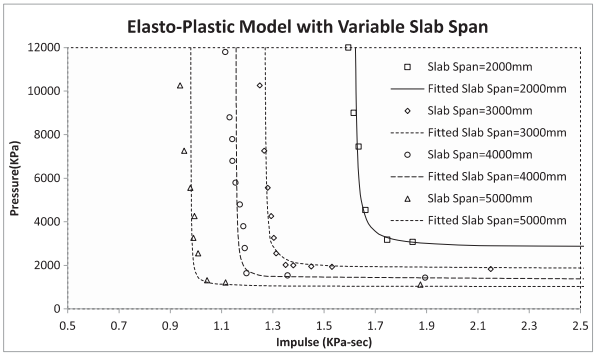

Fig. 16. Pressure–impulse relationships of direct shear failure modes with different *L*.

exceeds y_y, but less than y_{ult}; and, thirdly, when no shear force is applied to the system, the free vibration occurs until the maximum shear slip equals y_{ult}.

During the analysis, the response to the first condition can be the same as the response to the first condition of the elastic–plastic model [Equations (4)–(8)]. For the second condition, however, the motion equations need to be solved with the initial conditions $y\ (0) = y_y$, $y'(0) = y_y'$, as in the following equations

$$m\ddot{y} + k_2 y + y_y(k_1 - k_2) = 0.5P_{r\max}\left(1 - \frac{t}{t_d}\right) + 0.5K_L m_S \ddot{x}(t) \tag{27}$$

The solutions of the above equation with the initial conditions are

$$y(t) = A\sin\omega_2 t + B\cos\omega_2 t + Ct + D \tag{28}$$

$$y(t)' = A\omega_2\cos\omega_2 t + B\omega_2\sin\omega_2 t + C \tag{29}$$

where

$$A = \left(y_y' - C\right)\Big/\omega_2 \tag{30}$$

$$B = y_y - D \tag{31}$$

$$C = -\frac{P_{r\max}}{2t_d\omega_2^2 m_s} \tag{32}$$

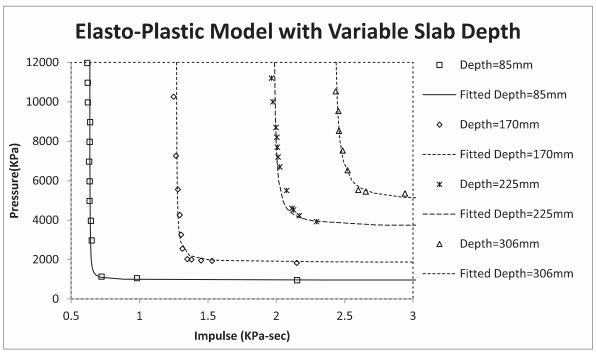

Fig. 17. Pressure–impulse relationships of direct shear failure modes with different *h*.

Table 8
Comparison of P_0 obtained by SDOF and estimated formula.

Validation of P_0 formulation							
$f'c$	f_y (MPa)	ρ	L (span) (mm)	h (depth) (mm)	P_0 (KPa) DOF results	P_0 (KPa) estimated formula	Error (%)
46.9	594	0.028	3000	170	1851	1839	−0.64
60	594	0.028	3000	170	2006	1983	−1.18
46.9	294	0.028	3000	170	1242	1276	2.68
46.9	394	0.028	3000	170	1367	1405	2.81
46.9	594	0.015	3000	170	1421	1414	−0.51
46.9	594	0.019	3000	170	1617	1532	−5.26
46.9	594	0.028	2000	170	2778	2757	−0.76
46.9	594	0.028	5000	170	1015	1047	3.13
46.9	594	0.028	3000	225	3621	3626	0.12
46.9	594	0.028	3000	306	4851	4854	0.08

$$D = \frac{P_{r\max} + K_L m_S \ddot{x}(t)}{2\omega_2^2 m_s} + \frac{y_y(k_2 - k_1)}{\omega_2^2 m_s} \tag{33}$$

For the third condition, the free vibrations response after t_d can be derived as

$$m\ddot{y} + k_2 y + y_y(k_1 - k_2) = 0.5K_L m_S \ddot{x}(t) \tag{34}$$

The solution of this equation is

$$y(t) = A\sin\omega_2 t + B\cos\omega_2 t + C \tag{35}$$

$$y'(t) = A\omega_2\cos\omega_2 t - B\omega_2\sin\omega_2 t \tag{36}$$

Taking the initial condition as $y\ (0) = y(t_2)$, $y'(0) = y(t_2)'$, the constants *A*, *B* and *C* in the above equation can be solved as following:

$$A = \frac{y'_{t_2}}{\omega_2} \tag{37}$$

$$B = y_{t_2} - C \tag{38}$$

$$C = \frac{0.5K_L m_S \ddot{x}(t) + y_y(k_2 - k_1)}{\omega_2^2 m} \tag{39}$$

3.3. Validation of the single degree of freedom system

The validation process aims to validate the SDOF system which is able to effectively predict the response time history through

Table 9
Comparison of I_0 obtained by SDOF and estimated formula.

Validation of I_0 formulation							
$f'c$	f_y (MPa)	ρ	L (span) (mm)	h (depth) (mm)	I_0 (KPa s) DOF results	I_0 (KPa s) estimated formula	Error (%)
46.9	594	0.028	3000	170	1.27	1.30	2.68
60	594	0.028	3000	170	1.38	1.37	−0.34
46.9	294	0.028	3000	170	1.09	1.12	3.40
46.9	394	0.028	3000	170	1.15	1.16	1.33
46.9	594	0.015	3000	170	1.16	1.24	6.69
46.9	594	0.028	2000	170	1.62	1.60	−0.74
46.9	594	0.028	4000	170	1.15	1.10	−4.69
46.9	594	0.028	5000	170	0.98	1.01	2.80
46.9	594	0.028	3000	85	0.64	0.60	−6.74
46.9	594	0.028	3000	306	2.42	2.48	2.43

inputting the structural parameters and charge information. The methodology of this validation process is to compare the time history generated in the real experiments with the predicted values calculated by the SDOF system. However, since there is no example in the literature available which can be used to validate the direct shear SDOF model, the example of an RC slab with specific scales for flexural response is selected to validate the flexural SDOF model in this study. In experiment where the explosion is extremely intensive yet the duration time is relatively short, the overpressure arising from the explosion shall only affect for a limited duration upon the RC slab (2 m × 0.4 m × 0.1 m).

The SDOF system is validated under the circumstance which the high intensity explosion with short duration time may affect the flexural elastic–plastic model. The properties of the simply supported RC slab (one way) applied in this instance are illustrated as in Fig. 5 and the size of the slab is 2 m × 0.4 m × 0.1 m. The slab variables are shown in Table 1. The experimental data are published by Zhu et al. [39].

According to the Ciccarelli et al. [40], the experimental displacement time results can be measured at the center of the slab by adopting LVDT. Those results are then to be compared with the deflection time history generated by using the SDOF system. The prediction of the information of the explosion used in the SDOF system is shown in Table 2. Under the conditions of extremely high peak reflected overpressure and minimal time duration t_d of the explosion, the system flexural response time lasts much longer than the blast duration time t_d. The results of comparing SDOF system's prediction of deflection time history and the experimental data is recorded as shown in Fig. 6. It can be observed that the shape of the predicted deflection time history matches nicely with the experimental curve. With the difference of 15.7%, the measured experimental maximum deflection result is at 0.0336 m while the maximum displacement generated from SDOF system is recorded at 0.0283 m.

4. Assessment of two failure modes for an RC slab

After the validation, the direct shear and flexural failure modes of the RC slab under the external blast loading is modeled by using two SDOF systems. The RC slab 2 m × 0.4 m × 0.1 m is chosen in the current stage. Based on the variables of material strength which regarding to Table 1, the flexural and direct shear strength can be obtained in Table 3.

Krauthammer et al.'s [29] direct shear resistance–slip model of RC members was relied upon for analyzing the shear resistance function of an RC slab. The Krauthammer et al. [29] model is based on research by Hawkins [41], Mattock [42], and Walraven and Reinhardt [43]. It has a tri-linear shear stress–slip relationship following a declining slope and ending with constant shear resistance. The entire model is shown in Fig. 7.

In the present study, the tri-linear model developed by Krauthammer et al. [29] is simplified into a bi-linear model. The simplification is based on the area under the stress–slip diagram remaining a constant, so that the energy absorbed by the system remains the same for both the bi-linear and tri-linear models. Consequently, the corresponding displacement keeps equally as well. Thus the shear slips of the yielding and ultimate capacity are taken as 0.1 and 0.6 mm, respectively.

As can be seen in Fig. 7, when calculating the area under the tri-linear model, the first segment OA represents the elastic response until it reaches the shear capacity τ_e(psi) with the expression

$$\tau_e = 165 + 0.157f'c$$

Then the slope of the curve decreases with the increase of the shear slip until it reaches the maximum shear stress with the following equation. The units of the equation are $f'c$ (psi), f_y (psi) and τ_m (psi).

$$\tau_m = 8\sqrt{f'c} + 0.8\rho_{vt}f_y$$

where ρ_{vt}, $f'c$ and f_y are the reinforcement ratio, concrete strength and yield strength respectively. The softening region was not considered by Krauthammer et al. [44].

Based on the structural properties provided in Table 1, the flexural elasto-plastic response model and direct shear elasto-plastic model are implemented in the present study. The resistance-deflection relationship for the flexural response and the direct shear resistance–slip curve for the RC slab can be obtained as shown in Fig. 8.

By using the obtained resistance/deflection (or slip) functions as in Fig. 8, the analysis of the SDOF system can be based on the derived motion functions presented for the shear response in an elasto-plastic model. Customarily, for the analysis of direct shear response, high reflected overpressure P_{rmax} of short duration is calculated using the motion Equations (4)–(14) followed by Equations (21)–(26). The result relates only to the duration time t_d occurring in the elastic phase of the elasto-plastic model followed by free vibration. P_{rmax} of a comparatively long duration at low reflected overpressure results in direct shear failure, and can be calculated using the motion Equations (4)–(8) and Equations (27)–(39), establishing the resistance response in the plastic phase of the elasto-plastic model.

The typical P–I curves of the RC slab with two failure modes are generated using the SDOF system as shown in Fig. 9. Using this figure, some important characteristics of the two failure P–I curves can be summarized by dividing the plot into four significant regions A, B, C and D which represent a particular situation of the slab under explosion blast load.

In the region labeled C, the slab remains safe without shear and bending failure under the impact loads. In region D, the slab is merely influenced by bending failure without direct shear failure. The area of B presents direct shear failure occurring without flexural failure. The position located in the region of A fails in both direct shear and bending modes. These typical outcomes demonstrate that when a large loading is applied at a rapid rate to the members, the slab is damaged by direct shear force. As shown in the impulsive loading region, the failure area of direct shear mode is much greater than the region of flexural failure. As the failure region is difficult to compare within the dynamic region of the P–I diagram, the failure of the slab could either be the shear failure or bending failure or both failures reinforcing one another. As peak reflected overpressure drops, the failure trends to flexural failure mode in the quasi-static region, which is the safety region in the flexural failure mode, and is smaller than the safety region under the curve in the direct shear failure mode.

5. Assessment of the two failure modes in elastic, plastic and elasto-plastic models

Krauthammer et al. [5] suggest that the two failure modes may not occur at the same time, and that the structure enters the flexural failure mode only if it can survive the direct shear force. However, there is no exact prediction guideline to define whether the RC structure is experiencing a flexural or direct shear failure mode. Based on the research by Ross [3], the peak reflected overpressure–time duration diagram can be divided into two phases. The region under high loading for a short period of time has been classified as the direct shear failure. Regions with lower reflected overpressure over a longer period of time are considered to be experiencing flexural failure. As can be seen from Fig. 10, the peak

reflected overpressure–time histories of two failure modes based on three various structural behaviors are predicted. In both shear and flexural failure modes, the plastic model exhibits the longest time history, followed by the Elasto-plastic model. Peak reflected overpressure decays most quickly in the elastic model. In order to distinguish the difference between the two failure modes, a fitted line is drawn to connect the transition points, as shown in Fig. 10. The direct shear failure modes are assigned to the region above the line, and the rest of the region can be defined as the structure sustaining the flexural failure mode. Therefore, using this method, the RC slab can be separated into the two failure modes.

P–I diagrams can be affected by numbers of parameters such as loading shape, structural behavior or damping. In order to investigate the effect of the peak pressure impulse response on direct shear failure modes with different shear resistance–slip curves, the elastic, plastic and Elasto-plastic models were used in the present study to generate the P–I diagram of the RC slab. The results indicate that variation in P–I diagrams due to different structural behaviors are more prominent in the dynamic region rather than the impulse and quasi-static region (Fig. 11).

Because of the various shapes of the shear resistance slip relationship, the plastic model has the largest impulse, which is incorporated into the longer time in each region of the P–I diagram. Compared to the other two models, a structure represented by an elastic model is one that is relatively easy to damage by direct shear force. This is because the plastic model represents the largest total energy absorption capacity in the SDOF system. The elasto-plastic and elastic models absorb less energy whenever the structure starts to deform. This behavior is more apparent in the dynamic region because the blast loading duration (t_d) and the RC slab's largest response time, which correspond to the largest shear slip, are approximately the same in this region. The greatest energy absorption of the structure therefore occurs when the blast duration and structure response time approach each other in the dynamic region.

In summary, influences of structural behavior on P–I diagrams were investigated by comparing the P–I curves in both flexural and direct shear failure modes in elastic, plastic and elasto-plastic models. The failure regions varied significantly with different resistance-deflection/slip responses (Fig. 11). The overall trend was for the structural models to remain safe when bending failure was recorded in the impulsive regime. The model was more vulnerable to flexural failure in the quasi-static region, and both flexural and shear response appeared to dominate failure in the dynamic region.

These phenomena prove that direct shear failure is more likely to occur in conjunction with high peak reflected overpressure while flexural failure occurs with lower peak reflected overpressure. Furthermore, as shown in Fig. 11, the plastic model has the largest "safe" region unaffected by shear and bending failure under different impact loads. Conversely, the elastic model can sustain relatively less loading in both failure modes due to having the largest failure region.

6. Curve fitting method for generating the P–I curves for RC slabs

Based on the research by Oswald and Skerhut [45], a simple hyperbolic function developed with dynamic SDOF analysis is shown in Equation (40) can produce a curve fitting the transition region for a linearly elastic flexural model. A modification of Equation (40) results in an equation for a perfectly flexural elastic SDOF system subject to rectangular and triangular pulses as approximated by Krauthammer et al. [17]. This is shown in Equation (41), where A and B are the impulsive and quasi-static asymptote respectively. C and D are the approximate constant values. Another curve fitting equation for RC column damage to flexural failure modes under blast loading has been expressed by Shi et al. [46], which is shown in Equation (42).

$$(P-A)(I-B) = 0.4(0.5A+0.5B)^{1.5} \tag{40}$$

$$(P-A)(I-B) = C(A+B)^{D} \tag{41}$$

$$(\mathrm{P}-\mathrm{P}_0)(\mathrm{I}-\mathrm{I}_0) = 12\left(\frac{P_0}{2}+\frac{I_0}{2}\right)^{1.5} \tag{42}$$

In order to present the simplified method of obtaining P–I diagrams for direct shear failure of an RC slab under external blast loading, the curve fitting Equation (43) was used in the present study. The P_0 and I_0 are the impulsive and quasi-static asymptotes, which were calculated by using the SDOF method. The constants n_1 and n_2, which relate to the RC slab configurations, were estimated from an assessment of the RC slab in Section 6.

$$(\mathrm{P}-\mathrm{P}_0)(\mathrm{I}-\mathrm{I}_0) = n_1\left(\frac{P_0}{2}+\frac{I_0}{2}\right)^{n_2} \tag{43}$$

The results of n_1 and n_2, associated with the variables P_0 and I_0, evaluated in relation to the elastic, plastic and elasto-plastic models in Section 6, are given in Table 4. The parameters of Equation (43) are:

Fig. 12 compares the fitted P–I curves which were derived using Equation (43) with the data points obtained using the SDOF system based on various shear resistance models. As shown in Fig. 14, the fitted P–I curves obtained by using the parameters in Table 5 match well with the data points obtained by using the single degree of freedom method. Thus the estimated values of n_1 and n_2 are a reasonable fit to the P–I curve for the elastic, plastic and elasto-plastic models.

In order to ensure that the parameters of n_1 and n_2 in the curve fitting Equation (43) are appropriate for RC slabs with different shear strengths, the curve fitting method is used in the following parametric studies to validate the accuracy of Equation (43). It should be noted that as the elasto-plastic model is the most suitable model for describing the interface shear resistance–slip relationship in an RC slab without considering axial forces, only the elasto-plastic model will be applied in the parametric studies.

7. Parametric studies using an elasto-plastic model

To validate the accuracy of the results for n_1 and n_2 found using Equation (43), the proposed curve fitting method was used to generate P–I curves for RC slabs having a variety of parameters, including concrete strength, steel strength, reinforcement ratio, slab span, depth and width. Transformation of the P–I curves in response to various slab configurations was also investigated. The direct shear Elasto-plastic resistance–slip model was used. The P–I curves generated using the curve fitting method were compared with curves generated using the SDOF method. It needs to notice that despite of modifying any of the variables in the parametric studies, the rest of the parameters however remain consistent with the benchmark, which is revealed in Table 5.

7.1. Concrete strength, $f'c$

The behaviors of the RC slabs with different concrete strengths were analyzed to generate the corresponding P–I curves by using the SDOF and curve fitting methods. Four distinct $f'c$ parameters were used: 30 MPa, 46.9 MPa, 60 MPa and 70 MPa. The impulsive and quasi-static asymptotes corresponding to the

different $f'c$ are listed in Table 6 and the fitted P–I curves are compared with the P–I curves generated by the SDOF method as shown in Fig. 13.

As can be seen in Fig. 13, the P–I curves using $n_1 = 0.0006$ and $n_2 = 1.6$ are a reasonable fit with the points generated by using the SDOF system. The data indicate that as the concrete strength increases, both impulsive and quasi-static asymptotes are rise. These results are expected and demonstrate the fact that the increase in concrete strength contributes to the development of shear strength; thus the "safe area" located under the P–I curve enlarges.

7.2. Steel strength, f_y

In order to investigate the effect of steel strength f_y on the pressure–impulse curves, various steel strengths were tested: 294 MPa, 394 MPa, 594 MPa and 694 MPa. Table 7 shows the changes of the impulsive and quasi-static asymptotes corresponding to the different f_y and Fig. 14 shows its corresponding P–I curves. As can be seen, the fitted curve generated using Equation (43) closely matches the data calculated by the SDOF method. In addition, increases in steel strength result in the increase of both impulsive and quasi-static asymptotes. It can be concluded therefore that the stronger steel strength also improves the RC slab's shear strength.

7.3. Reinforcement ratio, ρ

In order to examine the effect of the reinforcement ratio of RC slabs on P–I diagrams, four different reinforcement ratios were considered as listed in Table 7. The diagrams of the P–I curves are shown in Fig. 15. The outcome is consistent with the conclusion that as a percentage of the reinforced ratio ρ, the RC slab tends to be harder to damage in the direct shear failure mode.

7.4. RC slab span, L (mm)

RC slabs with span lengths of 2000 mm, 3000 mm, 4000 mm and 5000 mm (Table 7) were analyzed to compare the changes in P_0 and I_0 due to changes in span length. As can be shown in Fig. 16, the fitted curve which is generated by Equation (43) is similar to the points generated by the SDOF method. Increasing the slab span increases the likelihood that the RC slab will be damaged. In the SDOF system, an increase in the span of the slab increases the uniform distribution of the blast load acting on the member. This enhances the development of the total uniform distribution of the blast load, which directly leads to greater damage in the shear failure mode, promoting shear failure. The shape of the blast load on the member means that the impulsive and quasi-static asymptotes decrease (Fig. 16).

7.5. RC slab depth, h (mm)

Fig. 17 illustrates the transformation of the pressure–impulse curves as slab depth changes. The values of P_0 and I_0 are recorded in Table 8. The results show that when the depths increase, the corresponding impulsive and quasi-static asymptotes also increase. This is because increasing depth means increasing the cross-sectional area, which enhances the maximum direct shear resistance force of the slab, which makes stronger shear strength. Therefore the P–I curves move towards the right, which means it is harder to do damage using the same blast loading.

8. Prediction of pressure and impulsive asymptotes by analytical formula

Eventually, analytical formulae are generated for predicting the pressure asymptote and impulsive asymptote for the elasto-plastic model. The prediction is based on the results of the parametric studies. The least-squares fit technique, in this instance using Matlab software, was used. The parameters considered were concrete strength $f'c$, steel strength f_y, reinforcement ratio ρ, slab span L and slab depth h. It should be noted that slab width was not considered because it does not significantly influence P–I diagrams.

The formulae of the pressure asymptote and impulsive asymptote of the elasto-plastic model under direct shear failure mode are

$$P_0 = 10000 \times \left[0.0055 \times \exp\left(\frac{f'c}{30}\right) + 0.012 \times \exp\left(\frac{fy}{300}\right) + 0.048 \times \exp\left(\frac{\rho}{0.03}\right) + 0.017 \times \left(\frac{L}{1000}\right)^2 - 0.18 \times \left(\frac{L}{1000}\right) - 1.03 \times \left(\frac{h}{200}\right)^3 + 3.11 \times \left(\frac{h}{200}\right)^2 - 2.45 \times \left(\frac{h}{200}\right) + 0.80\right] \tag{44}$$

$$I_0 = 0.026 \times \exp\left(\frac{f'c}{30}\right) + 0.039 \times \exp\left(\frac{fy}{300}\right) + 0.22 \times \ln\left(\frac{\rho}{0.03}\right) + 0.054 \times \left(\frac{L}{1000}\right)^2 - 0.56 \times \left(\frac{L}{1000}\right) + 0.058 \times \left(\frac{h}{200}\right)^2 + 1.59 \times \left(\frac{h}{200}\right) + 0.72 \tag{45}$$

By using Equations (44) and (45), it is very easy to generate the values of the pressure asymptote and impulsive asymptote based on the parameters of the RC slab. The units used in the formula are P_0 (KPa), I_0 (KPa s), $f'c$ (MPa), f_y (MPa), L (mm), h (mm). After the generation of the pressure asymptote and impulsive asymptote, the next step is to substitute the values of P_0 and I_0 into Equation (43) using $n_1 = 0.0006$ ad $n_2 = 1.6$. Then the corresponding direct shear P–I curves of the RC slabs can be generated.

In order to test the accuracy of Equations (44) and (45), the values of the P_0 and I_0 generated by using these two equations are used to compare with the some specific results of P_0 and I_0 obtained by using the SDOF system. The values for P_0 obtained by the SDOF and the equation are very similar (Table 8). As the difference between these two results is controlled within 6%, Equations (44) and (45) can provide good predictions of the pressure asymptote.

The values for I_0 obtained by the SDOF and the equation are also very similar (Table 9). From the comparison, the results indicate that the error between the SDOF results and the estimated formula results is less than 10%. Thus the above I_0 formula [Equation (45)] also generates a reasonable estimation of the impulsive asymptote as well.

9. Conclusion

The SDOF system is used to develop the P–I diagrams of direct shear failure modes under external blast loading. Three different structural behaviors – elastic, plastic and elasto-plastic models – are used for each model, the performance function formulations are

derived by applying the equivalent structural resistance function into its direct shear SDOF systems.

When the P–I curves of direct shear and flexure failure modes are produced using a typical RC slab, the outcomes indicate that the slab tends to fail in direct shear failure when the magnitude of the peak reflected overpressure is very high and of a relatively short duration. Conversely, the flexural failure tends to occur at low peak reflected overpressure of relatively long duration. In order to predict whether an RC member is in a flexural or direct shear failure mode, a peak reflected overpressure–time response for a structural response is generated. In addition, a fitted line is drawn to connect the transition points in the peak reflected overpressure–time diagram to distinguish the failure modes.

Furthermore, by comparing the P–I diagrams of elastic, plastic and elasto-plastic models in both shear and bending failure modes, the results show that the plastic models most strongly resist blast loading because of their high energy absorption capacity, followed by elasto-plastic and elastic models, respectively. The direct shear and flexural P–I curves indicate that structural models tend to experience shear failure in the impulsive region, and that the model is more vulnerable to flexural failure in the quasi-static region. Both flexural and shear response may dominate failure in the dynamic region.

In order to generate the P–I curve quickly and accurate, a formula is proposed that can predict the P–I curves for the direct shear failure mode of RC slabs. Parametric studies based on the elasto-plastic model were conducted to not only establish the accuracy of the proposed formula but also to investigate the effects on P–I curves of changing several parameters, including span lengths, thickness, reinforcement ratio, concrete strength and steel strength. The final stage of this research is to evaluate the formulae of the pressure asymptote and impulsive asymptote based on the previous parametric studies. When the analytical formulae of the pressure asymptote and the impulsive asymptote are substituted into the curve fitting equation, the pressure–impulse curves of the direct shear failure model under an external blast loading can be established very quickly using the proposed simplified curve fitting method.

Acknowledgments

The research presented in this paper jointly supported by the ARC Discovery Grant DP140103025, and the National Natural Science Foundation of China under Grants 51278326 and 51238007 is gratefully acknowledged.

References

[1] Low HY, Han H. Reliability analysis of direct shear and flexural failure modes of RC slabs under explosive loading. Eng Struct 2002;24(2):189–98.
[2] Smith PD, Hetherington JG. Blast and ballistic loading of structures. Oxford: Butterworth-Heinemann; 1994.
[3] Ross TJ. Direct shear failure in reinforced concrete beams under impulsive loading [PhD thesis]. Standford University; 1983.
[4] Ma GW, Shi HJ, Shu DW. P-I diagram method for combined failure modes of rigid-plastic beams. Int J Impact Eng 2007;34(6):1081–94.
[5] Krauthammer T, Assadi-Lamouki A, Shanaa HM. Analysis of impulsively loaded reinforced concrete structural elements—I. Theory. Comput Struct 1993;48(5):851–60.
[6] Fischer K, Häring I. SDOF response model parameters from dynamic blast loading experiments. Eng Struct 2009;31(8):1677–86.
[7] Abrahamson GR, Lindberg HE. Peak load-impulse characterization of critical pulse loads in structural dynamics. Nucl Eng Des 1976;37(1):35–46.
[8] Fallah AS, Louca LA. Pressure-impulse diagrams for elastic-plastic-hardening and softening single-degree-of-freedom models subjected to blast loading. Int J Impact Eng 2007;34:823–42.
[9] Syed ZI, Mendis P, Nelson TKL, Ngo T. Concrete damage assessment for blast load using pressure-impulse diagrams. In: Kevin MC, Sonja L, editors. Canberra: Australian Earthquake Engineering Society; 2006. pp. 265–74.
[10] Shi Y, Hao H, Li Z. An overview of pressure impulse diagram derivation for structure components. Recent advances in security technology; 2007. p. 179.
[11] Shi Y, Hao H, Li Z. Numerical derivation of pressure-impulse diagrams for prediction of RC column damage to blast loads. Int J Impact Eng 2008;35:1213–27.
[12] Colombo M, Martinelli P. Pressure-impulse diagrams for RC and FRC circular plates under blast loads. Eur J Environ Civ Eng 2012;16(7):837–62.
[13] Fallah AS, Nwankwo E, Louca LA. Pressure-impulse diagrams for blast loaded continuous beams based on dimensional analysis. J Appl Mech 2013;80(5):051011.
[14] Dragos J, Wu C, Haskett M, Oehlers D. Derivation of normalized pressure impulse curves for flexural ultra high performance Concrete slabs. J Struct Eng ASCE 2013;139:875–85.
[15] Wu C, Oehlers D, Rebentrost M, Leach J, Whittaker A. Blast testing of ultra-high performance fibre and FRP-retrofitted concrete slabs. Eng Struct 2009;31(9):2060–9.
[16] Slawson TR. Dynamic shear failure of shallow-buried flat-roofed reinforced concrete structures subjected to blast loading. No. WES/TR/SL-84-7. Army Engineer waterways experiment station Vicksburg ms structures; 1984. pp. 1–129.
[17] Krauthamme T. Pressure-impulse diagrams for the behavior assessment of structural components. Int J Impact Eng 2008;35(8):771–83.
[18] Li QM, Jones N. Blast loading of fully clamped circular plates with transverse shear effects. Int J Solids Struct 1994;31:1861–76.
[19] Jones N. Structural impact. Cambridge: Cambridge University Press; 1989.
[20] Li QM, Jones N. The influence of boundary conditions on the dynamic plastic response of beams and circular plates. Appl Solid Mech 1991;4:52–71.
[21] Li QM, Shu XF. Elimination of loading shape effects on blast loading beams in damping medium. In: Zhang G, Huang SH, editors. Proc. of the 2nd int. symposium on intense dynamic loading and its effects. Chengdu: Sichuan University Press; 1992. pp. 480–3.
[22] Li QM, Jones N. Blast loading of fully clamped beams with transverse shear effects. Mech Struct Mach 1995;23(1):59–86.
[23] Li QM, Jones N. Blast loading of a "short" cylindrical shell with transverse shear effects. Int J Impact Eng 1995;16(2):331–53.
[24] Li QM, Jones N. Shear and adiabatic shear failure in an impulsively loaded fully clamped beam. Int J Impact Eng 1999;22:589–607.
[25] Li QM, Jones N. Formation of a shear localization in structural elements under transverse dynamic loads. Int J Solids Struct 2000;37:6683–704.
[26] Li QM, Jones N. Foundation of correlation parameters for eliminating pulse shape effects on dynamic plastic response of structures. Impact Research Center Report: University of Liverpool.
[27] Li QM, Meng H. Pulse loading shape effects on pressure-impulse diagram of an elastic-plastic, single-degree-of-freedom structural model. Int J Mech Sci 2002;44(9):1985–98.
[28] Li QM, Jones N. Foundation of correlation parameters for eliminating pulse shape effects on dynamic plastic response of structures. Int J Solids Struct 2005;72:6683–704.
[29] Krauthammer T, Bazeos N, Holmquist T. Modified SDOF analysis of RC box-type structures. J Struct Eng (ASCE) 1986;112(4):726–44.
[30] Krauthammer T, Shahriar S, Shanaa H. Response of reinforced concrete element to severe impulsive loads. J Struct Eng 1990;116(4):1061–79.
[31] Krauthammer T. Shallow-buried RC box-typed structures. J Struct Eng ASCE 1984;110(3):637–51.
[32] Low HY, Hao H. Reliability analysis of reinforced concrete slabs under explosive loading. Struct Saf 2001;23(2):157–78.
[33] Krauthammer T. Numerical assessment for blast resistant design. Adv Technol Struct Eng; 2000:1–9.
[34] Luckyram J, Stewart BM, Zintilis GM. Blast loaded R.C. slabs: a binary response model for shear and flexure interaction. In: Bulson PS, editor. Proceedings of the 2nd International Conference on Structures under Shock and Impact. Portsmouth, UK: Computational Mechanics Publications; 1992. pp. 177–88.
[35] Crouch R, Chrisp T. The response of reinforced concrete slabs to non-nuclear blast loading. In: Bulson PS, editor. Proceedings of the first international conference on structures under shock and impact. Cambridge: North-Holland Publishing Co; 1989. pp. 1–534.
[36] Krauthammer T, Assadi-lamouki A, Shanaa H. Analysis of impulsive loaded reinforced concrete structural elemetnsII implementation. Comput Struct 1993;48(5):861–71.
[37] Krauthammer T, Shanaa HM, Assadi A. Response of structural concrete elements to severe impulsive loads. Comput Struct 1994;53(1):119–30.
[38] Vugts K, Pistono T, Jeffrey S, Gee S. Derivation of normalized pressure-impulse curves for a structural member with bilinear resistance function under partially confined blasts [Final year research project report]. Australia: School of Civil, Environmental and Mining Engineering, The University of Adelaide; 2011.
[39] Zhu C, Lin Z, Chia Y, Chong K. Protection of reinforced concrete structures against blast loading [Final year research project report]. Australia: School of Civil, Environmental and Mining Engineering, The University of Adelaide; 2009.
[40] Ciccarelli J, Henderson A, Jorfans K, Noack B. Resistance against explosive loading of metal foam retrofitted and ultra high strength concrete structural members [Final year research project report]. Australia: School of Civil, Environmental and Mining Engineering, The University of Adelaide; 2008.

[41] Hawkins N. The strength of stud shear connections. Civil engineering transactions. Institute of Engineers; 1974. pp. 39–45.
[42] Mattock A. Effect of aggregate type on single direction shear transfer strength in monolithic concrete. Department of Civil Engineering, Univ.of Washington; 1974.
[43] Walraven J, Reinhardt H. Theory and experiments on the mechanical behavior of cracks in plain and reinforced concrete subjected to shear loading. Heron 1981;26(1A):1–68.
[44] Krauthammer T. Modern protective structures. LLC ed. Suite: CRC Press Taylor& Francis Group; 2008.
[45] Oswald CJ, Skerhut D. FACEDAP user's manual. Omaha District: Southwest Research Institute and U.S. Army Corps of Engineers; 1993.
[46] Shi Y, Li Z, Hao H. A new method for progressive collapse analysis of RC frames under blast loading. Eng Struct 2010;32(6):1691–703.

[THIS PAGE IS INTENTIONALLY LEFT BLANK]

Journal Article 2:
Numerical analysis of shear transfer across an initially uncrack reinforced concrete member

[THIS PAGE IS INTENTIONALLY LEFT BLANK]

Statement of Authorship

Title of Paper	Numerical analysis of shear transfer across an initially uncrack reinforced concrete member
Publication Status	✎ Published ☐ Accepted for publication ☐ Submitted for Publication ☐ Unpublished and Unsubmitted w ork w ritten in manuscript style
Publication Details	Engineering Structures, 102, pp.296-309

Principal Author

Name of Principal Author (Candidate)	Juechun Xu		
Contribution to the Paper	Carry out numerical simuations, data analysis and preparation of manuscript.		
Overall percentage (%)	85%		
Certification:	This paper reports on original research I conducted during the period of my Higher Degree by Research candidature and is not subject to any obligations or contractual agreements with a third party that would constrain its inclusion in this thesis. I am the primary author of this paper.		
Signature		Date	21 October 2015

Co-Author Contributions

By signing the Statement of Authorship, each author certifies that:

i. the candidate's stated contribution to the publication is accurate (as detailed above);
ii. permission is granted for the candidate in include the publication in the thesis; and
iii. the sum of all co-author contributions is equal to 100% less the candidate's stated contribution.

Name of Co-Author	Chengqing Wu		
Contribution to the Paper ! !	Guidance of numerical simulations and review manuscript.		
Signature		Date	21 October 2015

Name of Co-Author	Zhong-Xian Li		
Contribution to the Paper	Review of manuscript.		
Signature		Date	25 October 2015

!

[THIS PAGE IS INTENTIONALLY LEFT BLANK]

Engineering Structures 102 (2015) 296–309

Contents lists available at ScienceDirect

Engineering Structures

journal homepage: www.elsevier.com/locate/engstruct

Numerical analysis of shear transfer across an initially uncrack reinforced concrete member

Juechun Xu [a], Chengqing Wu [a,b,*], Zhong-Xian Li [b], Ching-Tai Ng [a]

[a] School of Civil, Environmental and Mining Engineering, The University of Adelaide, Australia
[b] Tianjin Chengjian University & University of Adelaide Joint Research Centre on Disaster Prevention and Mitigation, Tianjin, China

ARTICLE INFO

Article history:
Received 16 March 2015
Revised 14 August 2015
Accepted 14 August 2015
Available online 2 September 2015

Keywords:
Reinforced concrete
Shear transfer
Shear strength
Shear stress to slip relationship

ABSTRACT

An investigation of shear transfer behavior in initially uncracked reinforced concrete members is conducted using finite element modeling method in this study. Although earlier experimental studies have been carried out to identify the role of different design parameters on the ultimate shear strength, there are no design provisions that are available to predict the relationship of shear stress to slip as a function of the basic parameters. One of the aims of this paper is to improve insight into the characteristics between the shear stress and slip for a range of design parameters, such as concrete strength, percentage of dowel and variation of lateral normal pressure on RC members. The other aim of this paper is to derive a set of simplified equations for evaluating the ultimate shear stress and relationship of shear stress to slip in practical structural design. High-fidelity finite element models are developed using LS-DYNA program to simulate push-off tests, and the models are calibrated using experimental results. Parametric studies are then carried out to generate data with the consideration of different combinations of the structural design parameters, i.e., concrete strength, percentage of dowel steel and lateral normal pressures. It is found that the numerical models are accurate in predicting the interface shear strength and slip occurring along the shear plane of the push-off test specimens. The study also shows that there is a good agreement in predicting the shear stress to slip relationship between the results calculated by simplified equations and numerical models, and experimental results.

1. Introduction

Direct shear failure usually occurs in highly stressed interface between two dissimilar concretes such as corbels, bearing shoes, ledger beam bearings, precast concrete assemblies and composite construction [1–4]. In the last decades, numerous studies have been carried out to study shear transfer at an un-cracked plane in reinforced concrete (RC) members [5–7], and hence, to overcome the direct shear failure problem push-off specimens under direct shear testing have been used to greatly improve understanding of the fundamental behavior of the interface shear capacities through experimental observations. It is found that the behavior of shear transfer is largely governed by concrete strength, dowels steel across the interface and constraints in a direction normal to the shear plane [8]. To ensure safety and serviceability of concrete structures, many studies have focused on evaluations of empirical design procedures and developments of empirical equations for shear transfer characteristics [5,6].

For design purposes, different empirical formulas have been proposed for predicting shear strength based on different experiments and theoretical approaches. In the literature two major types of approaches were proposed to evaluate the shear strength across un-cracked plane. The first approach is capable of predicting the full behavior of an interface subjected to both shear and lateral normal stress. It is based on softened truss model theory but massive equations and variables need to be derived from equilibrium, compatibility and material conditions to solve the shear problem [9]. A number of studies have been conducted for evaluating the truss-like action due to the formation of diagonal cracks in initially un-cracked normal and high strength reinforced concrete members using this approach [5–10]. However, the interface morphology and accurate stress–deformation relationships are generally considered to be highly complicated so that the shear transfer behavior cannot be efficiently evaluated for engineering design [11]. The second approach is capable of predicting only the ultimate shear friction capacity. Mattock et al. [12–15] proposed to represent failure conditions of concrete using Mohr circles, and hence, the

* Corresponding author at: School of Civil, Environmental and Mining Engineering, The University of Adelaide, Australia.
E-mail address: cheng.wu@adelaide.edu.au (C. Wu).

http://dx.doi.org/10.1016/j.engstruct.2015.08.022
0141-0296/

Nomenclature

a_i	parameters defining the three-parameters failure surfaces	f_y	specified yield strength of reinforcement
$\sigma_1, \sigma_2, \sigma_3$	principle stresses	μ	coefficient of friction along the interface
$\Delta\sigma$	failure surface for the deviatoric stresses	τ_o	the cohesion
J_2	second invariant of the deviatoric stress tensor	σ_n	the normal stress
T	the stress factor	f_c'	the concrete strength
r_f	strain rate enhancement factor	ρ	the reinforcement ratio
$f_{ct}\, f_{ci}$	strength in uniaxial extension	f_y	is the steel strength
k_d	internal scalar multiplier	$\sigma + \rho f_y$	lateral normal stress
b_i	damage evolution parameters	$\tau_{\max}$	ultimate shear stress
V_n	nominal shear strength	Δ_1	shear slip corresponding to the ultimate shear stress
A_{vf}	the area of shear-friction reinforcement		

expressions of the maximum shear stress can be developed for a range of lateral normal stresses or confinements. However, the limitation of the second approach is that although the joint shear strength is found to be as a function of relative variables, it cannot be used to generalize the empirical function of shear stress to slip relationship. Among the previous publications, there is only one empirical model for describing the shear stress to slip relationship which was proposed by Krauthammer et al. [16]. They presented a tri-linear direct shear resistance-slip model for RC members relied upon analyzing the shear transfer in the static domain without contributions of in-plane compression on the shear strength. However, this model may underestimate the value of shear strength and slip for larger specimens. This is because larger diameter bars usually associated with larger slip at yielding [17]. In addition, the simplified tri-linear model may underestimate the energy absorption capacity under shear failure. Thus this study attempts to rationally predict the shear stress to slip characteristics of a RC member using the mathematical expressions and develops fully-nonlinear resistance functions for describing the shear stress to slip behavior.

As the shear failure of the reinforced concrete structures under static and impact loads has been one of the major safety concerns of designers in recent years. Some experimental studies have been performed to evaluate the shear strength between two concrete layers, and it is widely accepted that the following parameters will contribute to shear strength: the roughness of the substrate surface known as chemical connection between concrete [18,19] and dowel action and friction which appears when relative slippage between concrete layers takes place in the presence of normal stresses to the interface [20]. However, as the requirements and conditions for testing these various effects that contribute to the shear transfer result in the used material properties as well as loading conditions are differing in a tremendous wide range, hence, there is still no general admitted conclusion or prediction of shear stress to slip relationship that can be derived merely based on the existing experimental results. As a consequence, response predictions using physics-based numerical analyses have become important resources for both academics and structural engineers to reliably predict structure damages in a cost effective way.

Therefore, the current study first verifies and validates numerical models using experimental results so that consistent sets of virtual response data can be generated confidently for studying shear behavior and formulating models to support engineers' requirements in design and assessments shear failure. LS-DYNA program is used as a numerical tool to investigate individual parameters affecting the concrete to concrete interface of push-off test specimens and capture the effect of important issues. In the literature the available finite element investigations on the scope of shear transfer of reinforced concrete member are very limited. In the study conducted by Barragan et al. [21], a finite element program (DRAC code) was carried out to obtain the compressive and tensile stress distributions for the push-off test specimens. High compressive stresses occur along the central plane with some tensile stresses near the notch faces, indicating the shear cracking will be present along the ligament zone. However, they merely use this finite element program for predicting the shear response before their experiments, and the validation and shear response study haven't been carried out based on this model. Another numerical model is presented for evaluating shear strength between the two concrete layers by Dias-da-Costa et al. [22], and in their research, the influences of different parameters on longitudinal shear strength between two concrete layers of the push-off specimen have been determined. However, a major limitation is that the focus of these previous studies is to validate the capabilities of numerical modeling of various types of push-off specimens or discuss the effect of vary parameters on shear strength but mathematical expressions of shear-slip behavior have not been further discussed.

Therefore, this study aims to identify the relationship of shear stress to slip for a range of important parameters in concrete member designs, such as concrete strength, percentage of dowel and variation of lateral normal pressure on RC members. With this goal, a finite element model (FEM) is used to simulate the shear behavior of push-off specimens under various loading conditions. The FEM is developed using LS-DYNA program and the FEM is calibrated against the push-off test data. The experimentally calibrated numerical model is then used to carry out parametric studies to identify the effect of each of the most relevant parameters and then to derive mathematical expressions for describing the shear stress to slip relationship. The predicted results are compared with the experimental behavior of the concrete specimens, which were under direct shear loading, in a previous push-off test. A good agreement is found between the predicted results and experimental data.

2. Computational model

A FEM developed using the LS-DYNA program, which was used to simulate the shear behavior of initially uncracked push-off specimens under quasi-static loading, is described in detail in this section. Accurate simulation of reinforced concrete shear panel subjected to direct shear load is challenging. The simulation includes prediction of bond contact between concrete and steel, selection of material models that is capable of simulating the behavior of direct shear failure and highly refined meshing for simulating the fracture patterns observed in the tests. One of the essential requirements of using the FEM to predict the direct shear behavior of concrete members is to have a detailed verification of

material model using experimental test results. The numerical model developed in this study was validated with the push-off tests, which were carried out at the Smith-Emery Concrete Testing Laboratory in order to ensure the accuracy and reliability of the numerical model [23]. The push-off specimens were designed by Karagozian & Case [23].

2.1. Specimen geometry

For the initially uncracked push-off specimen, the basic configuration of a typical specimen with size of 254 mm × 914.4 mm × 254 mm as well as a critical shear cross section 139.7 mm × 228.6 mm is shown in Fig. 1. As shown in the figure, the 57 mm deep notch at the shear plane was designed to reduce the shearing cross section so that shear failure would occur prior to specimen failure at other critical locations. All models contained #5 (Nominal Area 200 mm^2) longitudinal reinforcements to avoid any local failures. In addition to the vertical bars, the closed steel stirrups across the shear plane were typical #3 (Nominal Area 71 mm^2) reinforcing bars. Details about the push-off specimens can be found elsewhere [23].

To save the computational time, only half of the experimental setup was considered due to the symmetry of the push-off specimen. The steel dowels, which induced a compression stress across the joint and the longitudinal reinforcing bars, were used adjacent to the shear plane to improve the compression strength of the critical section. They were modeled as embedded one-dimensional elements (linear truss elements) tied to the concrete region.

2.2. Material model

2.2.1. Concrete

To obtain a reliable prediction of concrete behavior under direct shear load, a proper model that reflects the characteristics of concrete material behavior is crucial. The Concrete_Damage_Rel3 (MAT_72_REL3), which is three independent yield failure surfaces with shear dilation, concrete damage surfaces and has an origin based on the Pseudo-Tensor Model (Material Type 16), is used to simulate concrete in this study. This model has been tested and used extensively by many researchers for analyzing RC structures subjected to quasi-static, blast and impact loads, and its validation and application have been reviewed comprehensively by Crawford et al. [24]. By using this model, the maximum failure surface of concrete is expressed as [25]:

$$\Delta\sigma/f'c = a_0\left(\frac{p/f'c}{a_1 + a_2 p/f'c}\right) \tag{1}$$

where

a_i = parameters defining the three-parameters failure surfaces;
$p = (\sigma_1 + \sigma_2 + \sigma_3)/3$,
$\sigma_1, \sigma_2, \sigma_3$ = principle stresses

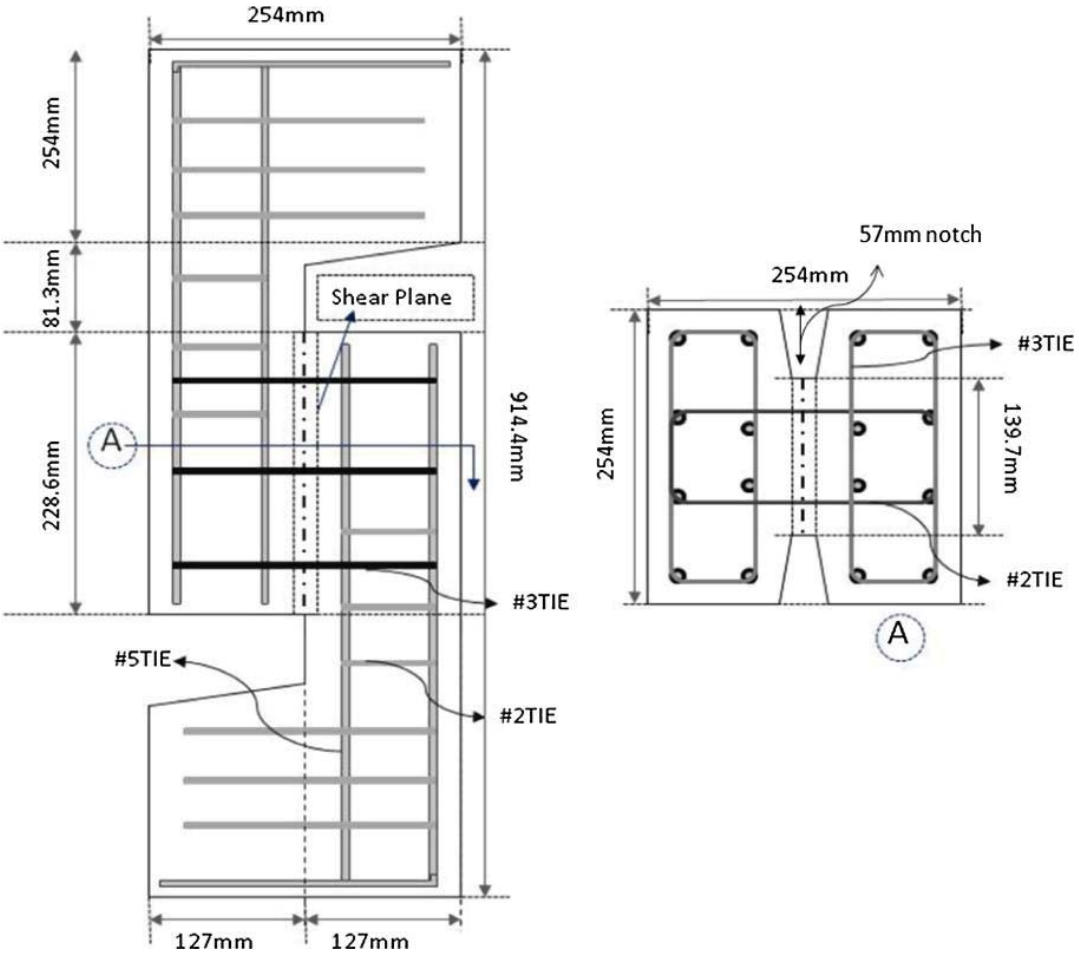

Fig. 1. Typical push-off test specimen.

$\Delta\sigma = \sqrt{3J_2}$ = failure surface for the deviatoric stresses
$J_2 = (S_1^2 + S_2^2 + S_3^2)/2$ = second invariant of the deviatoric stress tensor

For the shear damage accumulation [26], the failure surface is interpolated from the maximum failure surface and either the yield or the residual failure surface as

$$\Delta\sigma = \eta(\Delta\sigma_m - \Delta\sigma_{\min}) + \Delta\sigma_{\min} \tag{2}$$

where $\Delta\sigma = \sqrt{3J_2}$, $\Delta\sigma_{\min}$ is either $\Delta\sigma_y$ or $\Delta\sigma_r$ depending on whether $\lambda \leqslant \lambda_m$ or $\lambda > \lambda_m$, and η is a function of λ. The modified effective plastic strain λ is defined as

$$\lambda = \begin{cases} \int_0^{\bar{\varepsilon}_p} \dfrac{\overline{d\varepsilon_p}}{\gamma_f\left(1+\frac{p}{f_{ct}}f_{ct}\right)^{b_1}}, & p \geqslant 0 \\ \int_0^{\bar{\varepsilon}_p} \dfrac{\overline{d\varepsilon_p}}{\gamma_f\left(1+\frac{p}{f_{ct}}f_{ct}\right)^{b_2}} + b_3 f_d k_d(\varepsilon_v - \varepsilon_v^{yield}), & p < 0 \end{cases} \tag{3}$$

where

$\overline{\varepsilon_p} = \sqrt{\frac{2}{3}\varepsilon_{ij}^p \varepsilon_{ij}^p}$,
$p = -\frac{1}{3}tr(T)$ and T is the stress factor
r_f = strain rate enhancement factor
f_{ct} = strength in uniaxial extension
k_d = internal scalar multiplier
b_i = damage evolution parameters

$$f_d = \begin{cases} 1 - \frac{|\sqrt{3J_2}/p|}{0.1} & \text{for } |\sqrt{3J_2}/p| < 0.1 \\ 0 & \text{for } |\sqrt{3J_2}/p| \geqslant 0 \end{cases} \tag{4}$$

One of the advantages of using this model is that all the input parameters for constructing the damage function can be automatically generated by requiring the unconfined compressive strength and density of the concrete. However, all aspects of the concrete material model could not be accurately characterized by only using these two parameters. In the preliminary study, the results using default values for these parameters shows ascending branch of stress slip curves and ultimate shear stress agreed well for MAT72_REL3. However, when the steel being yield and aggregate interlock, friction is the major mechanism governing the response; under this situation, relatively large deviation was observed for the ultimate shear slip and the portion of the descending curve. In order to capture a more accurate representation of the shear transfer of softening phase, the default values of Concrete_Damage_Rel3 (MAT_72_REL3) model must be corrected by the user manually. As shown from the previous studies associated with the shear damage accumulation; because the amount of expansion and the strain are related to the values chosen for damage evolution parameters and the λ–η function; therefore both λ–η function and the softening parameters b_1, b_2, and b_3 were considered as possible ways to improve the softening performance of the shear transfer model. For considering the adjustment of b_1, as the default value is correct only for a 4-in. element, for which it was developed, thus the parameter b_1 must be adjusted to reflect the mesh size of the current model. The defining b_1 as a function of element size h could most easily be addressed by using the relationship $b_1 = 0.34h + 0.79$. Furthermore, as the damage scaling exponent b_2 will also affect plastic straining by modifying the relation between increments of effective plastic strain $d\bar{\varepsilon}_p$ and damage parameter λ, therefore the selection of b_2 needs to be specified according to aggregate size by using the table provided by Karagozian & Case [23]. Lastly, as there is no direct data to select the parameter b_3, the value for b_3 needs to be justified between 1.1 and 1.6 for best fitting the shear stress to slip curve [27].

2.2.2. Crack propagation simulation

For considering the physical crack propagation simulation, a new element erosion criterion was proposed in order to capture the crack patterns. An external erosion algorithm named the Mat_Add_Erosion is used along with Concrete_Damage_Rel3 (MAT_72_REL3) model. This erosion model is based on the concept that the erosion failure criterion of concrete elements is the maximum tensile strain, i.e. failed elements are ignored in further computation. The failure criteria are defined on an empirical basis in the current study. According to the research proposed by Xu and Lu [28], typical concrete strain at peak tensile stress under static loading is about one-tenth of that at peak compressive stress (it is around 0.0002). By taking the softening phase into consideration, the concrete at fracture with practically complete loss of tensile strength could be assumed as five times of the concrete strain at peak tensile stress under static loading, i.e. it is 0.001. However, as the deletion process is irreversible, the material is not able to offer further resistance once it reaches the failure criterion. Therefore this simulation with the strain based erosion can accurately capture the shear crack patterns; however, they may slightly underestimate the softening and the dissipated energy.

2.2.3. Reinforcement

In order to simulate the response of steel reinforcements, beam elements, with material model PLASTIC_KINEMATIC (MAT_003) were used in this study. This material model is suitable to model isotropic and kinematic hardening plasticity, i.e. the behavior of reinforcing steel. In this material model, the elastic behavior of steel material is defined by Young's modulus (207 GPa), Poisson's ratio (0.28) and yield stress (340 MPa). The plastic behavior is defined by tangent modulus but the strain rate effects were not considered in the model.

2.3. Bond slip

The shear stress transfer behavior between the concrete and reinforcement through bond plays an important role in the shear stress capacity of reinforced concrete structures. It should be noted that for considering the interface between concrete and steel, the bond action of the steel bars to the shear stress transfers across the cracks in concrete were treated as additional stresses acting between beam elements (reinforcements) and concrete solid elements by using the one-dimensional slide line contact algorithms, CONTACT_1D, in LS-DYNA. The kinematic constraint consists of placing normal interface springs to resist interpenetration between element surfaces. When the slave nodes of truss elements (modeling the reinforcements) penetrate the master solid elements (modeling the concrete matrix), the algorithm automatically detects it and applies an internal force to the nodes (represented by the fictitious springs) to resist penetration, i.e. keep the slave nodes outside the surface of master solid elements [29]. Based on the approach proposed by Shi and Li [30], the three parameters, which are bond shear modulus, the maximum elastic slip and the damage curve exponential coefficient, can be defined for the contact model.

3. Validations and discussions

3.1. Validation with experimental data

The main target of the present validation is to compare the results of finite element analysis with the actual experimental

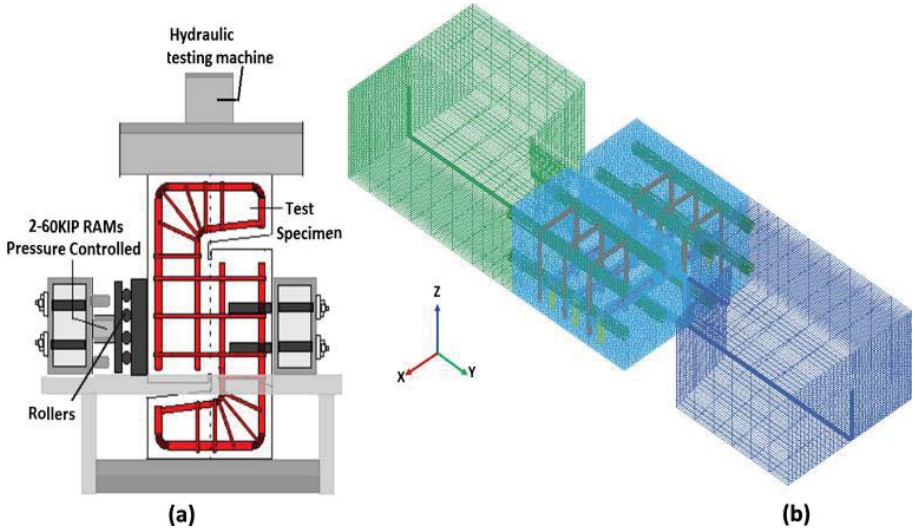

Fig. 2. (a) Experimental set up [26] and (b) LS-DYNA specimen model.

data. Based on the experimental results of the reinforced concrete specimen (as shown in Fig. 1) under construction joint test program performed by Karagozian & Case [23], a nonlinear finite element method is adopted to numerically analyze their behaviors and explore the influence of parameters on the shear behaviors of push-off test specimens. The experimental program is briefly discussed in the following paragraph and full details can be found in the report [23].

The un-dimensional sketch of the experimental fixture is shown in Fig. 2(a). The fundamental purpose of this test set up was to apply vertical load of 2669 kN (600 kips) through a hydraulic machine to force upper half of the specimen moving downward and induce a lateral pressure in horizontal direction using two 267 kN (60 kips) hydraulic rams powered by a hydraulic pump [23]. In order to ensure the test data covering different combinations of the three variables, i.e., concrete strength, joint reinforcement and lateral normal pressure in the experimental program, the specimens were classified as 7 casts with range of concrete strength from 25.7 MPa (3750 psi) to 48.3 MPa (7000 psi) for three joint conditions, i.e., monolithic, sandblast and wash. For the current study, the specimens fabricated in the monolithic conditions were modeled in the simulation. During the experiment, these specimens were performed under an applied vertical load up to 1.93 kN (433 lbs) and the lateral normal pressure applied by the hydraulic rams was varying from 56.05 kN (12,600 lbs) to 336.29 kN (75,600 lbs). Two dial gages were used to measure the slip during the elastic to plastic phase. The shear stress to slip relationship for the chosen six specimens were categorized into two groups based on the concrete strength and the LS-DYNA simulation results are compared within each group.

Fig. 2(b) indicates the FEM of the push-off test specimen. In order to be consistent with the test frame and loading apparatus as shown in Fig. 2(a), the boundary conditions need to be considered carefully in the numerical model. In this study symmetrical constrains were utilized to reduce the model size by half; the z translational, x and y rotational degree of freedom were fixed in the numerical model so that the push-off specimen is symmetrical in the z directions. In the experiment setup, the loading head assembly was designed to allow the applied force to be distributed evenly over the top surface of the specimen and the bottom of the specimen was placed on the floor. Thus, all the nodes at the bottom surface of the numerical model were restrained in both translational degrees of freedom in order to prevent movements and rotations while the top surface was prescribed a displacement by setting the *BOUNDARY_PRESCRIBED_MOTION_SET to follow a linear motion with a total displacement. Furthermore, there was a yoke consisting of structural box member with adequate strength and stiffness, and four cross bolts surrounded the specimen during the test [31]. In the simulations of adding lateral normal force, the outer vertical surface, which was connected to the lower L-shape base of the specimen, was constrained against horizontal motions (i.e., in the x and z direction). It should be noted that there was a prescribed displacement allowed in the opposite outer surface so that the left half of the specimen moves toward to right direction under a displacement controlled condition.

Eight-noded hexahedron solid elements were used to model the concrete in this study. A mesh refinement test was carried out in this study. Preliminarily, the original mesh size of the concrete and dowel steels across the shear plane was 1 mm × 4 mm × 4 mm as shown in Fig. 3(a). Once the load deformation behavior simulated by using this mesh size was acceptable, it was then refined to a meshing with a combination of different mesh sizes. The size of the finer elements remained the same in the region of shear plane (0.000505 m^3) while the element size in the region outside the shear plane was increased to have characteristic length of 4 mm. Both the original and refined mesh sizes and their corresponding lateral normal stress along the section depth are depicted in Fig. 3. Numerical convergence study shows that further refining the mesh size only has little effect on the numerical results, in which an average difference within 2% was found in the results simulated by the models with the two different meshes but the computational time of the refined mesh was reduced significantly. As a consequence, the further analysis and parametric study were performed using the refined mesh as shown in Fig. 3(b).

The numerical simulations of the typical shear stress–slip curves were compared with the representative test responses. Table 1 shows the details of the comparison between the maximum shear strength calculated by the FEM and the measured experimental data. The experimental results are grouped into two categories, the major variables among the groups are the concrete strength and normal pressure. The Casts 6.2 M-A, M-D, M-G have average concrete strength 34.37 MPa (4985 psi) and two #3 dowel steel bars across the joint. The Casts 7.2 M-A, M-D, M-G have

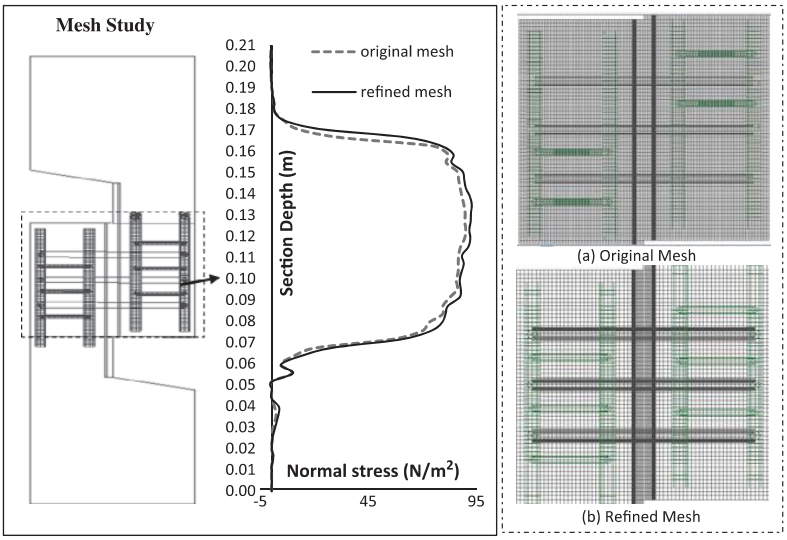

Fig. 3. Results of convergence study, a) original mesh and b) refined mesh.

Table 1
Validation with experimental data.

Sample mark	Concrete strength $f'c$ (MPa)	Normal pressure (MPa)	Dowel steel area (mm^2)	Shear area (mm^2)	Experimental maximum shear strength τ (MPa)	Simulated maximum shear strength τ (MPa)	Error %
Cast 6.2 M-A	34.37	0	142	31,645	8.01	7.59	5.5
Cast 6.2 M-D	34.37	2.76	142	31,935	12.19	11.6	5.0
Cast 6.2 M-G	34.37	5.52	142	32,516	16	15.6	2.5
Cast 7.2 M-B	48.54	0	142	32,226	10.21	9.82	3.9
Cast 7.2 M-D	48.54	2.76	142	32,226	14.84	14.1	5.2
Cast 7.2 M-G	48.54	5.52	142	32,226	17.26	17.7	2.4

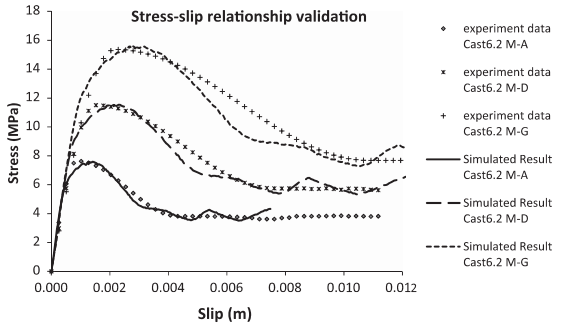

Fig. 4. Validation of Cast 6 specimens.

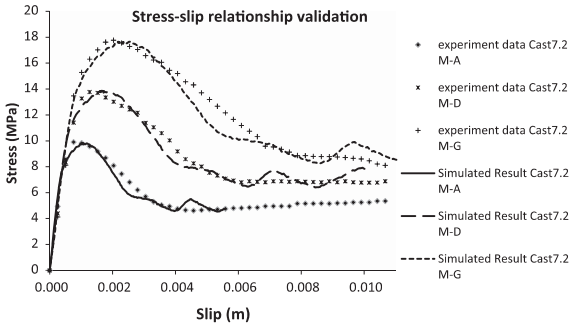

Fig. 5. Validation of Cast 7 specimens.

the same dowel steel areas but different concrete strengths (48.5 MPa i.e., 7040 psi). In all validation cases, the labels A, D, G indicate the specimens have different lateral normal pressures 0 MPa (0 psi), 2.76 MPa (400 psi) and 5.52 MPa (800 psi), respectively.

Fig. 4 shows the shear behavior of Casts 6.2 M-A, M-D, M-G specimens and Fig. 5 shows shear stress–slip curves for specimens Casts 7.2 M-B, M-D, and M-G. It is clearly shown in Figs. 4 and 5 that good agreements are found between the simulated shear transfer behavior and experimental results for all the selected specimens. The behaviors of the LS-DYNA simulations are almost identical to the experimental results with only little discrepancy that the simulated results have a lower stress for both pre-cracking and post-cracking stages. This may be due to the application of the external erosion algorithm as explained previously. In the case of specimens with the same concrete strength, similar rising trend of shear transfer behavior with the lateral normal pressure is found from both numerical simulations and experimental data. It is obvious that lateral normal force and tensile reinforcement play a significant role in the behavior of shear transfer. Table 1 also shows that there is an overall good agreement between the simulated ultimate direct shear stresses and the measured results from the experiments. The maximum error is only 5.5%. The examinations of these data also support the concepts that, for similar specimens, the increase of the normal pressure and concrete strength would directly improve the maximum shear transfer capacities.

After the validation of the LS-DYNA model, the fitting curve of the shear stress to slip relationship was analyzed based on typical simulation and experimental results in the next section. Afterward, the LS-DYNA model was applied to consider different combinations of lateral normal pressures, reinforcement ratios and concrete strengths in the following parametric studies. The regression analysis was then carried out for evaluating the expressions of the ultimate shear stress and direct shear stress to slip curves.

3.2. Simulation results

A specimen with concrete strength 65 MPa and six dowel steels across the shear plane under 6 MPa lateral normal pressure was analyzed and it was used as a typical example in the current stage. The simulated results of the maximum shear stress of the x–y plane of the specimen under six typical shear slip (Δ_y) conditions are presented in Fig. 6. The entire shear stress to slip relationship of the model during the loading conditions is shown in Fig. 7. It should

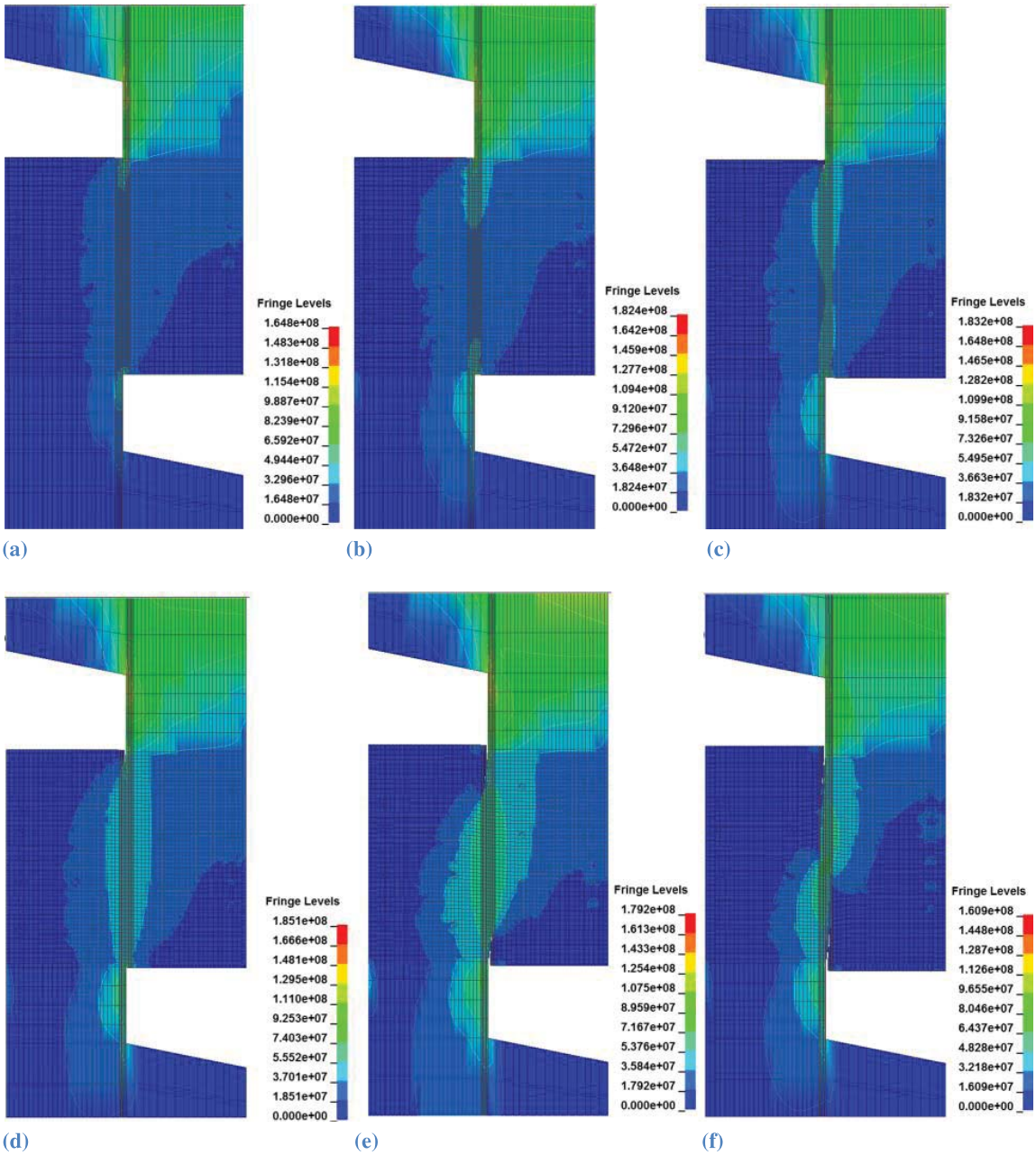

Fig. 6. LS-DYNA simulation results of shear stress. (a) Shear stress for Δy = 0.8 mm, (b) shear stress for Δy = 1.5 mm, (c) shear stress for Δy = 2.0 mm, (d) shear stress for Δy = 2.9 mm, (e) shear stress for Δy = 5.5 mm, and (f) shear stress for Δy = 7.7 mm.

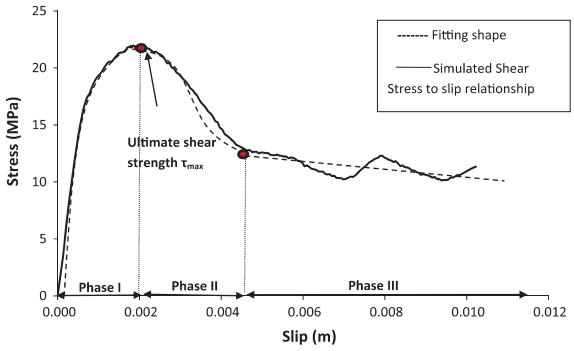

Fig. 7. Typical shear stress–slip relationships.

be noted that the nominal shear stress was obtained by dividing the shear force along the shear plane (in *y*-direction) by the nominal shear-plane area (139.7 × 228.6 mm^2). To clarify the shape of the shear stress–slip curve, a fitting curve with three different phases is shown in Fig. 7. The figure characterizes the shear stress–slip curve as the initial elastic behavior (Phase I), yielding of reinforcements (Phase II) and slip occurred under constant or decreasing load (Phase III).

As shown in Fig. 7, a practically ascending response can be observed up to the peak stress in Phase I, in which the typical shear stress across the shear plane for shear slip varies from 0.8 mm to 2.0 mm. Fig. 6(a)–(c) shows the shear stress at each value of these shear slips. As shown in Fig. 6(a)–(c), because the surface at joint area begins to deform with increasing load, it starts to stress the reinforcing bars birding the joint area until the reinforcement crossing the crack begins to yield and the ultimate strength is attained. Fig. 6(d) shows the peak point with shear slip = 2.9 mm. Afterward, there is a significant reduction in the shear force immediately upon the attainment of the ultimate strength (Phase II). Within this phase, any attempt to increase the applied load would lead to large deformation at the reinforcing bars and subsequently the reinforcements become the major contribution to the shear strength. The observation reveals that the dowels are severely bent, and hence, the residual shear strength is provided mainly by the steel bars. They continue to resist the load due to possible strain hardening and this plastic region has an almost constant shear stress. The shear slip from 5.5 mm to 7.7 mm (Fig. 6(e) and (f)) has been chosen as an example to show the maximum shear stress in Phase III. Finally, the bars shear off leads to a sudden reduction in the shear strength. Most of previous studies focused on developing the empirical equations for the peak shear stress but the prediction of the shear stress to slip relationship has still not well explored. Thus the next section focuses on developing an empirical shear transfer model for describing the shear stress to slip relationship.

4. Parametric studies

In order to assess the influences of different parameters on shear strength, the parametric study program consisted of 36 un-cracked push-off models were examined in the current stage. The key test parameters were the reinforcement ratio, lateral

Table 2
LS-DYNA model program and results.

Series	Name	No. of dowel steel	Normal pressure σ_n (kPa)	$\rho f_y + \sigma_n$ (MPa)	Concrete strength (MPa)	Maximum shear stress (MPa)	Maximum shear slip (m)
A	A-01	2	0	1.53	35	6.93	0.0014
	A-02	2	3000	4.53		11.56	0.002
	A-03	2	6000	7.53		13.95	0.0037
	A-04	2	10,000	11.53		15.60	0.0036
	A-05	4	0	3.06		9.25	0.0015
	A-06	4	3000	6.06		13.52	0.0022
	A-07	4	6000	9.06		15.48	0.0028
	A-08	4	10,000	13.06		15.83	0.0038
	A-09	6	0	4.6		11.32	0.0018
	A-10	6	3000	7.6		15.02	0.0027
	A-11	6	6000	10.6		15.83	0.0029
	A-12	6	10,000	14.6		16.06	0.0035
B	B-01	2	0	1.53	50	9.59	0.0011
	B-02	2	3000	4.53		14.44	0.0015
	B-03	2	6000	7.53		19.06	0.002
	B-04	2	10,000	11.53		20.22	0.0022
	B-05	4	0	3.06		12.13	0.0014
	B-06	4	3000	6.06		17.79	0.0017
	B-07	4	6000	9.06		19.76	0.0019
	B-08	4	10,000	13.06		20.91	0.002
	B-09	6	0	4.6		14.67	0.0016
	B-10	6	3000	7.6		19.29	0.002
	B-11	6	6000	10.6		20.45	0.0028
	B-12	6	10,000	14.6		21.37	0.003
C	C-01	2	0	1.53	65	10.86	0.0011
	C-02	2	3000	4.53		16.75	0.0013
	C-03	2	6000	7.53		21.37	0.0017
	C-04	2	10,000	11.53		25.19	0.002
	C-05	4	0	3.06		13.52	0.0012
	C-06	4	3000	6.06		19.64	0.0016
	C-07	4	6000	9.06		23.11	0.0022
	C-08	4	10,000	13.06		25.42	0.0027
	C-09	6	0	4.6		17.33	0.0014
	C-10	6	3000	7.6		21.95	0.0018
	C-11	6	6000	10.6		24.26	0.0022
	C-12	6	10,000	14.6		26.01	0.0029

normal stress and compressive strength of the concrete. The reinforcement parameter varied by changing the bar numbers without changing the bar size. The models were divided into three series, designated A, B and C in Table 2 according to the concrete strength that varied from 35 MPa to 65 MPa. In each series, they were further divided into three groups regarding to the amount of ties crossing the shear plane with variation from two to six and the lateral normal pressures applied to each group of models also varied from 0 kPa to 10,000 kPa.

4.1. Simulation results and discussion

Fig. 8 presents the shear stress to slip relationships for the 36 models with different concrete strengths and normal pressures. General speaking, all the models in this section behave in a similar manner. The appearance of typical curve fitting shape, which represents the loads vs. slip at shear plane, is shown in Fig. 8. The shear stress first increases with the slip. Once the shear stress reaches the maximum value, it then deceases and fluctuates around a slightly decreasing trend line in the final stage. The results of all models look similar except for the magnitude of the ultimate shear stress. The detailed discussion of the effects of concrete strength and reinforcement parameters is made in the following paragraphs.

As shown from the stress–slip curves of these models, all of the curves initially respond linearly and the strength reinforcement parameters have very little influence at this stage. After that the reinforcement starts elongating as it is being stretched due to the applied load. The shear stress–slip curves then become nonlinear until it reaches the ultimate point. The specimens with higher value of concrete strength and reinforcement parameter exhibit stiffer stress–displacement responses, leading to an enhancement in the ultimate shear strength.

For assessing the effects of reinforcement parameter on the ultimate shear strength, Fig. 9 compares the ultimate shear stress of three different dowel steel conditions (i.e. two, four and six) used in different series with different concrete strengths and normal pressures. It is clearly shown that the curves are considerably different with increase of concrete strength and normal pressure. For the curves drawn through points of constant lateral normal pressure, there is a higher increase in the slope of the curves at lower lateral normal pressure cases (01-05-09 with normal pressure = 0 MPa in each series A, B, C) than the higher lateral normal pressure cases (04-08-12 with normal pressure = 10,000 MPa in each series A, B, C). This situation also agrees with the concept mentioned by Hofbeck et al. [12]: for initially uncracked specimen, although the dowel action may contribute to increase the ultimate shear strength, the effects of reinforcements is not as significant as

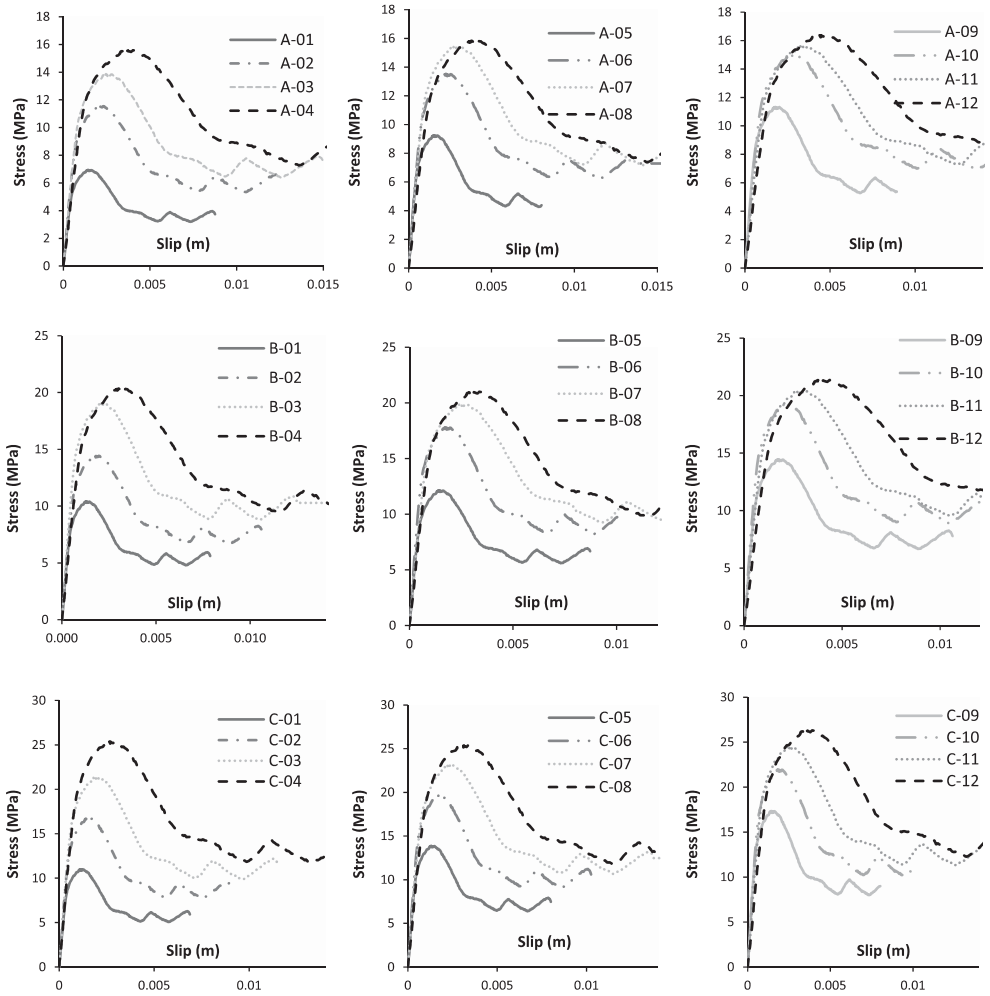

Fig. 8. Simulated shear stress–slip curves for all the models.

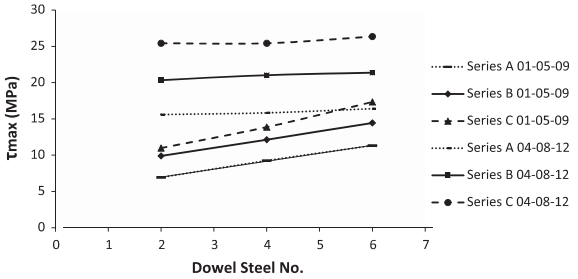

Fig. 9. The ultimate shear stress vs. dowel steel number.

the contributions of normal pressure and concrete strength to the maximum shear strength.

As shown in Fig. 8, after the ultimate point, as demonstrated by [31], the slope of load to slip curve decreases as the dowel steel continues to resist the load after the failure of the joint. Finally, the shear stress appears as slightly decreasing trend line with values about 60% of the ultimate shear for most of the models.

5. Shear stress–slip relationship

5.1. Theoretical considerations

In this section, the theoretical considerations of deriving ultimate shear stress and corresponding shear slip are discussed. Basically, although both initially cracked and un-cracked concrete are referred to as direct shear failure in the static sense, the basic behavior of shear transfer strength of these two cases are different, as long as slip occurs along the cracked shear plane [10,31]. For initially cracked joint, based on the push-off tests by Hanson [32] and Anderson [33], the shear friction hypothesis, which defines the shear friction as the frictional resistance of cracks to sliding, was proposed by Mast [34], and Birkeland and Birkeland [35]. Subsequently, this shear friction theory was adopted by many researchers, such as Hofbeck et al. [36]. As a result of the above works, the provisions for design using shear friction in the ACI Building Code, ACI 318-99 [37] are shown in the following:

$$V_n = A_{vf} f_y \mu \tag{5}$$

where V_n = nominal shear strength, A_{vf} = the area of shear-friction reinforcement, f_y = specified yield strength of reinforcement, μ = coefficient of friction along the interface.

However, this code is based on the assumption that a crack exists in the shear plane before shear force is applied on it [15]. Therefore, only data obtained from the initially cracked specimens were considered when developing design provisions, and hence, this design code may not reflect the true shear behavior of the initially un-cracked shear plane.

To determine the stress state of the initially un-cracked push-off shear plane, a graphic representation using the Mohr's circles, where the influences of various parameters were considered, is shown in Fig. 10. According to the approach proposed by Mattock and Hawkins [13] and Mattock [14], for determination of the magnitude of the maximum shear stresses τ_{max} due to the combination of the lateral normal stresses σ_x and applied force V, the failure envelope of concrete needs to be constructed first. A series of Mohr circles can be drawn tangent to the failure envelope and the diametrically opposite points corresponding to the intersection of the circle. In this graph τ axis or axis with angle θ ($\theta = \tan^{-1}\frac{V}{\sigma_y}$) is on the two curves, representing the combinations of shear stress

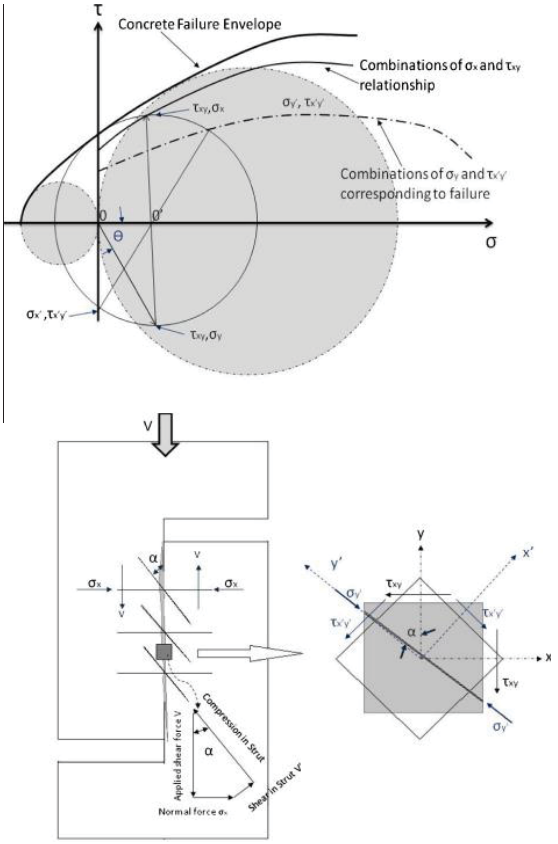

Fig. 10. Construction of relationship between shear stress and normal stress in initially uncracked push-off specimen using Mohr circles.

and lateral normal stress parallel to the short diagonal tension crack and shear plane, respectively.

Base on the research proposed by Haskett et al. [38], the relationship between lateral normal stress and shear stress as shown in Fig. 10 can be simply treated akin to a Mohr–Coulomb failure envelope. The two parameters, coefficient of friction and cohesion term (the intercept of the failure envelope with the ordinate) can be determined for both initially cracked and uncracked concrete. Thus the shear strength in concrete can be simplified as a function of normal stress as below:

$$\tau = \tau_0 + \mu\sigma_n \tag{6}$$

where τ_o is the cohesion, μ is the coefficient of friction and σ_n is the normal stress.

In the current study, the shear friction analysis of an initially un-cracked shear plane is presented. By normalizing the concrete strength, the function for the upper bound of shear stress was first evaluated by justifying the Mohr–Coulomb expression in terms of the sum of the normal pressure plus the yield strength of the dowel steels. Afterward, the method proposed by Mattock and Hawkins [13] and Mattock [14] was also applied to calculate the ultimate shear strength. A comparison between the results obtained by these two approaches was conducted. Ultimately, the aim of this paper is to illustrate the analytical techniques so that the shear friction parameters can be determined using the regression analysis to evaluate the function for describing the shear stress to slip relationship.

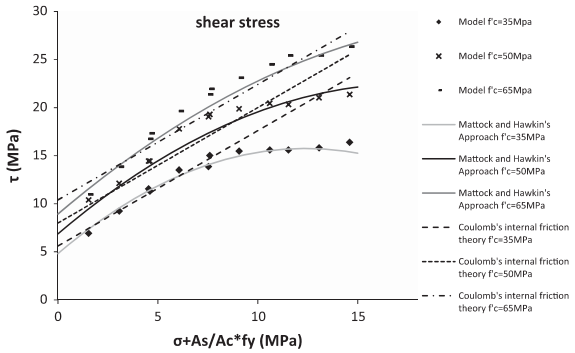

Fig. 11. The ultimate shear stress vs. normal stress.

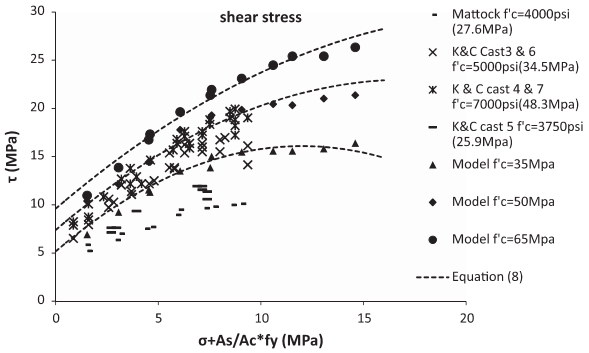

Fig. 13. Assessment of equation for the ultimate shear stress.

5.2. Ultimate stage

5.2.1. Ultimate shear stress

To define the ultimate stage, the maximum shear stress and its corresponding shear slip were evaluated based on the equivalent lateral normal stress, i.e., reinforcement parameters plus the lateral normal pressure are shown in Figs. 11 and 12. As shown in Fig. 11, the increase of the concrete strength $f'c$ from 35 MPa to 50 MPa, the models with the same lateral normal stresses have an average of 24% increase in the shear strength and an increase in concrete strength from 50 MPa to 65 MPa results in an increase in the shear strength by 14%. For the values of lateral normal pressure below 9 MPa, the lateral normal stress does appear to affect the shear transfer strength with a big increasing slope. However for normal stress values exceeding 9 MPa, the increasing slope of the maximum shear stress is not as great as the increasing slope of τ_{max} with lower lateral normal stress. As seen from Fig. 11, based on the Coulomb's internal friction theory, the failure of the material is caused by a sliding action along a certain plane within the material, the resistance to sliding plane is composed by a constant shearing strength τ_0 [39], and the internal friction is proportional to the lateral normal stress. To use this method, the best estimated shear stress is derived as below:

$$\tau = 0.16f'c + 1.2(\sigma_n + \rho f_y) \quad (7)$$

where $f'c$ is the concrete strength, σ_n is the lateral normal pressure and ρ is the reinforcement ratio and f_y is the steel strength.

However, it is clear that this coulomb expression based equation is not accurate enough to predict the shear stress for the higher values of lateral normal stress. Based on the theory proposed by Mattock and Hawkins [13], the shear stress vs. normal stress relationship based on concrete failure envelope obtained by using the Mohr's circles shown in Fig. 10 is plotted in Fig. 11 and these curves have a relatively good agreement with the simulated data, in which the error is within 10%.

5.2.2. Shear slip corresponding to the ultimate shear stress

Fig. 12 shows the shear slip corresponding to the maximum shear stress with increasing equivalent lateral normal stress and their normalized relationship. Contrary to the phenomena of shear stress, the slip at the ultimate state slightly decreases with an increase of the concrete strength. The decrease may attribute to the higher bond developed at the interface of dowel steels and concrete matrix for higher strength concrete. Despite of the effect due to concrete strength, Fig. 12 shows the normalized shear slip diagram. There is almost linearly ascending relationship between shear deformation and equivalent normal stress. This is due to the reason of friction, which appears when relative slippage between the concrete layers increases with the normal stresses at the interface, also it is due to the improvement of bond provided by concrete increases as well.

5.3. Assessment of equations

5.3.1. Ultimate shear stress and its corresponding shear slip

In the last section, based on the theory proposed by Mattock and Hawkins [13], the pairs of simulated values of lateral normal

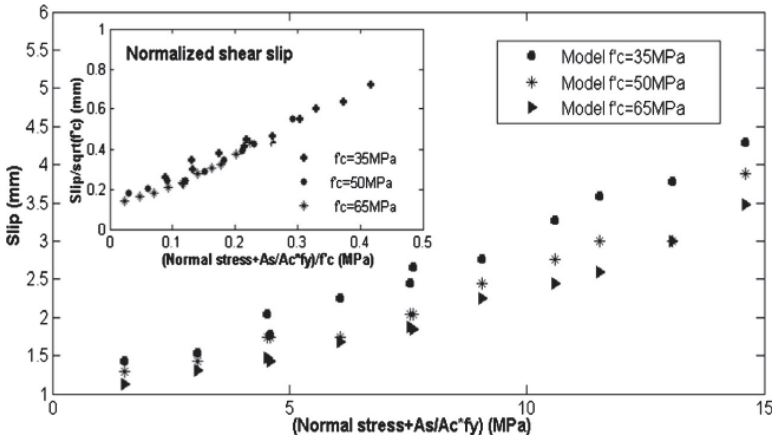

Fig. 12. The ultimate shear stress vs. its corresponding shear slip.

stress ($\sigma + \rho f_y$) and τ_{max}, which corresponds to failure of the concrete obtained by using the Mohr's circles, have been validated with experimental data. Therefore, in the present section, it is desirable to construct empirical equations for describing this non-linear relationship of equivalent lateral normal stress and shear stress. The first step to derive an equation that can express these curves is shown as below:

$$\tau_{max} = -2.65\frac{(\sigma_n + \rho f_y)^2}{f'c} + 1.82(\sigma_n + \rho f_y) + 0.147f'c \quad (8)$$

where $f'c$ is the concrete strength, σ_n is the lateral normal pressure, ρ is the reinforcement ratio and f_y is the steel strength.

However, as shown in Fig. 13 that the simulated data by using Eq. (8) for low reinforcement index (equivalent lateral normal stress under 5 MPa) cannot be properly accounted, especially for the models with higher concrete strength. As known for the triaxial tests under a complete compressive state-of-stress, some Mohr circle analyses show that shear strength to be directly proportional to $f'c$, although the push-off tests also induce some tension but the state of the stress is mostly under compression. Thus the shear strength is dependent on concrete strength [23]. In order to accurately predict the shear stress in all range of reinforcement indexes, basically, the shear strength is normalized by concrete strength for obtaining its characteristics with equivalent normal stresses, and the normalized curve can be shown in Fig. 14. To further validate this normalized curve, another comparison has been carried out with the experimental data recorded by Mattock [15], Anderson [33] and the construction joint test report [23]. As shown in Fig. 14, the normalized equation curves have a good agreement with the data in the construction joint test report [23]. It is slightly higher than the test data reported by Mattock [15] and Anderson [33]. This comparison proves that the normalized curve can predict the shear stress in a reasonable range, and hence, it can be confidently used for further determinations of the ultimate shear stress equation.

By adopting the characteristics of shear stress to the equivalent normal stresses from the above normalized curve and after a multiple regression analyses, the final equation which is improved from Eq. (8) is shown as below:

$$\tau_{max} = (-0.038f'c^{0.21})(\sigma_n + \rho f_y)^2 + 0.33f'c^{0.5}(\sigma_n + \rho f_y) + 0.3f'c^{0.75} \quad (9)$$

where $f'c \leqslant 65$ MPa and $\sigma_n + \rho f_y \leqslant 0.25f'c$.

Considering the recent studies using test specimens made from concrete with compressive strengths within range 70–103 MPa showed that the shear friction theory may not truly represent the behavior of high strength concretes [15], limitations have been set up for the application of the above equation within the range

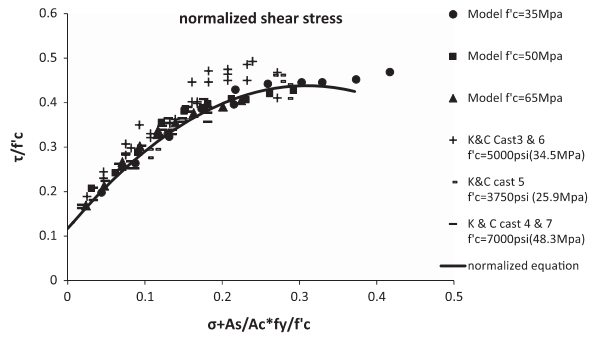

Fig. 14. Comparison of prediction with test data.

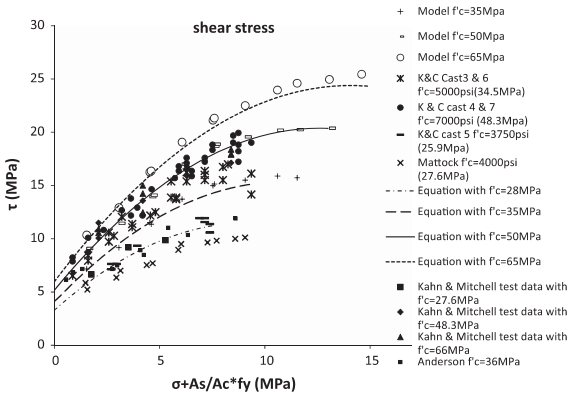

Fig. 15. Assessment final equation for the ultimate shear stress.

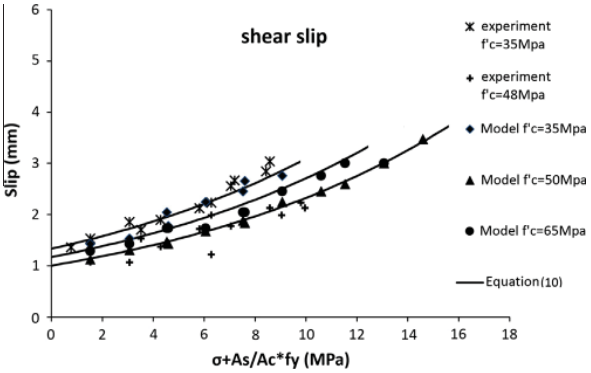

Fig. 16. Prediction of shear slip corresponding to the ultimate shear stress.

with concrete strength up to 65 MPa and the equivalent lateral normal of $\rho f_y + \sigma_n < 0.25f'c$. In order to test the accuracy of the above equation, four different curves with $f'c$ varying from 28 MPa to 65 MPa was plotted using the Eq. (9) and then compared with the data obtained by the previous construction joint test report [12,15,23,33,40] and simulated data. As shown in Fig. 15, the Eq. (9) gives reasonable predictions of the shear tress at high confinement levels as it does in Eq. (8). But unlike the previous Eq. (8), Eq. (9) also provides good predictions of the shear stress at low level of lateral normal stress as well.

Similarly, the regression analysis is also conducted for the shear slip corresponding to the ultimate shear stress and the equation of the shear slip is shown as below:

$$\Delta_1 = (-0.011f'c + 1.72)e^{1E-16f'c + 0.084(\sigma + \rho f_y)} \quad (10)$$

where $f'c \leqslant 65$ MPa and $\sigma_n + \rho f_y \leqslant 0.25f'c$.

A comparison between the results predicted by Eq. (10) and test data is plotted in Fig. 16. There is a good agreement between the results predicted by the empirical and the experimental data.

5.3.2. Direct shear stress to slip relationship

Some previous studies have been conducted on predicting the shear failure at the support of RC members due to a high amplitude blast loading [41,42]. However, due to the inaccuracy prediction of the shear stress to slip characteristics, previous simplified shear models may underestimate the energy absorption capacity of RC members. Therefore, the effort has been invested to extend the prediction of ultimate condition of shear stress and slip of RC

members to further determine the direct shear stress to slip relationship. Based on the simulated shear stress to slip relationships of the 36 models, which considered different reinforcement ratios, lateral normal stresses and compressive strengths as shown in Fig. 9, a regression analysis was carried out to derive the expressions for describing the load-slip characteristics from elastic portion to shear failure followed by a plastic region. Fig. 17 shows the analytical expressions for the approximation to the load-slip curve.

At the beginning, the ultimate shear stress and its corresponding shear slip needs to be calculated using Eqs. (9) and (10) based on the concrete strength, reinforcement parameter and lateral normal stress. Afterward, by applying the results from Eqs. (9) and (10), the prediction of the ascending branch of the curve and the section until reaching the ultimate stress can be done by using Eq. (11) as below:

$$\tau = \tau_{max} \cos\left(\frac{\pi}{2}\frac{\Delta - \Delta_1}{\Delta_1}\right) \quad \text{for } \Delta < \Delta_1 \tag{11}$$

Then Eq. (12) can be used to calculate the shear stress–slip relationship at descending branch (Phase II):

$$\tau = \tau_{max} \cos\left(-\frac{\pi}{2}0.6\frac{\Delta - \Delta_1}{\Delta_1}\right) + 0.01\tau_{max} \sin\left(0.125\pi\frac{\Delta - \Delta_1}{\Delta_1}\right)$$
$$\text{for } \Delta_1,\ \Delta < \Delta_2 \text{ Where } \Delta_2 = 1.8\Delta_1 \tag{12}$$

Finally, the plastic region appears in a slight decrease shear stress in Phase III, and the Eq. (13) below was used to predict the curve:

$$\tau = \tau_2\left(\frac{\Delta}{\Delta_2}\right)^{-0.38} \quad \text{for } \Delta > \Delta_2 \tag{13}$$

$$\text{where } \tau_2 = \tau_{max} \cos\left(-\frac{\pi}{2}0.6\frac{\Delta_2 - \Delta_1}{\Delta_1}\right) + 0.01\tau_{max} \sin\left(0.125\pi\frac{\Delta_2 - \Delta_1}{\Delta_1}\right) \tag{14}$$

5.3.3. Assessment of the shear stress to slip relationship equations

The fitting curve equations have been used to compare with the randomly selected simulation of shear stress to slip relationships and the comparisons are shown in Fig. 18. Overall, a good agreement is found between the simulated results and the curve fitting equations for shear stress and slip at all loading stages. In addition, although most of all the shear stress to slip curve predictions using the equations have a little underestimation for the portion of the decreasing branch when comparing to the data obtained using the LS-DYNA model, the differences are less than 5%, which seems to be reasonable. Thus this curve fitting model represents a good prediction for the shear strength and shear load-slip characteristics of a reinforced concrete member under static load.

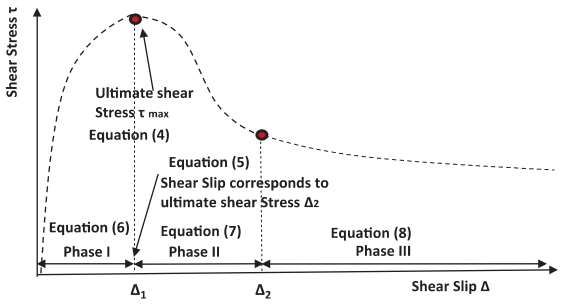

Fig. 17. Shear stress to slip relationship.

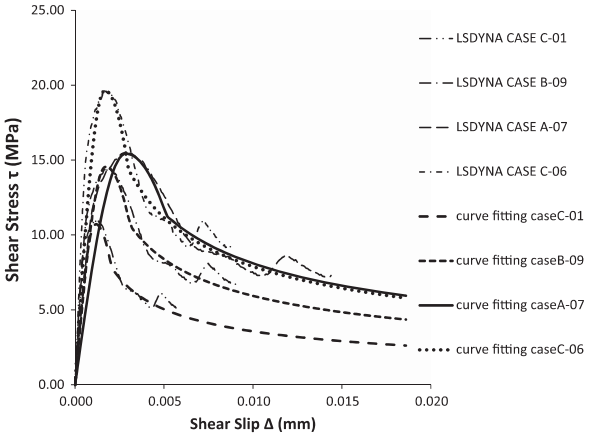

Fig. 18. Assessment of the curve fitting equations.

6. Conclusions

The main purpose of this research is to study the effect of concrete strength, normal pressure and reinforcements of the transfer shear capacity for reinforced concrete members and compare the results of initially un-cracked push-off test specimens under quasi-static loading with the FEM. The important conclusions are summarized as below:

1. The numerical analysis of the push-off test specimens shows that the FEM successfully simulates the response of direct shear stress to slip responses with a reasonable accuracy.
2. The simulated results indicate that the increase of the ultimate shear capacity depends on concrete strength, reinforcement ratio and lateral normal stress. Higher concrete strength directly enhances the ultimate shear strength. The major effects on increasing the shear slip are governed by the reinforcement parameters and lateral normal stresses.
3. Based on the simulated results, equations that can be used to estimate the shear strength and shear stress to slip relationships are derived. A total of 36 sets of simulated data have been collated and analyzed using regression analysis for deriving the equations. Two equations have been derived to predict the ultimate shear strength and its corresponding shear slip.
4. Finally, equations have been evaluated for predicting three different phases of shear stress to slip characteristics through the loading process. A comparison with the collected simulated data shows that these equations provide an accurate prediction and can be used as a preliminary design tool for evaluating the shear transfer in structure design works.

Acknowledgements

The research presented in this paper jointly supported by the Australian Research Council Discovery Grant DP140103025, and the National Natural Science Foundation of China under Grants 51278326 and 51238007 is gratefully acknowledged.

References

[1] Xia J, Mackie KR, Saleem MA, Mirmiran A. Shear failure analysis on ultra-high performance concrete beams reinforced with high strength steel. Eng Struct 2011;33:3597–609.
[2] Moreno-Martinez JY, Meli R. Experimental study on the structural behavior of concrete dapped-end beams. Eng Struct 2014;75:152–63.

[3] Fernandes Canha RM, Kuchma DA, El Debs MK, Alves de Souza R. Numerical analysis of reinforced high strength concrete corbels. Eng Struct 2014;74:130–44.
[4] Bompa DV, Elghazouli AY. Ultimate shear behavior of hybrid reinforced concrete beam-to-steel column assemblages. Eng Struct 2015;101:318–36.
[5] Tan K, Mansur M. Shear transfer in reinforced fiber concrete. J Mater Civil Eng 1990;2(4):202–14.
[6] Hwang S, Yu H, Lee H. Theory of interface shear capacity of reinforced concrete. J Struct Eng 2000;126:700–7.
[7] Su RKL, Li LZ, Lo SH. Shear transfer in bolted side-plated reinforced concrete beams. Eng Struct 2013:1372–83.
[8] Hsu T, Mau S, Chen B. Theory of shear transfer strength of reinforced concrete. Struct J 1987;84(2):149–60.
[9] Hsu T. Softened truss model theory for shear and torsion. ACI Struct J 1988;85:624–35.
[10] Valle M, Buyukozturk O. Behavior of fiber reinforced high-strength concrete under direct shear. ACI Mater J 1993;90:122–33.
[11] Ali M, White R. Enhanced contact model for shear friction of normal and high strength concrete. ACI Struct J 1999;96:348–61.
[12] Hofbeck J, Ibrahim I, Mattock A. Shear transfer in reinforced concrete. ACI J 1969;66(3):119–28.
[13] Mattock A, Hawkins N. Shear transfer in reinforced concrete recent research. J Prestr Concr Inst 1972;17(2):55–75.
[14] Mattock A. Shear transfer in concrete having reinforcement at an angle to the shear plane. ACI Special Publication; 1 no. ACI SP-42; 1974. p. 17–42.
[15] Mattock A. Shear friction and high-strength concrete. ACI Struct J 2001;98:50–9.
[16] Krauthammer T, ASCE M, Bazeos N, Holmquist T. Modified SDOF analysis of RC box-type structures. J Struct Eng 1986;112:726–44.
[17] Murtha R, Holland T. Analysis of WES FY82 Dynamic Shear Test Structures. Technical Memorandum. Naval Civil Engineering Laboratory; 1982.
[18] Julio EN, Branco FA, Silva V. Concrete-to-concrete bond strength Influence of the roughness of the substrate surface. Constr Build Mater 2004;18:675–81.
[19] Santos PM, Júlio EN, Silva V. Correlation between concrete-to-concrete bond strength and the roughness of the substrate surface. Constr Build Mater 2007;21:1688–95.
[20] Saldanhaa R, Júlioa E, Dias-da-Costab D, Santos P. A modified slant shear test designed to enforce adhesive failure. Constr Build Mater 2013;41:673–80.
[21] Barragan B, Gettu R, Agullo L, Zerbino R. Shear failure of steel fiber-reinforced concrete based on push-off tests. ACI Mater J 2006;103:251–7.
[22] Dias-da-Costa D, Alfaiate J, Julio E. FE modeling of the interfacial behaviour of composite concrete members. Constr Build Mater 2011;26(1):233–43.
[23] Karagozian & Case. Construction joint test program. Structural Engineers, Los Angeles, CA; 1973.
[24] Crawford J, Magallanes J, Lan S, Wu Y. User's manual and documentation for release III of the K&C concrete material model in LS-DYNA in TR-11-36-1 Technical Report. Burbank, CA: Karagozian & Case; 2011.
[25] Malvar L, Magallanes J, Wu Y. Numerical analysis of standard laboratory concrete strength tests using explicit lagrangian analytic models. In: 8th International conference on structural dynamics, Leuven, Belgium; 2011.
[26] Malvar L, Crawford J, Wesevich J, Simons D. A plasticity concrete material model for DYNA3D. Int J Impact Eng 1997;19(9–10):847–73.
[27] Crawford J, Wu Y, Choi H, Magallanes J, Lan S. Use and validation of the release III K&C concrete material model in LSDYNA. Glendale, CA: Karagozian & Case; 2012.
[28] Xu K, Lu Y. Numerical simulation study of spallation in reinforced concrete. Comput Struct 2006;84(5):431–8.
[29] Rama A, Murthy C, Palani G, Iyer NR. Impact analysis of concrete structural components. Defence Sci J 2010;60(3):307–19.
[30] Shi Y, Li Z-X. Bond slip modeling and its effect on numerical analysis of blast-induced responses of RC columns. Struct Eng Mech 2009;32(2):251–67.
[31] Ross T. Direct shear failure in reinforced concrete beams under impulsive loading. NM: Air Force Weapons Laboratory; 1983.
[32] Hanson N. Precast-prestressed concrete bridge horizontal shear connections. Development department bulletin D35, PCA; 1960. p. 38–58.
[33] Anderson A. Composite designs in precast and cast in place concrete. Prog Architect 1960;41(9):174.
[34] Mast R. Auxiliary reinforcement in concrete connections. J Struct Div 1968;94 (ST6):1485–504.
[35] Birkeland P, Birkeland H. Connections in precast concrete construction. ACI J Proc 1966;63(3):345–68.
[36] Hofbeck J, Ibrahim I, Mattock A. Shear transfer in reinforced concrete. ACI J Proc 1969;66(2):119–28.
[37] A. C. 318. Building code requirements for structural concrete (ACI 318–99), Commentary (318R–99), Farmington Hills, Mich; 1999.
[38] Haskett M, Oehlers D, Ali M, Sharma S. Evaluating the shear-friction resistance across sliding planes in concrete. Eng Struct 2011;33:1357–64.
[39] Zia P. Torsional strength of prestressed concrete members. ACI J Proc 1961;57 (4):1337–60.
[40] Kahn LF, Mitchell AD. Shear friction tests with high-strength concrete. ACI Struct J 2002;99:98–103.
[41] Astarlioglu S, Krauthammer T, Morency D, Tran TP. Behavior of reinforced concrete columns under combined effects of axial and blast-induced transverse loads. Eng Struct 2013;55:26–34.
[42] Dragos J, Wu C. Interaction between direct shear and flexural responses for blast loaded one-way reinforced concrete slabs using a finite element model. Eng Struct 2014;72:193–202.

Chapter 3
Experimental and Numerical Analysis of High Strength and Ultra High Performance Reinforced Concrete Structure subject to Blast Loading

Introduction

In comparison with conventional concrete and high strength, ultra-high performance fibre reinforced concrete is of high strength, high deformation and high toughness making it as a more ideal material to resist blast loading. Much attention has been paid to explore blast resistance of these newly developed materials in recent years, especially for columns made of UHPFRC because columns are usually the key structural members to prevent the progressive collapse of the whole building from explosions. In this chapter, three papers are adopted for investigating blast resistance of high strength reinforced concrete (HSRC) and ultra-high performance fibre reinforced concrete (UHPFRC) columns by using static testing, real blast testing and finite element simulation approaches. The first and second paper present experimental studies on failure modes of columns made of different types of HSRC and UHPFRC under blast loading. The third paper is to incorporate flexural behaviour of columns from the quasi-static tests into a computation efficient one-dimensional finite element model utilizing Timoshenko Beam Theory to determine the flexural response of steel fibre reinforced concrete columns with and without axial loading subjected to blasts.

There is very limited literature of real blast testing on UHPFRC columns. Two well-instrumented experimental programs were undertaken to contribute to our understanding of the effects of combined blast and axial loading on the behaviours of HSRC and UHPFRC columns under blasts and the data are used for further verification of one dimensional (1D) finite element model developed for the blast analysis of such columns.

The first paper is entitled “Experimental Study on Blast Resistance of Ultra High Performance Twisted Steel Fiber Reinforced Concrete Columns”. The newly developed novel material, that is, ultra-high performance concrete reinforced twisted steel fibres, is used to construct the columns. A total of two HSRC and eight UHPFRC column specimens, were tested under free air blast loadings. All specimens had identical longitudinal reinforcement, but under varying

charge weight and axial loading. The blast test program was successful in providing a substantial amount of high-quality data. The test results showed that comparing with HSRC columns, UHPFRC specimens can effectively resist the overpressures and shock waves from high explosives by reducing the maximum, residual displacements and the spalling and cracking of concrete substantially.

The second paper is entitled "Behaviour of Ultra High Performance Fibre Reinforced Concrete Columns Subjected to Blast Loading". Another newly developed novel material, that is, ultra-high performance concrete reinforced with micro steel fibres is used to manufacture columns. This experimental study is aimed at understanding the dynamic behaviour of HSRC and UHPFRC columns under blast loading to improve the state of the art of protective design.

The third paper is entitled as "Simplified FEM Analysis of Ultra-High Performance Fibre Reinforced Concrete Columns under Blast Loads". This article presents the results of static experimental and numerical work on the response of UHPFRC columns against blast loading. It firstly reports on columns using three-point bending tests to obtain static moment curvature of UHPFRC columns, which are incorporated into a numerically efficient one dimensional finite element model. The one-dimensional finite element model is then validated by field blast testing data and parametric studies are carried out to determine the failure mechanisms of steel fibre reinforced concrete columns under different blast and axial loads.

This chapter adopted the following journal publications:

- Xu J., Wu C., Xiang H., Su Y., Li Z.X., Fang Q., Hao H., Liu Z., Zhang Y. and Li J. (2015). "Behaviour of Ultra High Performance Fibre Reinforced Concrete Columns Subjected to Blast Loading". Submitted to Engineering Structures. (tentatively accepted subject to revision)
- Xu J., Wu C., Su Y., Li Z.X. and Li J. (2015). "Experimental Study on Blast Resistance of Ultra High Performance Twisted Steel Fibre Reinforced Concrete Columns". Submitted to Cement and Concrete Composites.
- Xu J., Wu C., Li J. and Cui J. (2015). "Simplified FEM Analysis of Ultra-High Performance Fibre Reinforced Concrete Columns under Blast Loads". Submitted to Advances in Structural Engineering (invited Special Issue paper).

[THIS PAGE IS INTENTIONALLY LEFT BLANK]

Journal Article 3:
Behaviour of ultra high performance fibre reinforced concrete columns subjected to blast loading

[THIS PAGE IS INTENTIONALLY LEFT BLANK]

Statement of Authorship

Title of Paper	Behaviour of ultra high performance fibre reinforced concrete columns subjected to blast loading
Publication Status	☐ Published ☐ Accepted for Publication ✎ Submitted for Publication ☐ Unpublished and Unsubitted work written in manuscript style
Publication Details	Submitted to Enigneering Structures (tentatively accepted subject to revision)

Principal Author

Name of Principal Author (Candidate)	Juechun Xu		
Contribution to the Paper	Carry out the field test and provide coordination, collection and analysis of field test data and preparation of manuscript.		
Overall percentage (%)	85%		
Certification:	This paper reports on original research I conducted during the period of my Higher Degree by Research candidature and is not subject to any obligations or contractual agreements with a third party that would constrain its inclusion in this thesis. I am the primary author of this paper.		
Signature		Date	21 October 2015

Co-Author Contributions

By signing the Statement of Authorship, each author certifies that:

i. the candidate's stated contribution to the publication is accurate (as detailed above);
ii. permission is granted for the candidate in include the publication in the thesis; and
iii. the sum of all co-author contributions is equal to 100% less the candidate's stated contribution.

Name of Co-Author	Chengqing Wu		
Contribution to the Paper ! !	Supervision and design of the field test and review the manuscript.		
Signature		Date	21 October 2015

Name of Co-Author	Hengbo Xiang		
Contribution to the Paper	Review of manuscript.		
Signature		Date	28 October 2015

!

Name of Co-Author	Yu Su		
Contribution to the Paper	Review of manuscript.		
Signature		Date	22 October 2015

Name of Co-Author	Zhong-Xian Li		
Contribution to the Paper	Review of manuscript.		
Signature		Date	25 October 2015

Name of Co-Author	Qin Fang		
Contribution to the Paper	Review of manuscript.		
Signature		Date	28 October 2015

Name of Co-Author	Hong Hao		
Contribution to the Paper	Review of manuscript.		
Signature		Date	28 October 2015

Name of Co-Author	Zhongxian Liu		
Contribution to the Paper	Review of manuscript.		
Signature		Date	28 October 2015

!

Name of Co-Author	Yadong Zhang		
Contribution to the Paper	Review of manuscript.		
Signature		Date	28 Octber 20158

Name of Co-Author	Jun Li		
Contribution to the Paper	Review of manuscript.		
Signature		Date	22 October 2015

Please cut and paste additional co-author panels here as required.

!

Behaviour of Ultra High Performance Fibre Reinforced Concrete Columns Subjected to Blast Loading

[1]Juechun Xu, [1,2]Chengqing Wu, [3]Hengbo Xiang, [1,2]Yu Su, [2]Zhong-Xian Li, [3]Qin Fang, [4]Hong Hao, [1]Zhongxian Liu, [3]Yadong Zhang, [1,2]Jun Li

[1]TCU-UA (Tianjin Chengjian University-University of Adelaide) Joint Research Centre on Disaster Prevention and Mitigation

[2]School of Civil, Environmental and Mining Engineering, the University of Adelaide, SA, Australia 5005

[3]PLA University of Science and Technology, Nanjing, China

[4]Department of Civil Engineering, Curtin University, WA, Australia

Abstract

Ultra high performance fibre reinforced concrete (UHPFRC) is a cement-based composite material mixing with reactive powder and steel fibres. It is characterized by its high strength, high ductility and high toughness and such characteristics enable its great potential in protective engineering against extreme loads such as impact or explosion. In the present study, a series of field tests were conducted to investigate the behaviour of UHPFRC columns subjected to blast loading. In total four 0.2 m × 0.2 m × 2.5 m UHPFRC columns were tested under different designed explosions but all at a standoff distance of 1.5 m. Blast tests were also performed on four high strength reinforced concrete (HSRC) columns with the same size and reinforcement as UHPFRC columns to evaluate their behaviour under the same loading conditions. The data collected from each specimen included reflected overpressures, column deflections at centre and near the supports. Three major damage modes, including flexural, shear and concrete spalling failure modes, were observed. The post blast crack patterns, permanent deflections and different levels of damage observations showed that UHPFRC columns performed superior in blast loading resistance as compared with HSRC columns.

Keywords: UHPFRC, Nano additives, columns, blasts, experimental analysis

1. Introduction

The analysis and design of civilian and military buildings and structures to withstand shock and blast loading has been a subject of extensive studies in the last decade due to the increase

of terrorist attacks around the world. There are two main approaches to protect structures against man-made explosive hazards. One approach is to reduce damage by protecting the structures with external claddings (e.g., aluminium foam); the other is to strengthen the structures to better withstand explosion-induced loads such as by applying ultra-high performance fibre reinforced concrete (UHPFRC) [1]. Based on standoff distance and charge weight of detonations, blast loads can be categorised into contact, close-in and far field detonation. Contact detonation is a case that explosive is in contact with a structure, therefore, contact blast load is a high-intensity and non-uniform. For close-in detonation, it is a spherical shock wave generated by the explosion striking a structure with a non-uniform and impulse-dominated load. Far field detonation is the explosive located at a large distance from the structure, where a planar wave with a uniform load is applied to the structures. The main aim of the present research is to investigate the capabilities and dynamic response of ultra-high performance fibre reinforced concrete columns against close-in blasts.

UHPFRC members are investigated in the current study because of their outstanding safety, serviceability, durability and ductility [2]. Ultra-high performance concrete is known as a reactive powder concrete that can provide compressive strength up to 200 MPa and flexural tensile strength up to 40 MPa while exhibiting strain-hardening behaviour under uni-axial tension [3] [4]. There are two important considerations in selecting UHPFRC columns to resist blast loading, i.e., their capability of preventing catastrophic failure like progressive collapse and reducing fragmentation due to projectiles [5]. Basically, the most significant characteristics of UHPFRC are its high compressive/tensile strength and outstanding ductility stemming from inclusion of steel fibre, which lead to a dramatic increase of the energy absorption capacity of UHPFRC members and prevent them from suffering catastrophic failure under blast loads. Also, the recent development in Nano-material science has been included to further improve the strength and energy absorption capacity of UHPFRC members so that their sizes can be reduced significantly in comparison with use of conventional concrete counterparts, leading to a remarkable reduction of material used in structural members with a much lower carbon footprint and sustained more active load on members before and after blast events [5]. Furthermore, as mentioned by Brandt [6], steel fibres create a homogeneous matrix in the mix and bridge the gaps of the micro-crack so as to control local crack opening and propagation as well. Thus in addition to increasing integrity of a structure, it is envisaged that application of UHPFRC will contribute to reducing spalling and scabbing.

In recent years there have been considerable numerical and experimental work conducted to understand UHPFRC material under both static and dynamic loading condition [7] [8] [9] [10] [11][12][13]. However, because of the high technical requirements, high costs of manufacturing UHPFRC and the security restrictions required for full scale blast tests, experimental studies on UHPRC members against blasts are very limited. The results of 72 fibrous-reinforced concrete slabs against explosive loading tests were presented by Williamson [16] and it was reported that there is only slight difference in response of high-strength and medium-strength concrete, when used in conjunction with fibres under explosive loading. The experimental data revealed that the failure mode was primarily flexure for a slab in a vertical position with bearing only on two sides, also, the concrete mixed with steel or nylon fibres could be significantly reinforced to withstand the stresses, and effectively reduce the amount and velocity of fragments. Some experimental investigations have been conducted to examine the blast resistant capability of concrete panels/beams/slabs made of UHPFRC materials [4] [17] [18] [19]. Compared with structures made of normal concrete, these tests not only verified that UHPFRC members could perform extremely well, surviving with minor cracks under the applied blast loads, but also proved that UHPFRC structure could minimize the risk of injury or damage caused by concrete debris as they did not break into fragments.

The study [20] on UHPFRC structures subjected to high strain rates has revealed some important differences on behaviours of UHPFRC subjected to relatively low strain rate dynamic loads. In the latter study, for determining the plates subjected to quasi-static loading, three- and four-point bending tests were applied and drop weight tests were performed in order to apply dynamic three-point-bending loading to UHPFRC plates [20]. Wu et al. [21] conducted a series of blast tests on evaluating the effectiveness of slabs using different materials as blast enhancement reinforcement, and some slabs retrofitted with fibre reinforced polymer plates, others constructed with ultra-high performance concrete. It was reported that the reinforced ultra-high performance fibre concrete slabs which suffered least damage was superior to all slabs made of other concrete materials, confirming that ultra-high performance fibre concrete (UHPC) is a more effective material for use in structures susceptible to terrorist attack or accidental impacts. These studies have generally indicated the benefits of UHPC in improving damage tolerance, enhancing control of cracking and spalling, and the ability to minimize the flying debris from damaged slabs and beams. However, most of the information and results provided by the studies have been used for evaluating the application of UHPC on

slabs/beams and there is little published literature pertaining to resistance and behaviour of UHPC columns under blast loading.

Several researchers have studied the blast vulnerability of RC columns with/without FRP-retrofitted composites using blast experiments, numerical prediction and drop-weight tests; and different failure modes have been observed [22] [23] [24] [25]. For analysing columns under blasts, a general classification of different failure modes needs to be established according to orientations of major cracks. Three failure modes are generally characterized. In general, flexural response governs failure mechanism when plastic hinges form in centre and supports of columns. If the static shear-bending capacity ratio is less than unity or under high-velocity impact or blast loading, some columns may collapse in a shear failure mode due to development and widening of severe diagonal cracks and rupture of longitudinal rebars [26] [27] [28]. Furthermore, as the current research is dealing with a close-in blast loading condition, the extremely high intensity and short duration of blasts give rise to localized failure modes such as direct shear failure mode, spalling and scabbing which are under less consideration in the previous literatures.

The objective of this study is to experimentally investigate whether UHPFRC columns can effectively improve their resistance to blast loads at relatively close standoff distance. In total, 8 column specimens, including 4 specimens built with UHPFRC, and 4 specimens built with HSRC were tested under blast loads ranging from 1 kg to 35 kg equivalent TNT at a distance of 1.5 meter. The experiment program including constructing specimens, test set-up and procedure is described. Particular interests of assessing the nature of damage and dynamic response, overpressure, duration time, displacement and failure modes are well-documented and analysed. The concluding remarks are presented in the final section.

2. Outline of Experiment

2.1 Material characteristics

In the current UHPFRC material composition, constant water to binder ratio 0.16 is adopted. Aggregates (river sand) at the same weight dosages (40% by weight) was used, A constant content of silica fume, silica flour was used to provide high pozzolanic effect that accelerated the hydration process and enhanced the material compressive strength. To further improve the performance of matrix, nanoscale $CaCO_3$ particles which acted as an effective filling material and also provided high pozzolanic reactivity had been used. The nanoparticle Nano–$CaCO_3$

has mean particle sizes about 40 nm and the specific surface area (in BET methods) more than 30 m^2/g.

Micro steel fibre (MF) was added into the mixtures and MF has 0.1 mm diameter and 6 mm length which can sustain tensile strength more than 4000 MPa. The steel fibres at a dosage 2.5% by volume were used. This dosage was decided on the basis of a series of preliminary tests. Table 1 shows mix proportions of UHPFRC/HSRC. Please note that HSRC has the same proportions of mix design as UHPFRC except fibre material addition.

Table 1 Composition of UHPFRC/HSRC

Constituent	Cement (kg)	Silica fume (kg)	River Sand (kg)	Glenium (L)	Water (kg)	Water /Binder (%)	Steel fibre (%)	Nano $CaCO_3$ (%)
$1m^3$ mixture	995	229	1051	60	197	16	2.5	3

Static test results based on uniaxial compression and four-points bending tests indicated that the specified UHPFRC compressive strength and flexural tensile strength at 28 days was 148 MPa and 32 MPa, respectively.

2.2 Specimen geometry

The test specimens consist of four UHPFRC columns (that is, U1A, U1B, U2A and U2B) with span length 2.5 m, having square cross section of 0.2 m. The geometry of UHPFRC column, layout of longitudinal reinforcements and spacing of transverse reinforcement are shown in Figure 1. The reinforcing bar has diameter of 16 mm with cross-section area of 201.1 mm^2 and the centre-to-centre spacing of 57 mm. The thickness of the concrete cover is 35 mm; the yield stress and ultimate strength of high strength reinforcing bars are 1450 MPa and 1600 MPa, respectively.

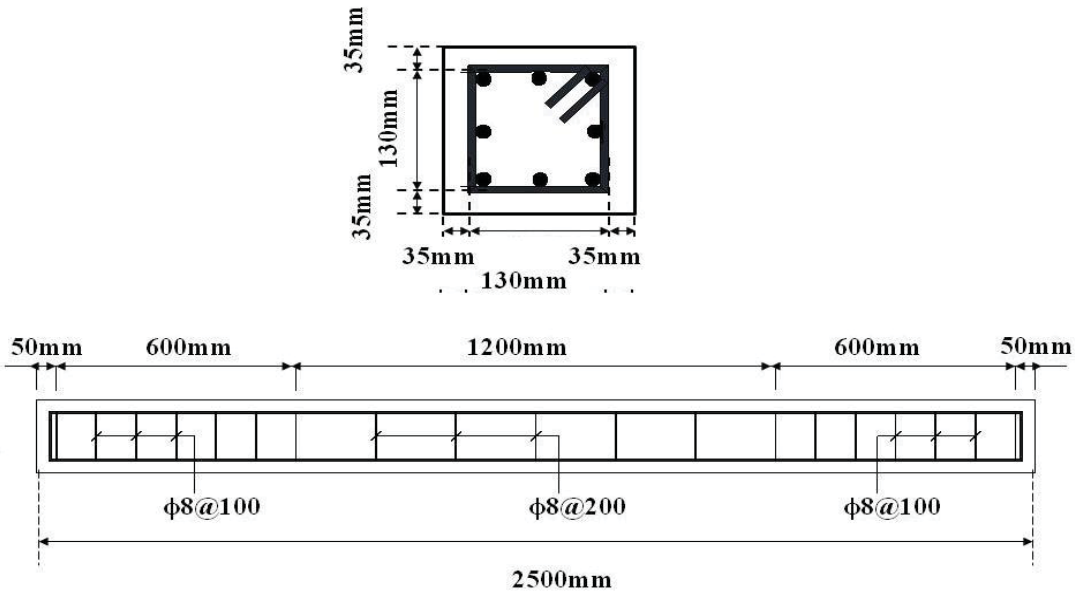

Figure 1 Geometry of the UHPFRC and HSRC specimen

The columns were divided into two groups, with specimens in each group being nominally identical. The columns in Group U were produced by using UHPFRC and Group H by HSRC. The charge weights, scaled distance, specimen geometry for the experimental program are provided in Table 2. It should be noted that U1A was subjected to two shots, that is, 1 kg TNT blast loading followed by 35 kg TNT charge loading (so was U2A), while U1B was subjected to 17.5 kg TNT blast loading. Such arrangement was designed to observe different response modes and possible damages of column. 1 kg blast loading was designed for elastic response; 17.5 kg blast loading was designed for plastic response while 35 kg blast loading was designed for possible failure.

Table 2 Experimental program

Column Name	Description	Fibre Content %	Normal Force (kN)	Charge distance D (m)	Scaled distance ($m/kg^{1/3}$)	TNT equivalent charge weight (kg)
U1A	UHPFRC	2.5	0	1.5	1.5	1
U1A	UHPFRC	2.5	0	1.5	0.5	35
U1B	UHPFRC	2.5	0	1.5	1.5	1
U1B	UHPFRC	2.5	0	1.5	0.6	17.5
U2A	UHPFRC	2.5	1000	1.5	1.5	1
U2A	UHPFRC	2.5	1000	1.5	0.5	35
U2B	UHPFRC	2.5	1000	1.5	1.5	1
U2B	UHPFRC	2.5	1000	1.5	0.6	17.5
H1A	HSRC	0	0	1.5	1.5	1
H1A	HSRC	0	0	1.5	0.6	17.5
H1B	HSRC	0	0	1.5	1.5	1
H1B	HSRC	0	0	1.5	0.8	8
H2A	HSRC	0	1000	1.5	0.6	17.5
H2B	HSRC	0	1000	1.5	0.8	8

2.3 Experimental set-up

A schematic diagram of the test instrumentation is shown in Figure 2. The test set up was commenced by placing the specimen in an excavated test pit with its top surface at the same level as ground. This design is selected to eliminate the clearing effect. When preparing the test field, an excavated test pit with dimensions 5 m x 1.7 m x 2 m was dug for containing the specimen and housing the electrical cables and instrumentation equipment. The installation arrangement of UHPFRC columns is shown in Figure 3.

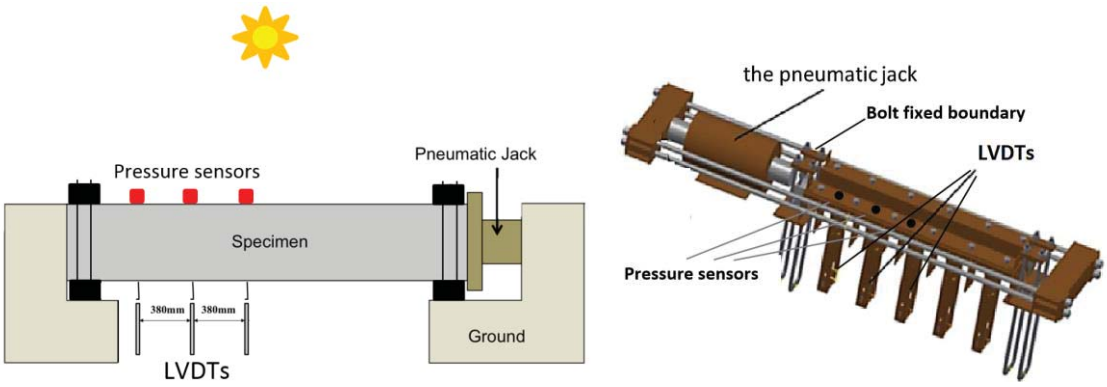

2D View 3D View

Figure 2 Schematic diagram of the support condition

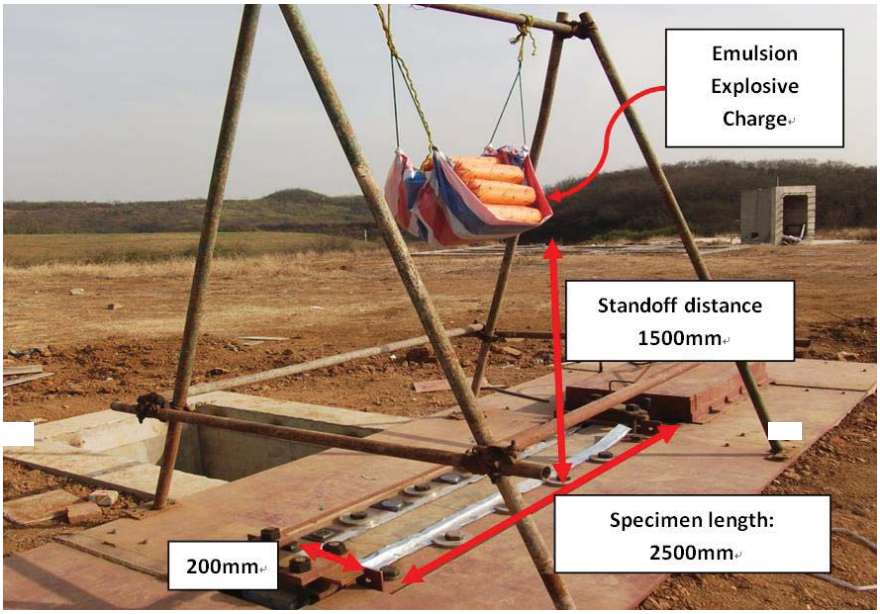

Figure 3 Experimental set up

Steel frame of dimension 2600 mm x 400 mm x 1000 mm as shown in Figure 4(a) was built with a clamping system to ensure that the test specimens were firmly placed inside the frame and prevented the column from uplifting. There were five box-type structures mounted under the frame for placing the displacement measurement devices. With this design, the wiring connection and LVDT devices were fully protected during the blast tests. After placing the column between the supported frames, the whole frame was lowered into the ground, thus there were only top surface of the column with area 200 mm x 2500 mm exposed to the blast wave. In order to prevent the unreliable experimental results due to the vertical movement at the supports, steel yokes were used, which prevent vertical movement against column rebound, thus making the effective span of the specimen 2300 mm. On the other side, the axial loading was applied using a pneumatic jack as shown in Figure 4(b). In the test, axial loading was

applied to some of UHPFRC columns. For typical ground floor column in a low-to-medium rise building, its axial load ratio (service load versus loading capacity) is from 0.2 to 0.4. Considering high mechanical performance of UHPFRC and its comparable density to normal strength concrete, in the current study, an axial load of 1000 kN which equals to approximately 20% their loading capacity was used during the tests and was kept as a constant for all UHPFRC samples. For comparison purpose, HSC columns C8A and C8B were loaded with the same axial load, i.e. 1000 kN which equals to their 50% loading capacity.

Cylinder emulsion explosive charge weights of 1.4 kg to 48 kg were placed at 1.5 m height above the specimen. The nominal TNT equivalence factor for emulsion explosive charge is 1.4.

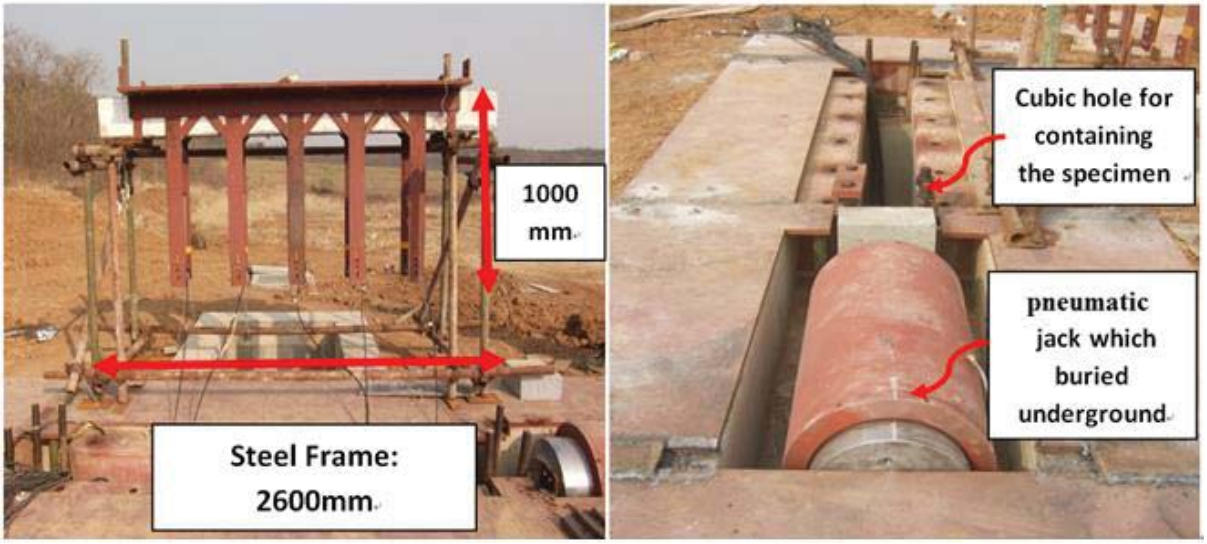

(a) specified steel frame design (b) Pneumatic jack buried underground

Figure 4 Steel frame and axial loading supply system

2.4 Instrumentation

In order to record the column displacement, linear variable differential transducers (LVDT) were placed underneath the column specimens. Figure 5 shows the locations of LVDTs for each test specimen. With a span length of 2500 mm, there is a LVDT placed at 1/2 (mid-span); others were placed at 1/3rd, and 1/6th distance along the span of the column. The LVDTs have sampling rate of 0.2 MHz and a stroke range of 300 mm. As mentioned above, these LVDTs were installed into a box-like steel frame below the specimens and placed in an excavated test pit to avoid blast induced damage. However, prior to the preliminary close-in blast testing, an unsuccessful attempt was observed in which all the LVDTs were destroyed by the extremely high shock pressure passing through the gap between the specimen and the supporting rig. To

better protect the instruments in the following tests, two layers of rubber pad and a thin steel panel were used to cover the gaps between the column and the supporting system. Please note that the additional rubber pads and steel panels did not hinder the free movement of columns.

For measuring the reflected pressures, pressure transducers were installed at the distance of 0 mm, 380 mm and 760 mm away from the centre of the specimen, respectively, as shown in Figure 6. It should be noted that the pressure measurements depend on the sensitivity of the pressure transducers. The measuring range of the pressure sensors was up to 70 MPa. The signals from the LVDTs and pressure sensors were transferred and stored by the data acquisition system (DAC) as digital data. The unit had a maximum recording frequency of 0.2 MHz per channel, and five channels for pressure recording and five channels for displacements recording simultaneously during the tests.

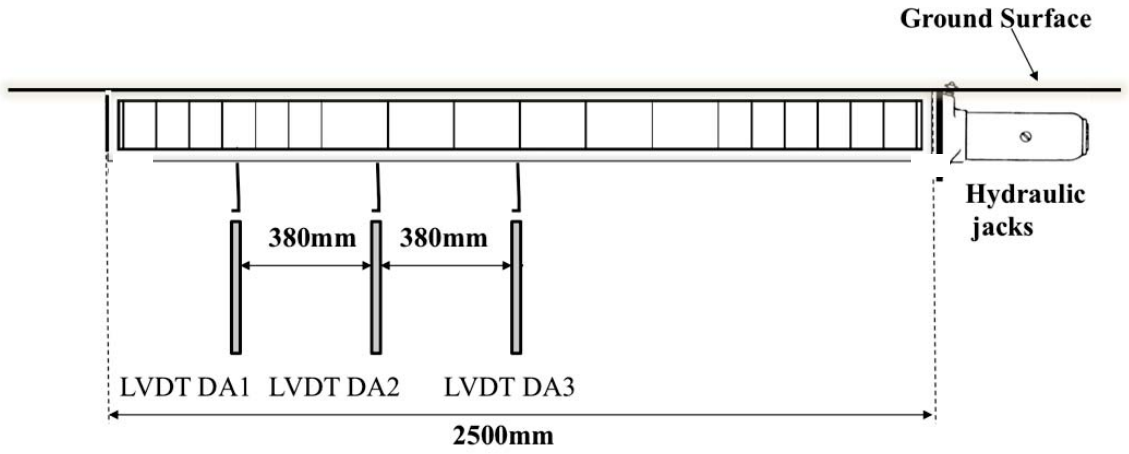

Figure 5 LVDT locations

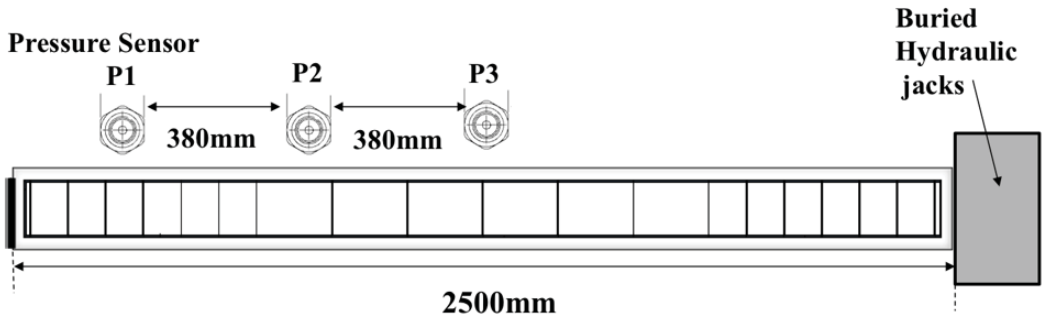

Figure 6 Pressure Sensor locations

2.5 Test procedure

All specimens were tested under combined with/without static axial loading and blast loads; a clear distance between charge centre and centre of specimen is 1.5 m. Each column was tested by the following procedures:

(1) The first step of the experiment was to place the specimen on top of the steel frame, connect all the LVDTs and check connections and functionality.

(2) The whole frame with specimens needed to be placed in a horizontal position and lowered into the testing frame, making sure that the top surface of the column at the same level as the ground surface.

(3) Then make sure the designed steel yokes performed well to let specimen free-standing at two lateral sides of the test position. The other support was connected with the pneumatic jack which located at the same level with the column to make sure that the axial load could be transferred from the pneumatic jack to the column.

(4) Afterwards, the pressure transducers needed to be properly installed and checked.

(5) Explosive was placed using the guided line 1.5 m above the centre of the column.

(6) Finally the detonation was triggered and the test data was recorded.

3. Results and Discussion

The data for UHPFRC columns against blast loading were recorded, including: (1) typical pressure-time histories for different charge weights; (2) displacement versus time histories measured by the LVDTs at mid-span and near supports. All data recorded was used to compare the performance of high strength reinforced concrete (HSRC) specimens with UHPFRC columns, so as to better understand the effect of UHPFRC in improving the blast resistant capability. The summaries of the test results for UHPFRC and HSRC columns are listed in

Table 3. The table reports the maximum mid-span displacement, and residual deflection for each specimen.

Table 3 Summary of UHPFRC and HSRC series test results

Specimen	Charge weight (kg)	Axial load (kN)	Maximum deflection (mm)	Permanent deflection (mm)
U1A	1	0	2.0	0
U1A	35	0	-	21
U1B	1	0	2.0	0
U1B	17.5	0	63	18.5
U2A	1	1000	-	0
U2A	35	1000	68	23
U2B	1	1000	1.2	0
U2B	17.5	1000	29.3	4
H1A	1	0	2.4	0
H1A	17.5	0	82.6	2
H1B	1	0	2.6	0
H1B	8	0	46.9	1
H2A	17.5	1000	56.0	12
H2B	8	1000	38.0	7.5

3.1 Blast pressure measurements

The applied blast loads resulted from four charge weights which are 1 kg, 8 kg, 17.5 kg and 35 kg TNT equivalence at different scale distances were captured by the three pressure sensors located in different places as indicated in Figure 7. Empirical perdition on the peak blast overpressure and duration is based on UFC 3-340-2. According to the comparison between experimental and empirical blast pressure time histories as shown Figure 7, it is generally concluded that empirical method can give reasonable overpressure decay prediction although it underestimates the peak blast overpressure for all the blast scenarios. However, the deviation between the experimental and empirical predictions is relatively small.

As expected, the greater charge weight tends to cause larger reflected pressure. In general, it can be observed that the average peak overpressure recorded has a dramatic increase from 1 kg to 8 kg, to 17.5 kg, and finally 35 kg explosive loading. Furthermore, it is worth noting there is always a second peak over-pressure followed the first peak pressure for most of the data collected from different pressure sensors. This could be ascribed to the complicated process of the detonation of the emulsion explosives. Unlike the incidental explosion engendered by integrated TNT charge, several emulsion explosive charges wrapped for achieving the equivalent TNT blast pressure magnitude were accumulated together, resulting in continuous explosion characteristics. The foregoing reflected blast waves were combined with the subsequent ones, creating different applied loading with several peak pressures. Another possible reason is that a lot of sand and soil particles travel along with it, which inevitably hit on the pressure transducer when the blast wave travels toward a test specimen. As the pressure transducer is highly sensitive, the pressure resulted from the particle collision is therefore also regarded as part of the blast load.

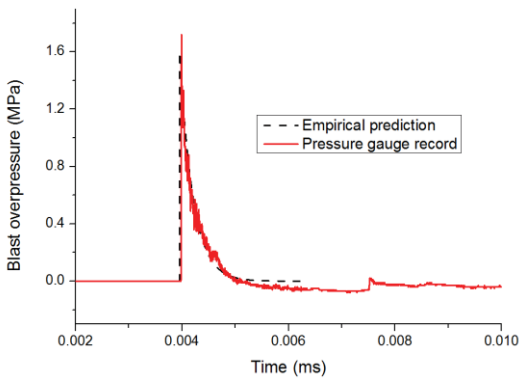

1 kg TNT equivalence

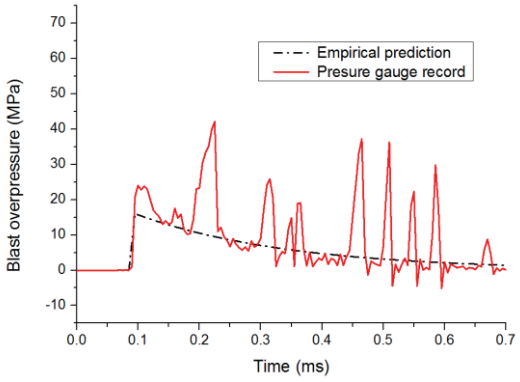

10 kg TNT equivalence

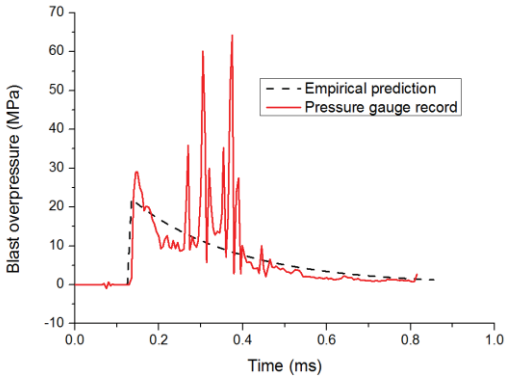

17.5 kg TNT equivalence

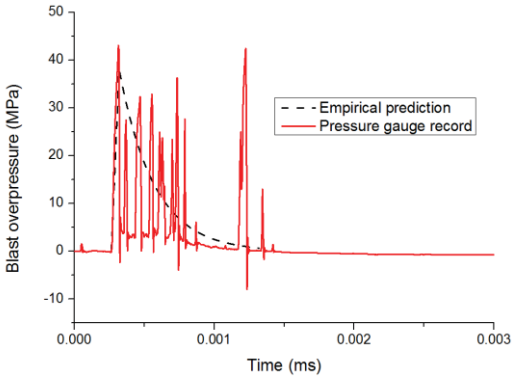

35 kg TNT equivalence

Figure 7: Blast pressure time-histories

3.2 Displacement versus time period of vibration

To assess the effectiveness of UHPFRC columns in enhancing blast resistance, the maximum displacements and permanent deflections measured at the centre of specimens are given in Table 3 and typical displacements for cases U1B and U2B of UHPFRC specimens and H1A, H1B, H2A and H2B of HSRC specimens are used to compare UHPFRC columns with/without axial load and HSRC specimens with/without axial load under similar blast loads plotted in Figures 8-10. These figures have been classified into three groups based on the charge weights varying from 1 kg to 8 kg, and 17.5 kg.

As mentioned before, LVDTs were placed at three different positions for recording the displacements with the legend of DA1, DA2 and DA3 in Figures 8 to 10, DA1-DA3 represented the LVDTs placed at $1/6^{th}$ $1/3^{rd}$ and 1/2 (mid-span) of the distance along the column, respectively. Figures 8(a) and 8(b) indicate the displacements of UHPFRC specimens U1B and U2B under the 1 kg charge weight load recorded by the LVDTs at three different locations. Generally speaking, the responses from each specimen were very similar; the largest displacement was recorded by DA3 at the centre of the specimen, and the value recorded by DA2 was typically less than the mid-span deflection and finally DA1 located near the support followed a very similar trend but the least deflection to that recorded by DA2 and DA3. The results of specimens U1B and U2B under the 17.5 kg charge weight loads as shown in Figures 8 (c) and (d) demonstrate similar phenomena. As expected, larger charge weight (17.5 kg charge weight) yields larger deflection. Figure 9 shows the displacements of HSRC specimens H1B and H2B under the 8 kg charge weight load recorded by the LVDTs at two different locations (DA2 and DA3). Similar phenomenon is observed again.

(a) 1kg

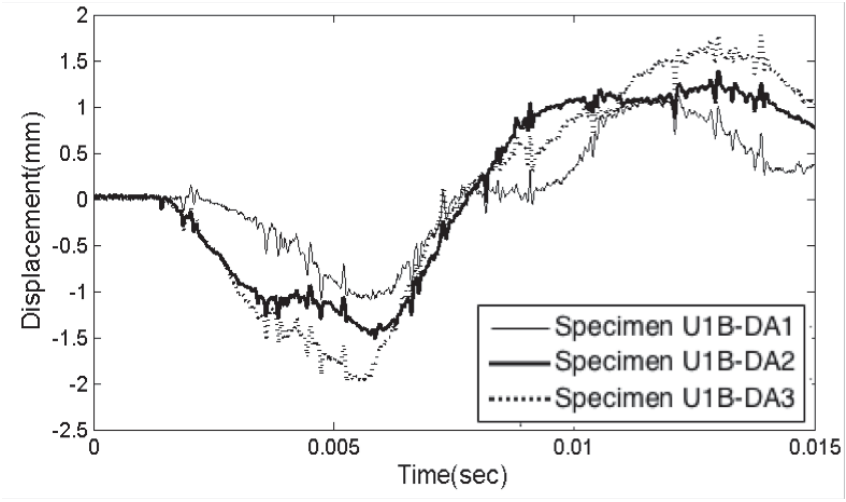

(b) 1kg

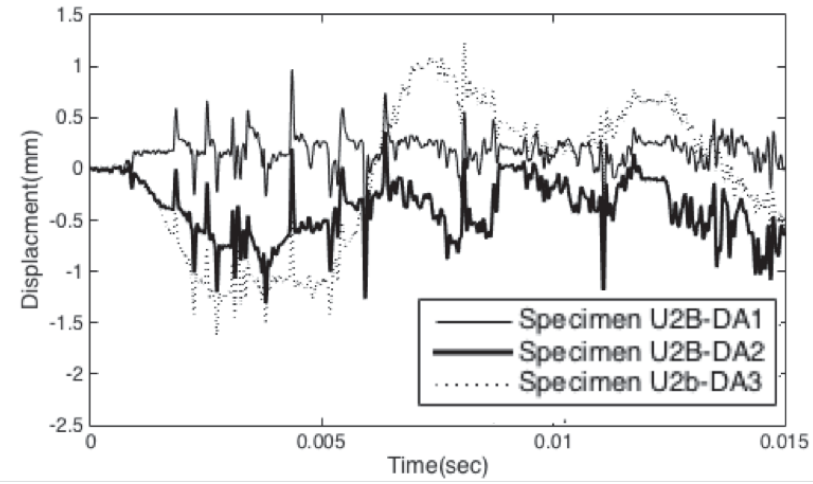

(c) 17.5kg

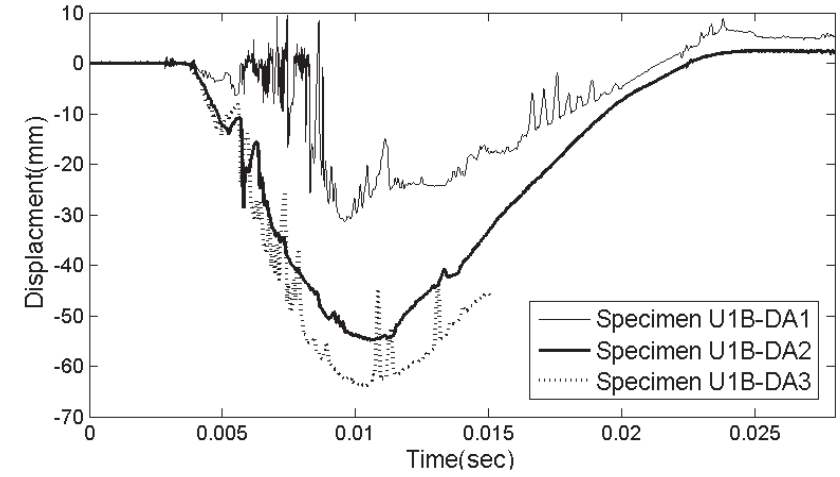

(d) 17.5kg

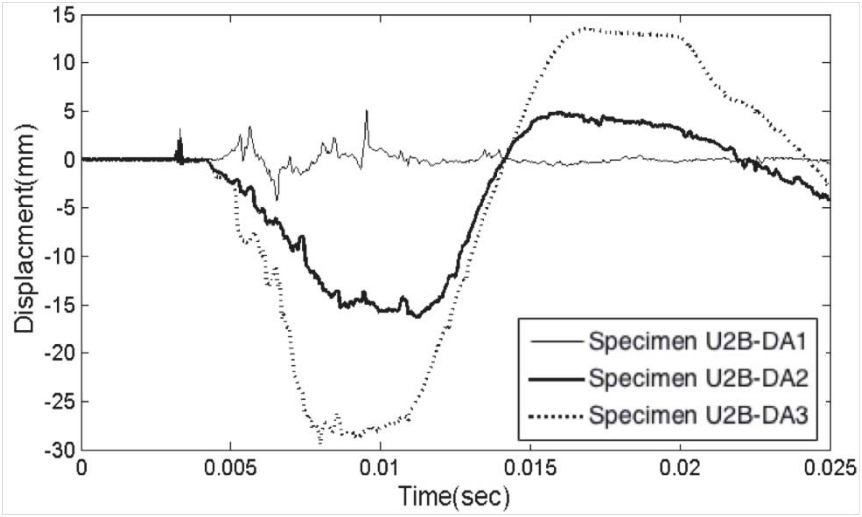

Figure 8 Displacement time profiles of UHPFRC specimens under different charge weight loads

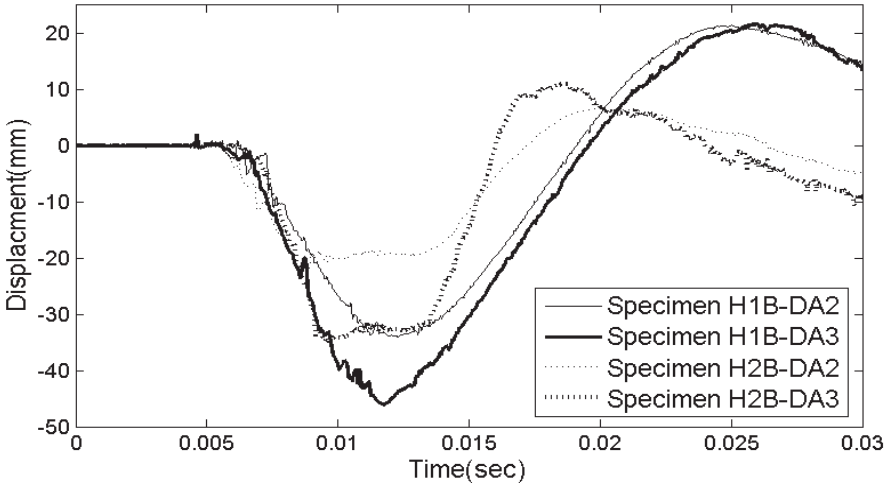

Figure 9 Displacement time profiles of HSRC specimens under the 8kg charge weight loads

The effect of axial load was investigated by applying two different axial loads, namely 0 kN and 1000 kN, on both UHPFRC and HSRC specimens by comparing their displacement-time histories under the same blast loads. As can be shown in Figure 10(a), for comparing the displacements under the same 1 kg TNT equivalent charge loading, the maximum displacement measured at mid-span of UHPFRC column U1B without axial loading was 2.0 mm, while UHPFRC specimen U2B with 1000 kN axial loading was 1.2 mm. This phenomenon shows that the addition of axial load leads to a reduction of 40 % deflection of the UHPFRC specimens. Comparing with the deflection of U1B (64 mm), U2B (29 mm) has approximately 55% reduction of displacement, demonstrating that the axial loading plays significant role on increase of the blast resistance capacity. The similar phenomenon was observed when

comparing HSRC specimens H1A without axial loading (mid-span displacement is 82.6 mm) with H2A with 1000 kN axial load (mid-span displacement is 56.0 mm) as shown in Figure 10 (b). Furthermore, a comparison between HSRC specimens H1B (mid-span displacement is 46.9 mm) and H2B (mid-span displacement is 38.0 mm), in which both specimens were subjected to 8 kg charge weight loading as shown in Figure 9, indicated the significant reduction of displacements that can be attributed to addition of the axial loading. This is because the axial load applied on the column increases the moment capacity and its nominal shear strength of the column. The axial loading also changes the column boundary condition by limiting the end rotation and introducing possible compressive membrane effect, the influence from boundary change outweighs the P-delta effect which results in a reduced mid span deflection. However, it should be notated that as columns experience large deflection and plastic hinges formation occurs at mid-span and fixed ends, axial loads will amplify the displacement and internal moment due to the P–Δ effect.

(a) 1kg

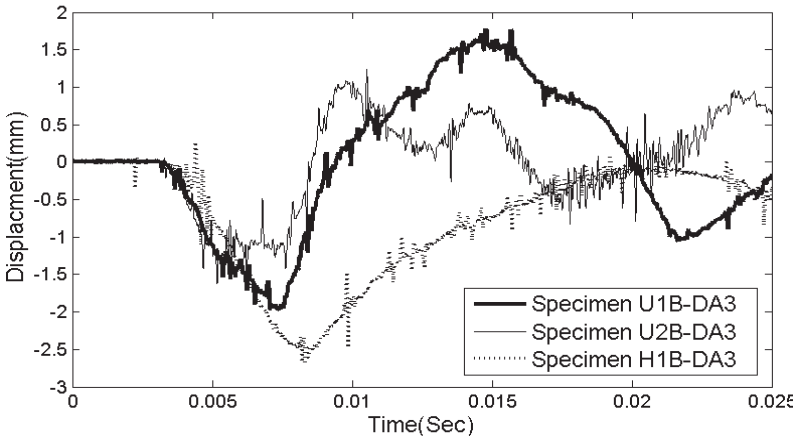

(b) 17.5kg

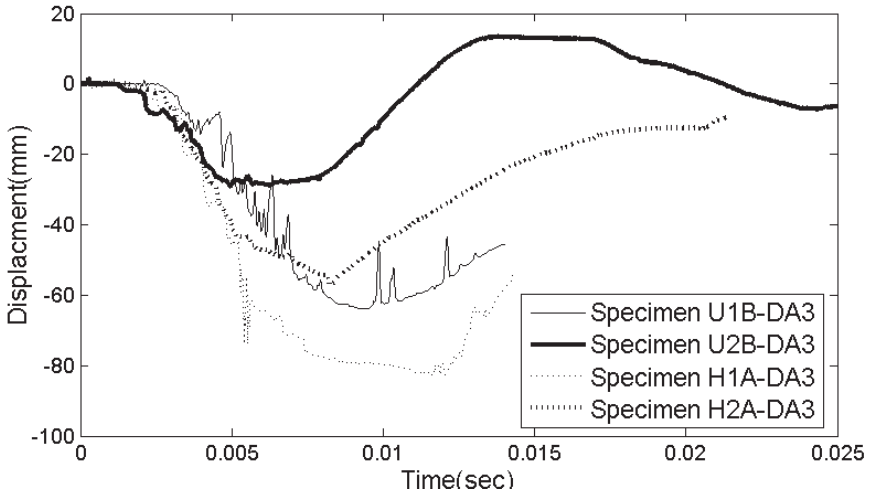

Figure 10 Effects of axial loads on displacement time profiles of specimens

The results in Figure 10 also indicated that the addition of steel fibre in columns (U1B and U2B) substantially reduced the mid-span displacements when compared to a high strength reinforced concrete columns without inclusion of steel fibre (H1A and H2A). With addition of steel fibre, there is a 23% reduction of deflection for U1B (63 mm) when comparing to H1A (82.6 mm) under the same 17.5 kg blast load. Also when comparing U2B with H2A under the same 17.5 kg blast load with 1000 kN axial loading, column U2B has a maximum mid-span deflection which is approximately 47% smaller than HSRC column H2A. Similar reduction of deflection is also observed for U1B (2.0 mm) in comparison with H1A (2.4 mm) under the same 1 kg blast load with 1000 kN axial loading. The above results are expected since UHPFRC has drastically greater compressive and tensile strengths, as well as ductility due to high steel fibre contents [4].

3.3 Crack profiles and failure modes

The effectiveness of steel fibres is also determined by comparing the post-blast crack patterns of UHPFRC specimens to those of HSRC columns. Detailed descriptions of typical crack profile together with classification of the failure modes are presented in this study. Generally speaking, four levels of damage have been characterised to describe the post-blast specimens, which are light, moderate, heavy and severe.

For light damage, column is in good service condition with almost no lateral deflection, only hairline cracks can be observed. When moderate damage occurs, formation of cracks can be found at the distal face and the crack width cannot exceed 5 mm. Following that, heavy damage is defined when concrete crushing at proximal surface is observed together with massive cracking of concrete at distal surface; the crack width is more than 5 mm. The summary of the maximum deflection, level of damage and failure modes is given in Table 4. The post damage photographs of UHPFRC and HSRC specimens under different blast loadings can be observed in Figures 11 and 12, respectively.

Table 4 Post-blast damage analysis

Specimen	Charge weight (kg)	Axial load (kN)	Post-blast failure mode description	Post-blast observed damage level
U1A	35	0	Flexural	moderate
U1B	17.5	0	Flexural	moderate
U2A	35	1000	Flexural	moderate
U2B	17.5	1000	Flexural	moderate
H1A	17.5	0	Brittle shear failure near supports combined with flexural failure and massive concrete spalling	severe
H1B	8	0	Brittle shear failure near supports combined with flexural failure and massive concrete spalling	heavy
H2A	17.5	1000	Brittle shear failure near supports combined with flexural failure and massive concrete spalling	severe
H2B	8	1000	Brittle shear failure near supports combined with flexural failure and massive concrete spalling	severe

Generally, it is seen in Table 4 that UHPFRC columns in an average sense suffered much less damage than HSRC columns. Based on the post blast observed damage scenario, most of UHPFRC specimens are in light or moderate damage level, however, HSRC specimens suffered heavy to severe damage under similar or smaller blast loading. As shown in Figures 11 and 12, the response mode of UHPFRC columns is shown to be primarily flexural while HSRC columns tend to fail under shear with fragments scattered extensively.,

The influence of axial loading on the damage of the specimens was also under investigation. The results on columns tested with axial loading ranging from 0 to 1000 kN showed that axial loading can affect the post damage scenario. When observing the post damage scenario of HSRC columns in Figure 12, columns with axial loading exhibit more severe damage in comparison to the specimens without axial loading. For example, for specimen H1B without axial loading, typical thin cracks with limited spalling of concrete from the surfaces of the column was observed, although the diagonal splitting width of H1B was 2 mm and the crushing

width was 300 mm, the column remains intact. In contrast, there are several diagonal slitting developed from the bottom of the specimen H2B (with 1000 kN axial load) and extend to the top of the column, and also massive crushing of compression concrete was observed; the large diagonal crack with 15 mm width tends to disengage the column into different pieces. This situation may be due to the fact that axial compression strain and flexural compression strain from the blast load exceed the ultimate strains of the columns at the supports. Under the combination force of blast and axial loading, the concrete material is under a complex three dimensional stress state, and increasing of axial loading increases the load applied on the concrete element and thus leading to more severe damage. The addition of axial loading may reduce the capacity of the column to withstand blasts as a result of the pre-compressed concrete being close to material failure.

U1A Specimen with 0 axial load under 35 kg charge weight loading

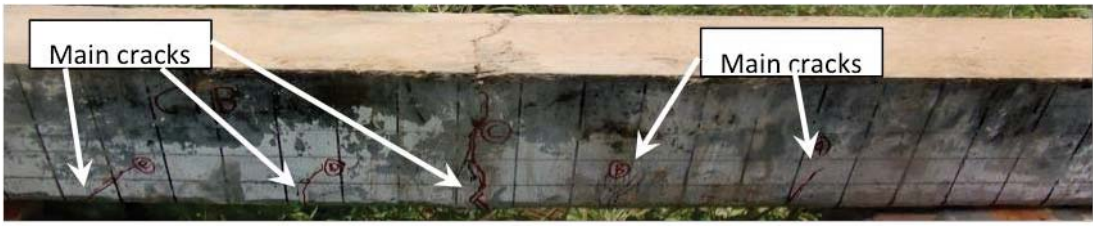

U1B Specimen with 0 axial load under 17.5 kg charge weight loading

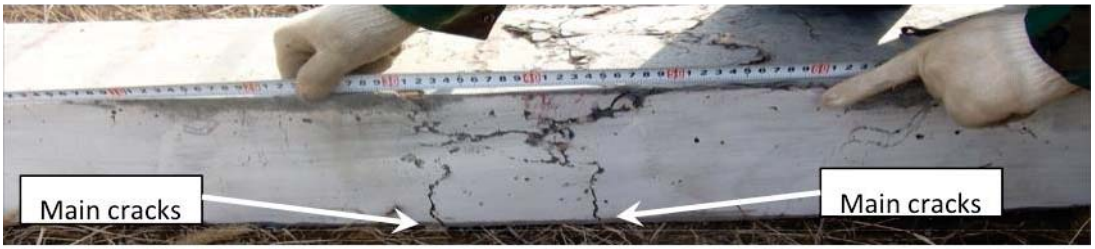

U2A Specimen with 1000 kN axial load under 35 kg charge weight loading

U2B Specimen with 1000 kN axial load under 17.5 kg charge weight loading

Figure 11 Post blast damage situations of UHPFRC columns

H1A Specimen with 0 axial load under 17.5 kg charge weight loading

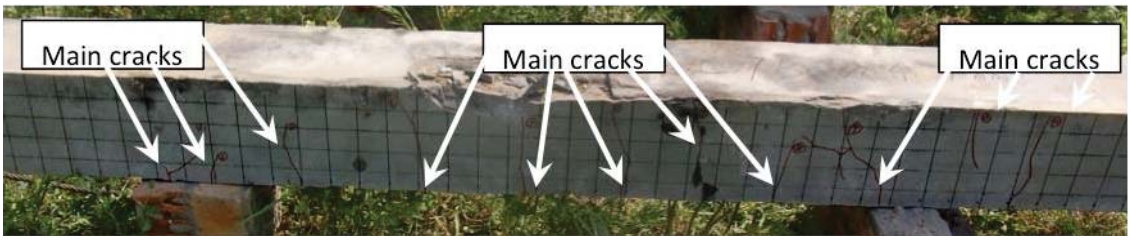

H1B Specimen with 0 axial load under 8 kg charge weight loading

H2A Specimen with 1000 kN axial load under 17.5 kg charge weight loading

H2B Specimen with 1000 kN axial load under 8 kg charge weight loading

Figure 12 Post blast damage situations of HSRC columns

4. Conclusions

The experimental results of 8 columns under explosions at different scaled distances are presented in the current study. Evaluation was based upon the capability of UHPFRC columns to resist blast loading; the values obtained from the tests on HSRC specimens were used as the basis of comparison. Based on the data presented herein, the following conclusions are delivered:

1. Comparing the results of HSRC and UHPFRC specimens shows that UHPFRC specimens can effectively resist the overpressures and shock waves resulted from high explosives, reducing the maximum and residual displacements of columns when subjected to similar blast loads, and enhancing the blast resistant capacity substantially.
2. Investigation into the effect of axial loading on columns subjected to blasts has been performed and the results show that the axially loaded specimens have smaller deflections for UHPRC members. The axial loading changes the column boundary condition and limits the end rotation, and the influence from boundary change outweighs the P delta effect which results in a reduced mid span deflection.

Acknowledgements

The research presented in this paper jointly supported by the National Natural Science Foundation of China under Grants 51278326 and 51238007, and the National Key Technology R&D Program of the Ministry of Science and Technology of China (2012BAJ07B05), and the ARC Discovery Grant DP140103025, is gratefully acknowledged.

References

[1] A. Schenker, I. Anteby, E. Nizri, B. Ostraich, Y. Kivity, O. Sadot, O. Haham, R. Michaelis, E. Gal and G. Ben-Dor, "Foam-protected reinforced concrete structures under impact: experimental and numerical studies," *Journal of Structural Engineering*, vol. 131, no. 8, pp. 1233-1242, 2005.

[2] S. Aydin, H. Yazici and B. Baradan, "High temperature resistance of normal strength and sutoclaved high strength mortars incorporated polypropylene and steel fibers," *Constr Build Mater*, vol. 22, no. 4, pp. 504-512, 2008.

[3] S. Michael and F. Ekkehard, "Ultra-high-performance concrete: research, development and application in Europe," in *In: Proceeding of the 7th international symposium on the utilization of UHS/HPC*, 51-77, 2005.

[4] Y. Na-Hyun, J.-H. J. Kim, T.-S. Han, Y.-G. Cho and J. H. Lee, "Blast-resistant characteristics of ultra-high strength concrete and reactive powder concrete," *Construction and Building Materials*, vol. 28, pp. 694-707, 2012.

[5] A. Ghani Razaqpur, A. Tolba and E. Contestabile, "Blast loading response of reinforced concrete panels reinforced with externally bonded GFRP laminates," *Composites Part B: Engineering* , vol. 38, pp. 535-546, 2007.

[6] A. Brandt, "Fibre reinforced cement-based (FRC) composites after over 40 years of development in building and civil engineering," *Composite Structures*, vol. 86, no. 1, pp. 3-9, 2008.

[7] S.T. Kang, Y. Lee, Y.D. Park, J.K. Kim, "Tensile fracture properties of an ultra high performance fiber reinforced concrete (UHPFRC) with steel fiber," *Composite Structures*, vol. 92, p. 61-71, 2010.

[8] Y. Farnam, S. Mohammadi, M. Shekarchi, "Experimental and numerical investigations of low velocity impact behavior of high-performance fiber-reinforced cement based composite," *International journal of Impact Engineering*, vol. 37, p. 220-229, 2010.

[9] Z. Rong, W. Sun, Y. Zhang, "Dynamic compression behavior of ultra-high performance cement based composite," *International Journal of Impact Engineering*, vol. 37, p. 515-520, 2010.

[10] I. H. Yang, C. Joh and B.-S. Kim (2010). "Structural behavior of ultra high performance concrete beams subjected to bending." *Engineering Structures* 32(11): 3478-3487.

[11] G. H. Mahmud, Z. Yang and A. M. T. Hassan (2013). "Experimental and numerical studies of size effects of Ultra High Performance Steel Fibre Reinforced Concrete (UHPFRC) beams." *Construction and Building Materials* 48: 1027-1034.

[12] S. G. Millard, T. C. K. Molyneaux, S. J. Barnett and X. Gao (2010). "Dynamic enhancement of blast-resistant ultra high performance fibre-reinforced concrete under flexural and shear loading." *International Journal of Impact Engineering* 37(4): 405-413.

[13] P., Máca, R. Sovják and P. Konvalinka (2014). "Mix design of UHPFRC and its response to projectile impact." *International Journal of Impact Engineering* 63: 158-163.

[14] C. Wu, D. J. Oehlers, J. Wahchl, C. Glynn, A. Spencer, M. Merrigan and I. Day, "Blast Testing of RC Slabs Retrofitted with NSM CFRP Plates," *Advances in Structural Engineering*, vol. 10, no. 4, pp. 397-414, 2007.

[15] C. Wu, L. Huang and D. Oehlers, "Blast Testing of Aluminum Foam–Protected Reinforced Concrete Slabs," *Journal of Performance of Constructed Facilities*, vol. 25, no. 5, pp. 464-474, 2010.

[16] G. Williamson, "Response of fibrous-reinforced concrete to explosive loadings, Technical Report," Depart of the army, Ohio River division laboratories, Corps of Engineers, Cincinnati, Ohio, 1966.

[17] T. Ngo, P. Mendis and T. Krauthammer, "Behavior of Ultrahigh-strength prestressed concrete panels subjected to blast loading," *Journal of structural engineering* , vol. 133, no. 11, pp. 1582-1590, 2007.

[18] J. Magnusson, "Fibre Reinforced Concrete Beams Subjected to Air Blast Loading," *In: Structures and materials* , vol. 15, pp. 53-62, 2004.

[19] T. Lok and J. Xiao, "Steel-fibre-reinforced concrete panels exposed to air blast loading," *Proceedings of the Institution of Civil Engineers: Structures and Buildings*, vol. 134, no. 4, pp. 319-331, 1999.

[20] K. Habel and P. Gauvreau, "Response of ultra-high performance fiber reinforced concrete (UHPFRC) to impact and static loading," *Cement & Concrete Composites*, vol. 30, pp. 938- 946, 2008.

[21] C. Wu, D. Oehlers, M. Rebentrost, J. Leach and A. Whittaker, "Blast testing of ultra-high performance fibre and FRP-retrofitted concrete slabs," *Engineering Structures*, vol. 31, pp. 2060-2069, 2009.

[22] P. Imbeau, "Response of reinforced concrete columns subjected to impact load," University of Ottawa, Ottawa, Canada, 2012.

[23] H. Elsanadedy, T. Almusallam, H. Abbas, Y. Al-Salloum and S. Alsayed, "Effect of blast loading on CFRP-Retrofitted RC columns-a numerical study," *Latin American Journal of Solids and Structures*, vol. 8, p. 55 – 81, 2011.

[24] X. Bao and B. Li, "Residual strength of blast damaged reinforced concrete columns," *International Journal of Impact Engineering*, vol. 37, no. 3, pp. 295-308, 2010.

[25] K. Fujikake and P. Aemlaor, "Damage of reinforced concrete columns under demolition blasting," *Engineering Structures*, vol. 55, p. 116–125, 2013.

[26] N. Kishi, H. Mikami and T. Ando, "Impact-resistant behavior of shear-failure-type RC beams under falling-weight impact loading," in *In: Proceedings of the 7th International Conference on Structures under Shock and Impact*, PP.499-508, 2002.

[27] Y. Shi, H. Hao and Z. Li, "Numerical derivation of pressure–impulse diagrams for prediction of RC column damage to blast loads," *Int*. *Journal of Impact Engineering*, vol. 35, no. 11, p. 1213–1227, 2008.

[28] J. Crawford, L. Malwar and K. Morrill, "Reinforced concrete column retrofit methods for seismic and blast protection," In Proc. of society of American military engineering symposium on compressive force protection, Charleston, USA, 2001.

[29] P. Imbeau, "Response of reinforced concrete columns subjected to impact loading," Department of Civil Engineering, University of Ottawa, Ottawa, Canada, 2012.

Journal Article 4:
Experimental study on blast resistance of ultra high performance twisted steel fibre reinforced concrete columns

[THIS PAGE IS INTENTIONALLY LEFT BLANK]

Statement of Authorship

Title of Paper	Experimental study on blast resistance of ultra high performance twisted steel fibre reinforced concrete columns
Publication Status	☐ Published ☐ Accepted for Publication ✎ Submitted for Publication ☐ Unpublished and Unsubitted work written in manuscript style
Publication Details	Submitted to Cemenet and Concrete Composites

Principal Author

Name of Principal Author (Candidate)	Juechun Xu		
Contribution to the Paper	Carry out the field test and provide coordination, collection and analysis of field test data and preparation of manuscript.		
Overall percentage (%)	85%		
Certification:	This paper reports on original research I conducted during the period of my Higher Degree by Research candidature and is not subject to any obligations or contractual agreements with a third party that would constrain its inclusion in this thesis. I am the primary author of this paper.		
Signature		Date	21 October 2015

Co-Author Contributions

By signing the Statement of Authorship, each author certifies that:

i. the candidate's stated contribution to the publication is accurate (as detailed above);

ii. permission is granted for the candidate in include the publication in the thesis; and

iii. the sum of all co-author contributions is equal to 100% less the candidate's stated contribution.

Name of Co-Author	Chengqing Wu		
Contribution to the Paper ! !	Supervision and design of the field test and review the manuscript.		
Signature		Date	21 October 2015

Name of Co-Author	Yu Su		
Contribution to the Paper	Review of manuscript.		
Signature		Date	22 October 2015

!

Name of Co-Author	Zhong-Xian Li		
Contribution to the Paper	Review of manuscript.		
Signature		Date	25 October 2015

Name of Co-Author	Jun Li		
Contribution to the Paper	Review of manuscript.		
Signature		Date	22 October 2015

Please cut and paste additional co-author panels here as required.

!
.

Experimental Study on Blast Resistance of Ultra High Performance Twisted Steel Fibre Reinforced Concrete Columns

[2]Juechun Xu, [*1,2]Chengqing Wu, [1,2]Yu Su, [1]Zhong-Xian Li, [1,2]Jun Li

[1]TCU-UA (Tianjin Chengjian University-University of Adelaide) Joint Research Centre on Disaster Prevention and Mitigation

[2]School of Civil, Environmental and Mining Engineering, the University of Adelaide, SA, Australia 5005

Abstract

Protection of structures against malicious attacks and accidental explosions has become a serious public concern in recent decades. Ultra-high performance fibre reinforced concrete materials, which have outstanding ductility, impact resistance and energy absorption capacity, can be used as an ideal material in blast resistant design of structures. This study is to experimentally investigate both quasi-static and blast resistances of a newly developed ultra-high performance twisted steel fibre reinforced concrete. Static tests were conducted to examine the mechanical behaviour of the newly developed ultra-high performance concrete (UHPC) and concrete columns built with this material were then field tested to investigate their blast resistant capabilities and the results were compared with high strength reinforced concrete (HSRC) columns. The results of different failure modes, reflected blast pressures, and deflection profiles for UHPC and HSRC columns are compared, analysed and discussed. It is found that UHPC columns effectively resisted higher blast loads with minor flexural damage while HSRC columns were severely damaged under lower blast loads. The maximum and residual mid-span deflections of UHPC columns were significantly smaller than HSRC columns under the same blast loading scenarios.

Keywords: Ultra high performance fibre reinforced concrete, columns, twisted steel fibre, blast experimental analysis

1. Introduction:

In the last few decades, with the increase in the number of terrorist attacks, terrorism has generated considerable concern over government agencies and researchers have made significant effort on developing new and affordable ultra-high performance concrete (UHPC) materials resisting blast and impact loads. Compared with conventional concrete, ultra-high performance concrete (UHPC) is known for its high strength, high ductility and high durability, and its fracture energy can be achieved about 20,000-40,000 J/m^2, which is several orders of magnitude higher than that of normal concrete materials [1-2]. Therefore, UHPC is commonly characterized by superior resistance to severe loading conditions such as terrorist bombing attacks and offers high potential for concrete structures with significantly improved structural resistance and durability.

In recent years, to better understand the behaviour of UHPC, a number of studies have been conducted to investigate the mechanical properties of UHPC [3-5] under both static and dynamic loading environments. These studies indicated that UHPC had improved compressive and tensile strength as well as substantially enhanced energy absorption capacity comparing with normal concrete. Habel and Gauvreau [1] presented an experimental and analytical study on rate-dependency of UHPC. They observed a significantly increased strength and fracture energy of the dynamically loaded structural element compared to quasi-static loading. Habel et al. [6] carried out tests on 12 full-size flexural beams made by UHPC composites. They observed that utilizing UHPC material significantly improved the ultimate resistance, stiffness and cracking behaviour of structural member. An analytical model was also developed for predicting the response of members made of UHPC and conventional reinforced concrete. Farnam et al. [7] presented an experimental and numerical study of the low velocity impact test of UHPC members. The results showed that UHPC has higher impact resistance than plain concrete and adding fibre to the concrete can improve the impact resistance. Habel et al. [8] investigated the hydration and their correlation to development of the mechanical properties of UHPC. Astarlioglu and Krauthammer [9] presented a numerical study to compare behaviour of normal strength concrete columns and UHPC columns under blast loads. Yi et al. [10] experimentally evaluated blast resistant capacities of ultra-high strength concrete and reactive powder concrete. Yang et al. [11] investigated the basic behavioural properties of UHPC beams with steel rebar, which provided more information in establishing a model predicting flexural capacity and deflection of UHPC beams under bending conditions.

As discussed by Kim et al.[12] flexural behaviour of UHPC is affected by mechanical properties of fibres, and bonding behaviours between fibre and matrix, and the type and volume contents of fibre are the most important governing factors. To enhance the bonding behaviour, Xu et al. [13] developed spiral steel fibre reinforced concrete, and the impact tests demonstrated such material had better ultimate compressive strength, post-failure strength and energy-absorption capacity among all steel fibre reinforced test specimens. Typical compressive and tensile stress-strain curves obtained from static tests containing three different fibres (Polymeric, hooked and twisted steel fibres in volume fractions ranging between 1.5 and 2.0%) were analysed by Parra-Montesinos [14], and the results indicated that the composite with twisted steel fibres (30 mm long and 0.5 mm diameter) exhibited superior compressive and tensile performance with larger strength, strain, and toughness capacity compared with other fibre materials. This is mainly due to the unique pullout behaviour of the twisted steel fibres which utilized most of the embedded fibre length to generate mechanical resistance, thus higher pullout energy can be produced [15-16]. Therefore, twist or spiral shaped steel fibres in cement paste are promising to produce new composites with high flexural strength and energy absorption capacity.

When considering extreme loading condition such as blast loads, protective structure design normally utilizes retrofitting cladding material like FRP and aluminium foam [17-18]. Although UHPC demonstrated excellent material performance, limited experimental results are available on blast resistant capacities of UHPC structural members. Nevertheless, a few available blast tests demonstrated that UHPC could be a very effective material for blast resistance than normal reinforced concrete (RC) [19-24]. It has become clear from the test results that UHPC members not only have good potential for absorbing energy but also offering increased shatter resistance with reduced scabbing, spall and fragmentation. But the previous experiments focused on UHPC panels under blast loads and only very limited studies were on the blast behaviour of UHPC columns. Since columns are essential load carrying structural components and it may trigger complete progressive collapse of the entire building due to failure of columns, investigation of columns made of UHPC material becomes significant.

Blast loading on structures can produce both local and global structural responses, and local responses cause localized failure such as scabbing and spall; while global responses are associated with flexural failure mode. According to the previous research [25-28], several types

of failure modes have been classified for columns subjected to blast loading. Depending on intensities of blasts, three major failure modes are generally characterized. Basically, as the governing blast loads at large scaled distances impinge the columns laterally, flexural failure will occur after formation of sufficient number of plastic hinges. Secondly, associated with severe short duration and extreme high impulsive load, brittle direct shear failure may occur at supports or diagonal shear failure may occur associated with flexural behaviour of structural elements. Thirdly, for close-in or contact blasts, scabbing may occur in the impact zone and spall may occur on the rear side of columns.

In view of the above discussion, the objectives of this study are to investigate experimentally the mechanical properties of a newly developed UHPC with nano particle addition and blast resistance of columns made of this novel material. Static tests were performed in the laboratory to confirm its outstanding mechanical performance of this novel material compared to normal strength concrete. Full scale explosion tests were also carried out for evaluating the effectiveness of blast resistance of columns made of this novel material.

2. The mechanical properties of the newly developed ultra-high performance concrete

To obtain the material properties of the novel material, static tests were conducted on the ultra-high performance fibre reinforced concrete specimens and the results are discussed in this section.

2.1 Materials Properties

Table 1 shows mix proportions of the novel material investigated in this study. The silica fume was used as reactive material involved in the hydration of cement as commonly used in reactive powder concrete (RPC), and silica flour was used to fill in the voids existing between the cement past and aggregate matrices. To ensure consistency of concrete for all specimens, twisted steel fibre (as shown in Figure 1) which has 1480 MPa tensile strength with diameter of 0.3 mm and length of 30 mm was incorporated in mix design of self-compacting concrete. Fibre materials were employed at a dosage of 2.5% by volume. Nano particles $CaCO_3$ were mixed in the concrete matrix to facilitate hydration effects.

Figure 1 Twisted steel fibres

Table 3 Composition of UHPFRC (unit: kg)

Cement	750
Silica Fume	225
Silica Flour	190
River Sand	1030
Superplasticizer	16
Water	190
Water/Binder	25.30%
Nano Particles Nano-$CaCO_3$	21.7
TF Fibre	191

2.2 Manufacturing Procedure

The aggregate and natural sand used in the concrete were from local source with size between 0.16 mm and 2.5 mm with specific density of 2.58 g/cm^3, respectively. The manufacturing procedure included mixing cement, nano-particles $CaCO_3$, silica fume, and fine sand first in dry condition for about five minutes, and for another three minutes after adding approximate 70% water. Then 30% water pre-mixed with superplasticizer was then added gradually into the mixture. When the state of mortar matrix showed appropriate flowability for good workability and adequate viscosity for uniform fibre distribution, then twisted steel fibres were manually dispersed and added into the mixer in order to avoid fibre clump. The mortar mixture mixed with twisted steel fibres was then placed in a mould. After being cured in humid room at a temperature of 20 ± 5°C for 24 hours, the specimens were demolded and then cured in hot

water at a temperature of 90°C for 48 hours. Specimens were removed from the water tank after 2 days hot water curing and stored in a laboratory at room temperature. When specimens were dried, both surfaces were properly levelled, sanded, polished, cleaned and dried to attain smooth surfaces before testing. All the specimens were tested in a dry condition at age of 28 days.

2.3 Compressive testing

100 mm × 100 mm ×100 mm cubic specimens were used in compressive testing. Figure 2 shows the average compressive strength of three cubic samples at age of 28 days. The testing results were obtained by testing cubes at the Structures Laboratory at TCU-UA (Tianjin Chengjian University-University of Adelaide) Joint Research Centre on Disaster Prevention and Mitigation. 28-day compression tests were conducted on two types of specimens, high strength concrete specimens and specimens with 2.5% by volume content of twisted steel fibres with nano particle addition. All specimens were loaded via the hydraulically controlled constant load rate until failure and the data was recorded using two axial and lateral strain gauges on each specimen, and four axial LVDTs were placed at each corner of the loading plate.

Figure 2(a) shows the average stress strain curves for both types of specimens. High strength concrete (HSC) specimens displayed a very brittle failure after the peak load was reached, on the contrary, UHPC samples had very ductile behaviour as identified in Figure 2(a) by the long descending branch where the specimen continued to carry load up to strains far greater than the peak strain. The steel fibre reinforced concrete specimens were able to sustain significant deformations after the peak stress due to confining effect of steel fibres across cracks. Typical crack patterns for UHPC and high strength concrete specimens after testing are shown in Figures 2(b) & 2(c), respectively. Figure 2(c) shows a very brittle failure of high-strength concrete. In a contrast, due to the bridging mechanism of fibres, UHPC specimens in Figure 2(b) remained in one complete piece and the fibres limited the propagation of the cracks. The average compressive strengths of UHPC and HSC specimens are 130 MPa and 74 MPa, respectively.

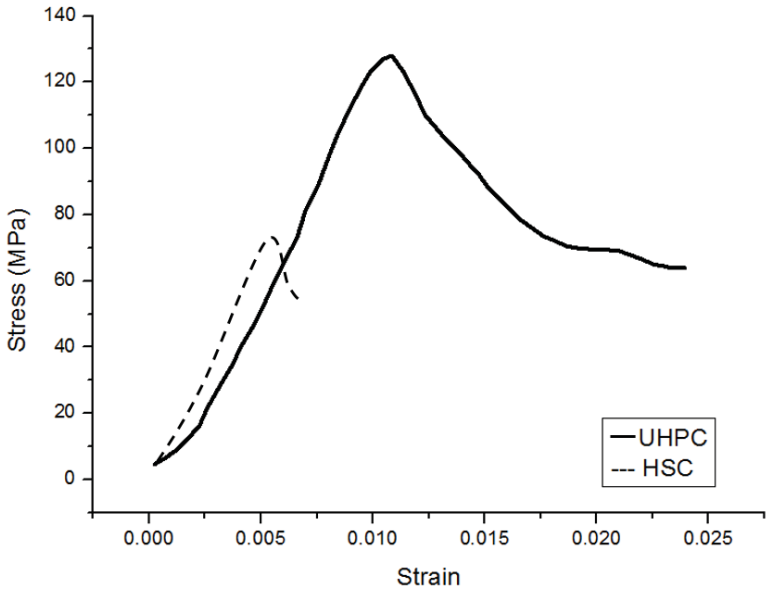

(a) Stress-Strain relationship of UHPC and HSC specimens

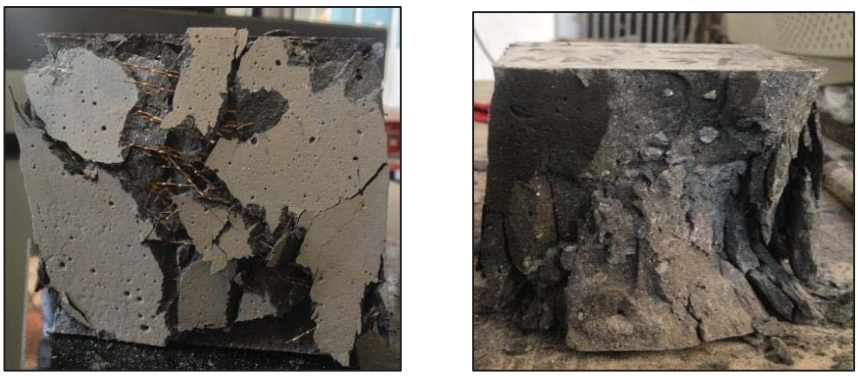

(b) UHPC specimen (c) HSC specimen

Figure 2 Failure modes and data record from compression testing

2.4 Flexural Tensile Tests

Figure 3 provides typical force-displacement curves at mid-span from four-point bending tests on small unreinforced and un-notched beams. The UHPC beam had dimensions of 100 mm × 100 mm × 400 mm. As shown in Figure 3(c) the UHPC specimen reached peak load at 82 kN and a very ductile behaviour after formation of a major crack. In a contrast, the high strength concrete specimens displayed a very brittle failure after the peak load of 51 kN was reached.

Failure modes of high strength concrete and UHPC specimens are also shown in Figure 3. The failure mode of UHPC specimen is significantly different from that of high strength concrete specimen, as shown in Figures 3(a) and 3(b). High strength concrete specimen exhibited typical brittle flexural behaviour, in which the initial crack was formed from the bottom under tensile

loading, and the specimen was then split into two parts when the crack propagated towards top face. However, there was an obvious enhancement of flexural performance in UHPC specimens. The crack width and spacing between the major cracks were reduced for UHPC beams and both parts of specimen remained attached. This is due to the fact that steel fibres have significant influence on bridging two crack faces, and concrete deformability has been increased substantially. After conducting all four-point bending tests, the flexural tensile strength of UHPC samples is averaged as 25 MPa.

(a) Failure of high strength concrete specimens

(b) Failure of UHPC specimens

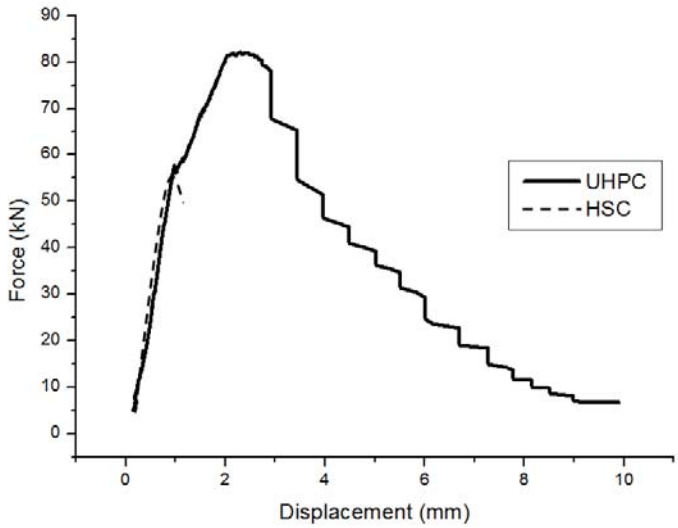

(c) Force-displacement relationship of UHPC and HSC specimens

Figure 3 Failure modes and data record from four point bending testing

3. Blast resistance of ultra-high performance fibre reinforced concrete columns:

3.1 Experimental Program

Blast tests were conducted on columns constructed with the novel UHPC and high strength concrete. Test data including blast overpressure and duration, column deflection time histories well as failure modes are recorded and discussed. Emulsion explosive charge weights ranging from 1.4 kg to 70 kg were placed at 1.5 m height above the specimens. It is common practice to refer explosive weight to TNT equivalence. The nominal TNT equivalent factor for emulsion explosive charge is 0.71. A total of ten columns including eight UHPC columns and two high strength reinforced concrete (HSRC) columns were tested in this experimental program.

3.2 Test Specimen Descriptions

Table 2 summarizes the test program; the columns in Group U were constructed by using UHPC and Group H consists of HSRC columns. Each column had a square cross-section of 200 mm × 200 mm and a total height of 2500 mm. The longitudinal reinforcement consisted of 8-Φ16mm bars (bar yield stress and ultimate strength are 1450 MPa and 1600 MPa) and had 90° hooks extending 75 mm at each extremity to ensure full development of reinforcement into the support region. The transverse reinforcement consisted of roller steel 8 mm diameter ties (f_y = 300 MPa) with 135° hook extensions and the clear concrete cover was kept as a constant of 35 mm. The reinforcement of UHPC columns and HSRC columns is shown in Figure 4.

a)

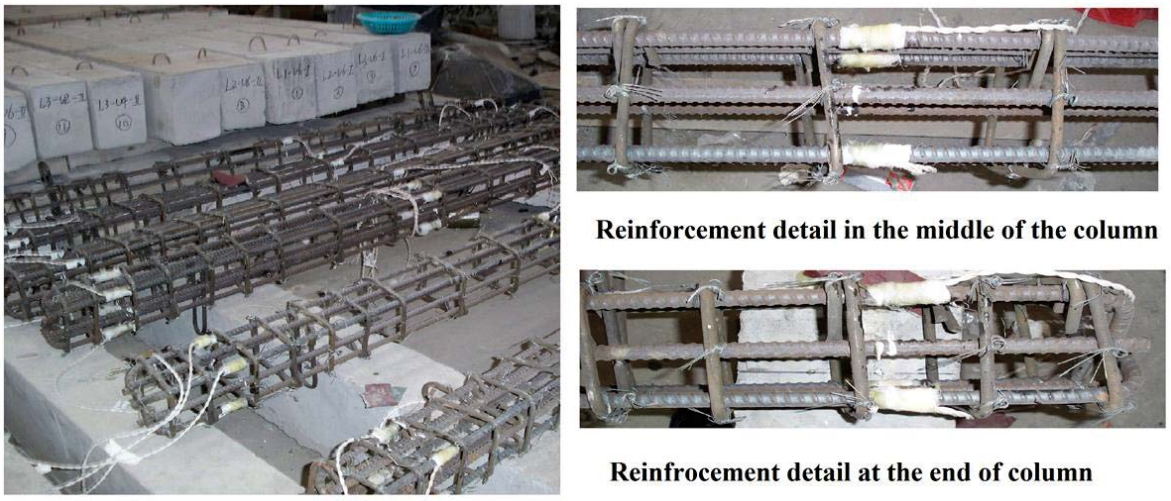

b)

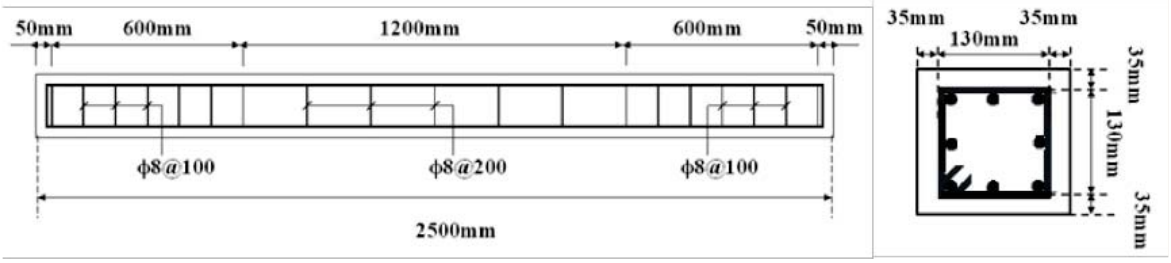

Figure 4 a) Reinforcement, and b) dimension and reinforcement arrangement of UHPC and HSRC columns

3.3 Test setup and instrumentation

A specified 2600 mm × 400 mm × 1000 mm steel frame was built with a clamping system to ensure that a column was firmly placed inside the frame and no uplifting happened. The whole system was then lowered into the ground. Two strips of rubber sheet were used to cover gaps between the column and ground support so as to prevent blast wave passing through the gaps, which might not only destroy the testing instruments beneath the column, but also result in shock waves engulfing the column specimen. Three LVDTs were installed under the column using Dynabolts for deflection measurement, DA3 was located at the centre, DA2 was located at 550 mm away from the centre and DA1 was located at 1100 mm away from the centre of the specimen. Before testing columns, axial load was slowly increased to 1000 kN by using a pneumatic jack, which was installed at one side of the test column. When the designed axial load was reached, the pneumatic jack maintained a constant load to make sure the axial load applied to the column remained constant during the blast test period. The pressure-time history was recorded by blast pressure transducers installed on top surface of the specimens at distance of 0 mm, 380 mm and 760 mm away from centre of the specimen, which were labelled as P3, P2 and P1, respectively. It should be noted that the pressure measurement accuracy depends on the sensitivity of the blast pressure transducers. The voltage signals from LVDTs and pressure sensors were recorded by data acquisition system. The unit had a maximum recording frequency of 0.2 MHz per channel: there were three channels for pressure recording and three channels for displacements recording simultaneously during the blast tests.

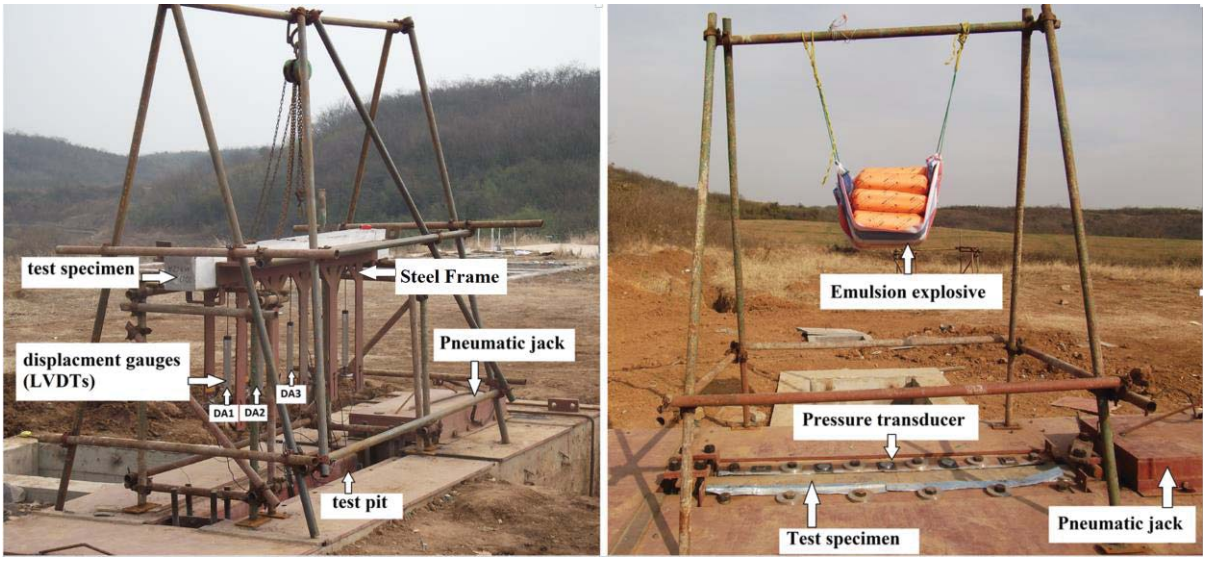

(a) **(b)**

Figure 5: Blast test setup a) before, b) after the specimen being installed into the test pit

3.4 Results and Discussion

The measured blast testing data were processed in order to have a better understanding of the dynamic response of UHPC and HSRC columns to blast loads. The raw data included peak pressure and duration, column deflections. Column deflection results for UHPC and HSRC columns are listed in Table 2.

Table 2 Summary of UHPC and HSRC series test results

Specimen	Charge weight (kg)	Axial load (kN)	Maximum deflection (mm)	Residual displacements (mm)
U3A	1.4	0	1.9	-
U3A	48	0	-	45
U3B	1.4	0	2.4	-
U3B	24	0	-	4
U4B	48	1000	76	24
U5A	1.4	1000	1.2	-
U5A	14	1000	22	0
U5B	24	1000	27.2	0
U5C	35	1000	51.1	0
U6A	70	1000	-	12
U6B	24	1000	-	3
H7A	24	0	82.6	2
H8A	24	1000	56.0	12

3.4.1 Blast pressure measurements

Blast overpressure time history curves were recorded by centre pressure gauge. Empirical prediction on the peak blast overpressure is based on UFC 3-340-2 [27]. Based on the comparison between the experimental and empirical blast pressure time histories as shown in Figure 6, it is generally concluded that empirical method can give reasonable overpressure decay prediction. Although it underestimates the peak values of the blast overpressure for all the blast scenarios, the empirical prediction is still able to provide a good prediction of the trend of the blast overpressure experimental results, especially the trend of the blast overpressure.

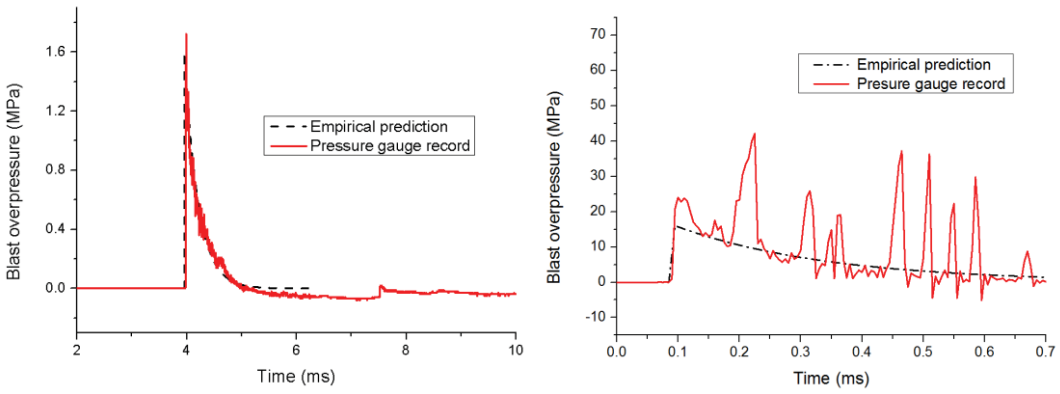

1.4 kg charge 12 kg charge

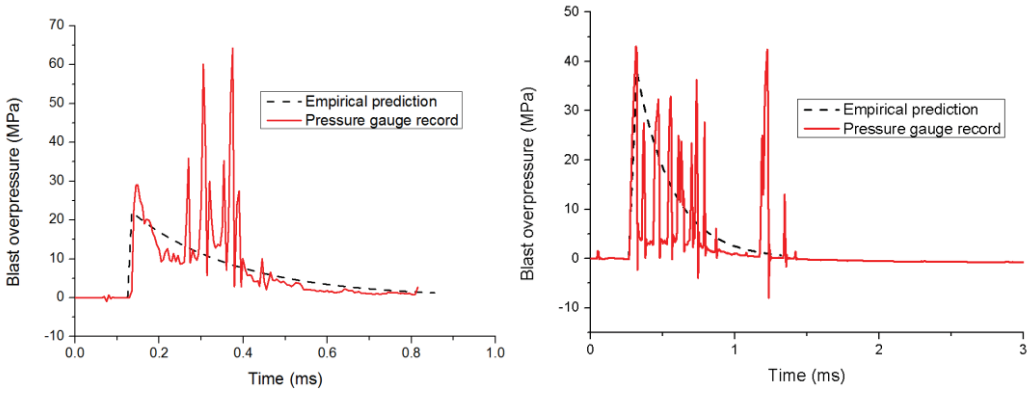

24 kg charge 50 kg charge

Figure 6: Blast pressure time-histories measured by centre pressure gauge

3.4.2 Displacement versus time profile

3.4.2.1 Effect of different magnitudes of blast loadings

The displacement time profiles recorded by LVDTs at different locations were compared. Figure 7 shows typical Deflection vs Time curves for specimens U3B, U4B and U5C under 1.4 kg, 48 and 35 kg blast loadings, respectively. It can be seen that all the displacements recorded from different locations exhibited very similar trend. As distance of LVDTs away from the centre of the specimen increases, the displacement profiles exhibited progressively decreasing. As shown in Figure 7(a), the maximum vertical displacement of U3B measured at mid-span by using LVDT -DA3 is 2.42 mm, while the record reduced to 2.01 mm from DA2 and the least value was recorded by DA1, which is 1.71 mm. For U4B specimen (Figure 7c), the mid-span displacements dropped from 76 mm for DA3 to 59.8 mm for DA2, and to merely 22 mm for DA1.

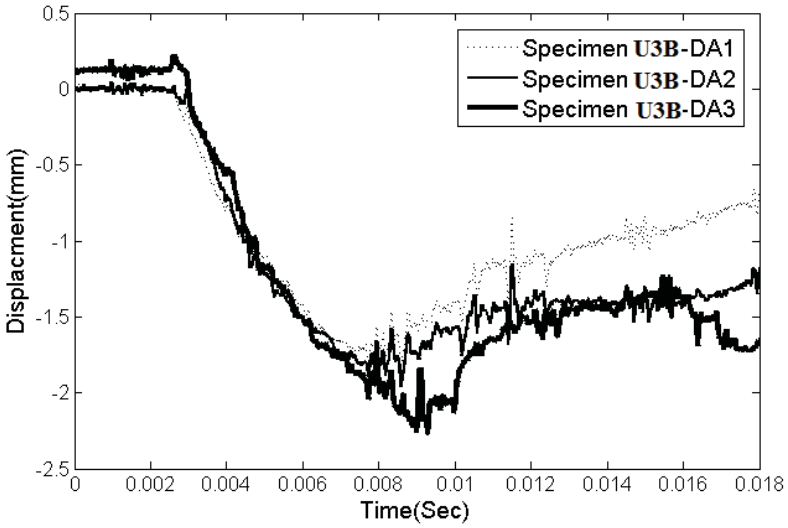

(a) Displacement-time history recorded from three LVDTs on U3B

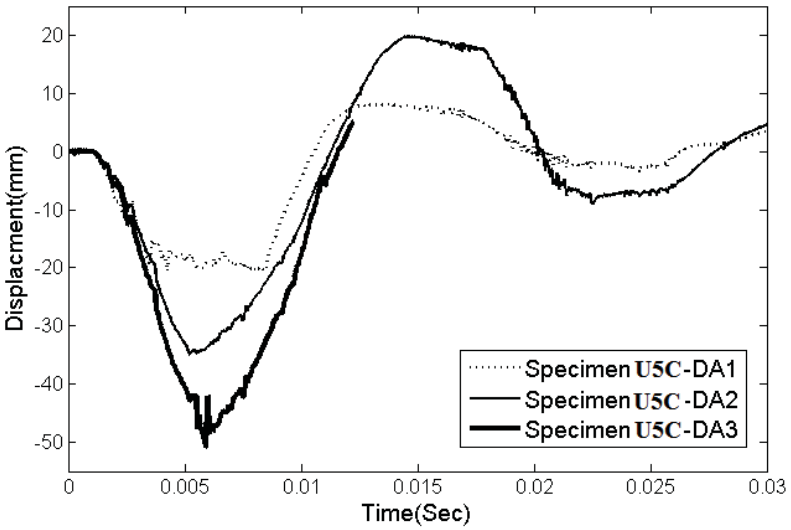

(b) **Displacement-time history recorded from three LVDTs on U5C**

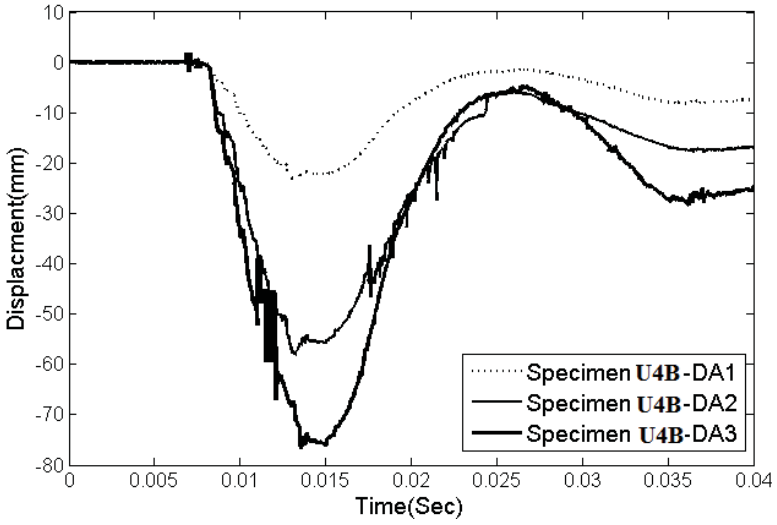

(c) **Displacement-time history recorded from three LVDTs on U4B**

Figure 7 Typical displacement time profiles recorded by three LVDTs located at mid-span (DA3), 550 mm from the mid-span (DA2) and 1100 mm from the mid-span (DA1) of the column

Figures 8 (a) to (c) present the measured deflections of specimens U5A and U5B under the 1.4 kg to 14 kg and finally 24 kg blasts, respectively. U5A column has the maximum mid-span deflection of merely 1.18 mm under 1.4 kg blast loading, while 14 kg blast loading leads to the maximum mid-span deflection of 16.6 mm. Furthermore, the maximum mid-span displacement of U5B under 24 kg blast loading is 27.2 mm.

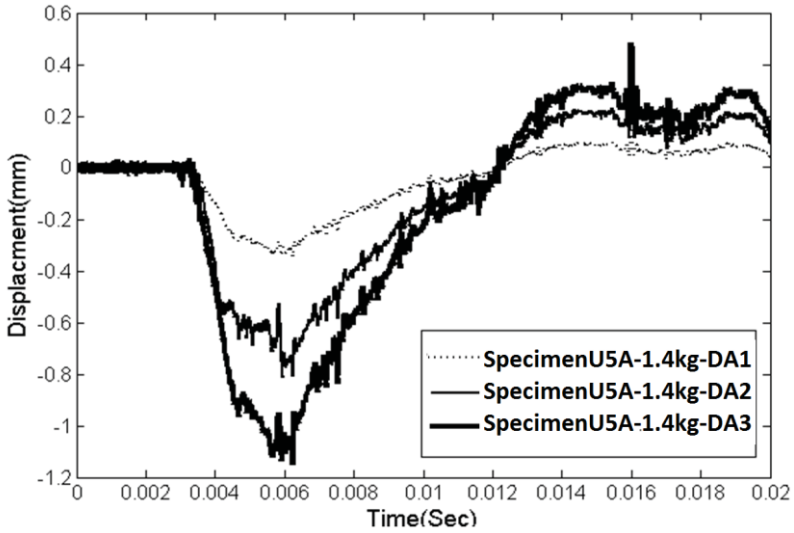

(a) Displacement-time history of specimen U5A under 1.4 kg blast loading

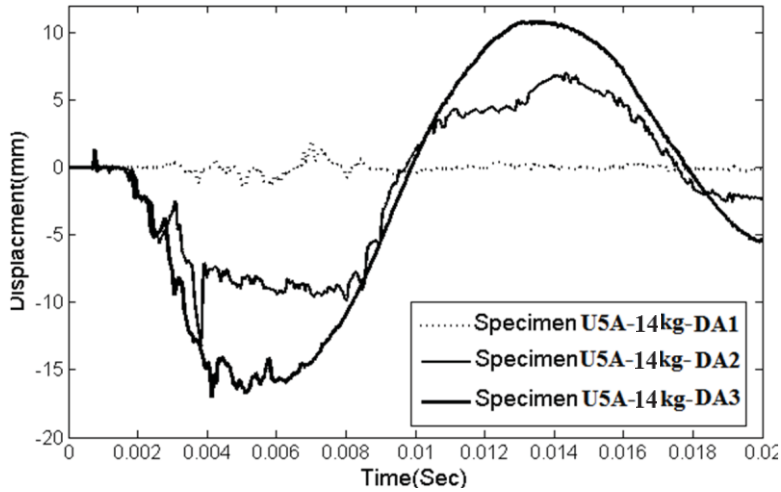

(b) **Displacement-time history of specimen U5A under 14 kg blast loading**

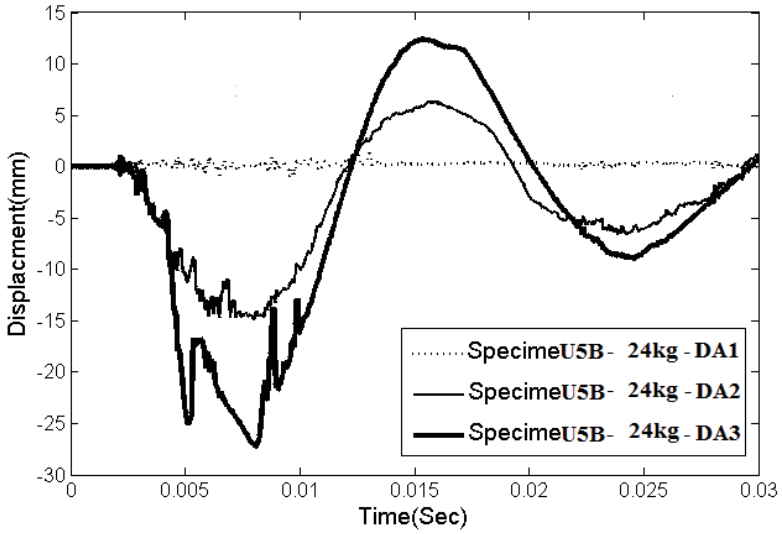

(c) Displacement-time history of specimen U5B under 24 kg blast loading

Figure 8 Displacement time profiles recorded under various blast loadings, measured locations at mid-span (DA3), 550 mm from the mid-span (DA2) and 1100 mm from the mid-span (DA1) of the column

3.4.2.2 Effect of axial loading

Comparisons of mid-span displacement time histories for UHPC columns with and without axial loading are shown in Figure 9. Under the same blast loading, it resulted in a peak deflection of 1.2 mm for U5A specimen with 1000 kN axial loading, and a 1.72 mm deflection for U3A specimen when removing the axial loading. Thus there is 31% reduction in the deflection with adding 1000 kN axial loading. When the blast loading and corresponding column deformation are small, the mid-height displacement of the column with axial loading is slightly smaller. This is due to the fact that with axial load acting on column, it results in an increase in its moment capacity and its nominal shear strength. However, the reduction in mid-height displacement would only occur before the impulse and its corresponding displacement reaches a critical value (i.e. balance condition). Once this critical value is exceeded, the mid-height displacement would increase greatly with the increase of axial load. This is expected for columns with flexural behaviour. When columns experience large deflection and plastic hinges formation occurs at mid-span and fixed ends, axial loads will amplify the lateral deflection and internal moment due to the P–Δ effect. As the deflection increases, the column will transit from a gradual stiffness and strength degradation to a rapid loss of strength due to the buckling of the longitudinal reinforcement.

Another possible reason for the strength enhancement is the membrane effect. In the present study, axial loads application provides lateral restrain to the column, and compressive

membrane action may occur. A small initial deflection may cause a migration of the neutral axis which is accompanied by in-plane expansion of the column at its boundaries. If this expand is restrained, in this case by the axial load application, the development of arching action enhances the strength of the column.

3.4.2.3 Comparison of UHPC and HSRC under blast loadings

Comparing the results of UHPC and HSRC columns under the same 24 kg blast loading as shown in Figure 10, the results clearly demonstrated that the use of twisted steel fibre (U5B) in columns substantially reduced the mid-span displacements when compared to a typical high strength reinforced concrete column (H8A). This is due to the fact that UHPC has drastically greater compressive and tensile strengths, as well as ductility due to high steel fibre contents. The results of H7A and H8A in Figure 10 show that there is a 28% decreasing of deflection on when the axial load was applied to the column specimen H8A. This is similar to the phenomena observed in Section 3.4.2.2, in which the axial loading may improve the capacity of the column to withstand blast loads.

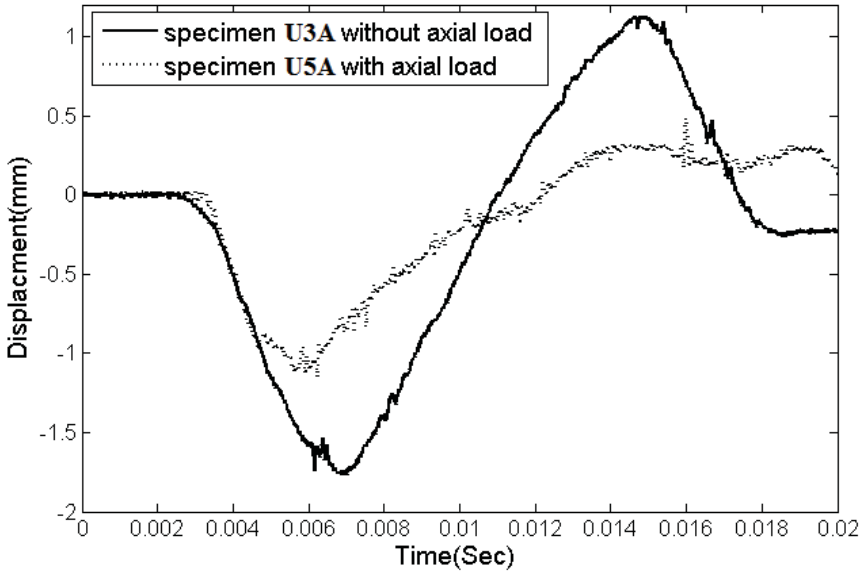

Figure 9 Displacement-time histories at mid-span (DA3) of **UHPC specimen U3A (without axial loading) and U5A (with 1000 kN axial loading) under the same 1.4 kg blast loading**

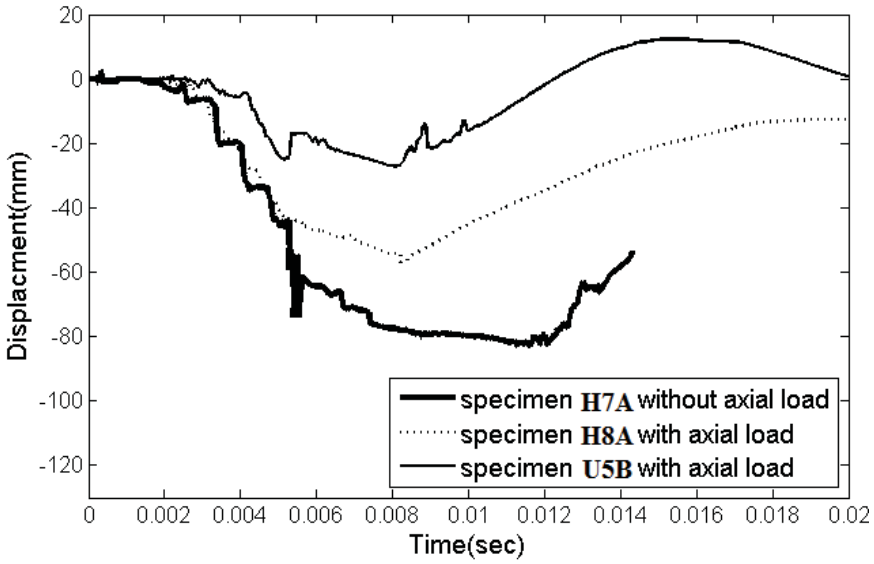

Figure 10 Displacement-time histories at mid-span (DA3) of **H7A (without axial load), H8A (with axial load) and U5B (with axial load) under the same 24 kg blast loading**

3.5 Crack patterns and failure modes

When the blast tests had completed, the specimens were examined. Crack patterns, fragmented locations, and residual displacement were assessed.

3.5.1 UHPC columns under various charge weight loads

Failure modes of four UHPC columns under different blast loadings are shown in Figure 11. Generally, due to the better bonding of twisted steel fibre with concrete matrix, UHPC columns displayed larger elongation, higher residual strength together with higher energy absorption under blasts. Although under very large blast loading, small fragments formed, the pieces were effectively restrained by the steel fibres and very little permanent damage occurred on all UHPC columns. A comparison of UHPC columns against different blasts is divided into two groups. Firstly, under the same 48 kg blast loading, the comparison between U3A and U4B columns is shown in Figure 11 (a) and (b). Although it mentioned in the previous discussion that adding axial loading can effectively reduce the maximum deflection, the column with axial loading (U4B) exhibited more cracks at mid-span in comparison to U3A without axial loading. This situation may be due to the fact that under the combined blast and axial loading, the concrete material is under a complex three dimensional stress state, and addition of axial loading increases the load applied on the concrete element, thus leading to more severe damage. Second comparison is focusing on the post failure performances of UHPC columns under the

35 kg and 70 kg blasts, respectively. Figure 11 (c) shows U5C with a typical flexural failure pattern with small cracks distributed near the specimen centre. For U6A column under the 70 kg blast load, this severe blast loading resulted in fracturing of the concrete on the bottom face as shown in Figure 11 (d). Although some major cracks tended to split the concrete specimen from top to bottom whereas the steel fibers still held the parts of UHPC column together. These observations indicated that UHPC columns could resist severe blast pressures.

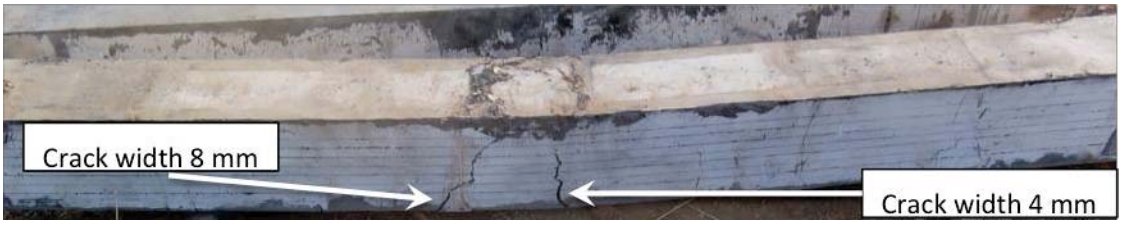

(a) U3A specimen with no axial load under 48 kg blast loading

(b) U4B specimen with 1000 kN axial load under 48 kg blast loading

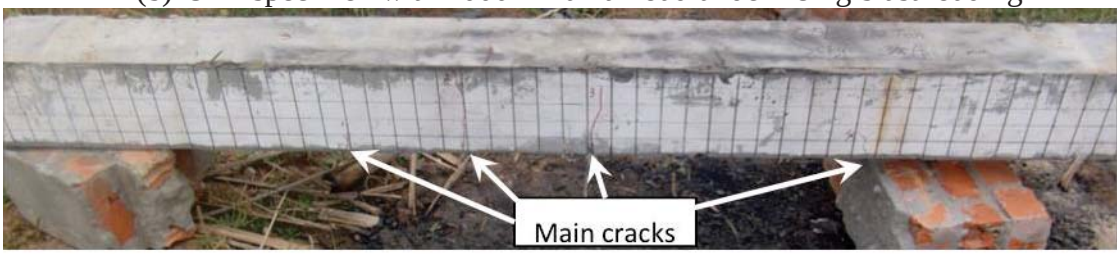

(c) U5C specimen with 1000 kN axial load under 35 kg blast loading

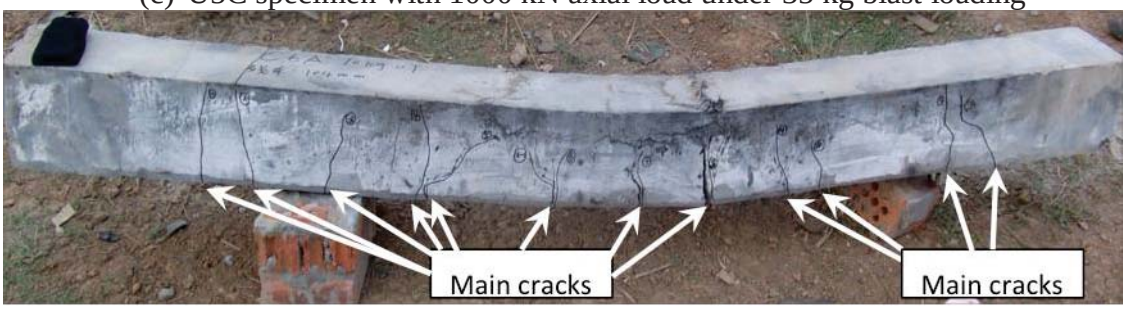

(d) U6A specimen with 1000 kN axial load under 70 kg blast loading

Figure 11 Post blast damage performances of UHPC columns under different blasts

3.5.2 Comparison of post failure patterns between UHPC and HSRC columns

A comparison of post failure patterns for UHPC and HSRC specimens is illustrated in Figure 12. Figures 12a and 12b show the comparison of U3B and H7A under the same 24 kg blast loading. The post failure photo shows that U3B specimen failed with some minor concrete crushing at mid-span. In a contrary, H7A shows considerable breakup at the centre portion of the column; and severe crushing of concrete along the compressive face in the region of mid-span combined with some large diagonal cracks formed in the support regions identified brittle shear failure near supports combined with flexural failure and massive concrete spalling.

Another analysis is conducted between U6B and H8A as shown in Figures 12c and 12d. Each column was exposed to the same 1000 kN axial loading and 24 kg blast loading. As expected for UHPC column, merely light concrete crushing was apparent near the impact zone and minor residual cracks ($\leq$ 0.1 mm) were observable in the tension zone. However, it is seen that H8A column did not fail in a ductile manner as assumed initially. Although there were some flexural cracks, the column finally failed in a brittle mode. It clearly shows crushing of compressive concrete and significant cover spalling for H8A column. This comparison indicated that the use of twisted steel fibre reinforced concrete in columns to resist the blast effects can reduce the concrete crashing substantially.

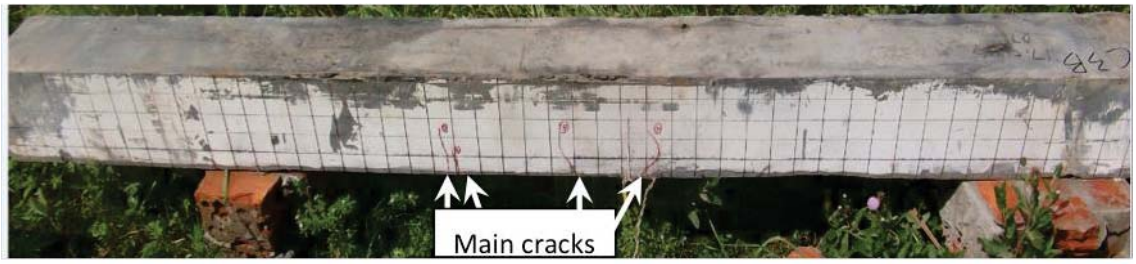

(a) U3B Specimen with no axial load under 24 kg charge weight loading

(b) H7A Specimen with no axial load axial load under 24 kg charge weight loading

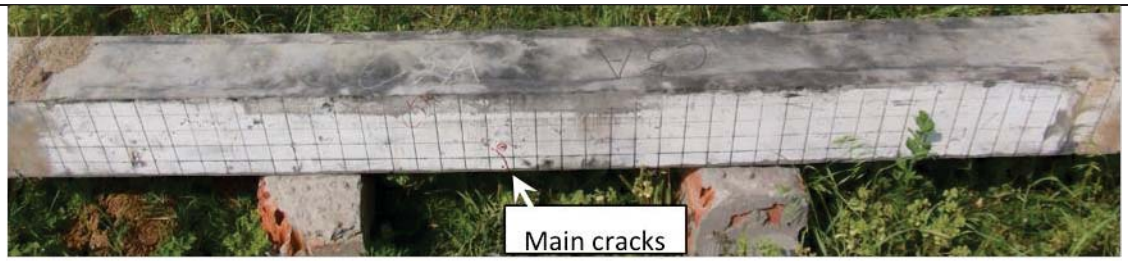

(c) U6B Specimen with 1000 kN axial load under 24 kg charge weight loading

(d) H8A Specimen with 1000 kN axial load under 24 kg charge weight loading

Figure 12 Post blast performances of UHPC and HSRC columns

A description of each column and the testing results are given in Table 3. The major failure mode was primarily dominated by flexure for UHPC columns. However, for the two HSRC specimens, the failure was dominated by shear at the supports with considerable breakup of the centre portion of the column. Compared with HSRC columns, UHPC columns can effectively resist the overpressures and shock waves resulted from high explosive loads, reducing the maximum and residual displacements when subjected to similar blast loads, and enhancing the blast resistant capacity substantially. In general, the blast loads with larger charge weight result in larger damage levels for all specimens under the same condition.

Table 3 Post-blast damage analysis

Specimen	Charge weight (kg)	Axial load (kN)	Post-blast failure mode description	Post-blast observed damage level
U3A	48	0	Flexural	moderate
U3B	24	0	Flexural	moderate
U4B	48	1000	Flexural	moderate
U5C	35	1000	Flexural	severe
U6A	70	0	Primarily flexural failure with diagonal shear cracks	heavy
U5B	24	1000	Flexural	moderate
H7A	24	0	Brittle shear failure near supports combined with flexural failure and massive concrete spalling	severe
H8A	24	1000	Brittle shear failure near supports combined with flexural failure and massive concrete spalling	severe

4. Conclusions

This paper achieves the aims of characterizing the dynamic performance of UHPC and HSRC columns under blast loads. A total of 10 columns were tested to determine their response under explosive loading with explosive weights ranging from 1.4 to 70 kg at standoff distance 1.5 m. Based on the findings of this study, the following conclusions can be made:

- In the four-point bending tests UHPC beam exhibited strain hardening characteristics, however, the load-deflection curve demonstrated a brittle failure for high strength concrete specimen.
- Results from the blast experimental program show that the twisted steel fibres in UHPC enhanced the blast resistance of columns, resulting in reducing the maximum displacements of columns subjected to blast loads.
- In all blast tests, UHPC columns failed by minor bending cracks. However, a larger number of cracks were observed on HSRC columns and shear failure occurred near the supports combined with significant bending and spalling failure occurred under blast loads.
- The results of UHPC columns show that the axial load can reduce the deflection of the column when the blast loading and corresponding column deformation are small. For larger blast loading and column deformation situation, the axial load increases the deflection of the columns under the blast loads.

Acknowledgements

The research presented in this paper jointly supported by The National Basic Research Programme 2015CB058002, the National Natural Science Foundation of China under Grant 51278326, and the ARC Discovery Grant DP140103025, is gratefully acknowledged.

References

[1] K. Habel and P. Gauvreau, "Response of ultra-high performance fiber reinforced concrete (UHPFRC) to impact and static loading," *Cement & Concrete Composites,* vol. 30, pp. 938-946, 2008.

[2] L. Mao, S. Barnett, D. Begg, G. Schleyer and G. Wight, "Numerical simulation of ultra high performance fibre reinforced concrete panel subjected to blast loading," *International Journal of Impact Engineering ,* vol. 64, pp. 91-100, 2014.

[3] V. Bindiganavile, N. Banthia and B. Aarup, "Impact response of ultra-high strength fiber reinforced cement composite," *ACI Materials Journal,* Vols. no.99-M55, pp. 543-548, 2002.

[4] Z. Rong, W. Sun, Y. Zhang, "Dynamic compression behavior of ultra-high performance cement based composite," *International Journal of Impact Engineering*, vol. 37, p. 515-520, 2010.

[5] S.T. Kang, J.K. Kim, "The relation between fiber orientation and tensile behavior in an ultra high performance fiber reinforced cementitious composite (UHPFRCC)," *Cement and Concrete Research*, vol. 41, p. 1001-1014, 2011.

[6] K. Habel, E. Denarie and E. Bruhwiler, "Experimental investigation of composite ultra-high-performance fiber-reinforced concrete and conventional concrete members," *ACI Structural Journal,* Vols. no.104-s11, pp. 93-101, 2007.

[7] Y. Farnam, S. Mohammadi, M. Shekarchi, "Experimental and numerical investigations of low velocity impact behavior of high-performance fiber-reinforced cement based composite," *International Journal of Impact Engineering*, vol. 37, p. 220-229, 2010.

[8] K. Habel, M. Viviani, E. Denarie and E. Bruhwiler, "Development of the mechanical properties of an ultra-high performance fiber reinforced concrete (UHPFRC)," *Cement and Concrete Research,* vol. 36, pp. 1362-1370, 2006.

[9] S. Astarlioglu and T. Krauthammer, "Response of normal-strength and ultra-high performance fiber-reinforced concrete columns to idealized blast loads," *Engineering Structures,* vol. 61, pp. 1-12, 2014.

[10] N.H. Yi, J.H. J. Kim, T.-S. Han, Y.-G. Cho and J. H. Lee, "Blast resistant characteristics of ultra-high strength concrete and reactive powder concrete," *Construction and Building Materials,* vol. 28, pp. 694-707, 2012.

[11] I. H. Yang, C. Joh and B.-S. Kim, "Structural behavior of ultra high performance concrete beams subjected to bending," *Engineering Structures,* vol. 32, no. 11, p. 3478– 3487,

2010.

[12] D. J. Kim, S. H. Park, G. S. Ryu and K. T. Koh, "Comparative flexural behavior of Hybrid Ultra High Performance Fiber Reinforced Concrete with different macro fibers," *Construction and Building Materials,* vol. 25, pp. 4144-4155, 2011.

[13] Z. Xu, H. Hao, H. Li, Experimental study of dynamic compressive properties of fibre reinforced concrete material with different fibres, *Materials & Design*, vol. 33, p. 42-55, 2012.

[14] G. J. Parra-Montesinos, "High-performance fiber-reinforced cement composites: an alternative for seismic design of structures," *ACI Structural Journal,* vol. 102, no. 5, p. 668, 2005.

[15] D. Kim, S. El-Tawil and A. Naaman, "Correlation between single fiber pullout behavior and tensile response of FRC composites with high strength steel fiber, " *in Proceeding of* F*ifth International Symposium on High Performance Fiber Reinforced Cementitious Composites,* Mainz, Germany, 2007.

[16] S. Park, D. Kim, G. Ryu and T. Kyung, "Tensile behavior of Ultra High Performance Hybrid Fiber Reinforced Concrete," *Cement & Concrete Composites,* vol. 34, pp. 172-184, 2012.

[17] C. Wu, L. Huang, D.J. Oehlers, "Blast testing of aluminum foam–Protected reinforced concrete slabs, *Journal of Performance of Constructed Facilities*, 25 (2010) 464-474.

[18] C. Wu, D.J. Oehlers, J. Wachl, C. Glynn, A. Spencer, M. Merrigan, I. Day, Blast testing of RC slabs retrofitted with NSM CFRP plates, *Advances in Structural Engineering*, 10 (2007) 397-414.

[19] T. Ngo, P. Mendis and T. Krauthammer, "Behaviour of ultra high strength prestressed concrete panels subjected to blast loading," *Journal of Structural Engineering,* vol. 133, p. 1582–1590, 2007.

[20] C. Wu, D. Oehlers, M. Rebentrost, J. Leach and A. Whittaker, "Blast testing of ultra-high performance fibre and FRP-retrofitted concrete slabs," *Engineering Structures,* vol. 31, p. 2060–2069, 2009.

[21] S. Millard, T. Molyneaux, S. Barnett and X. Gao, "Dynamic enhancement of blast-resistant ultra high performance fibre-reinforced concrete under flexural and shear loading," *International Journal of Impact Engineering,* vol. 37, pp. 405-413, 2010.

[22] M. Rebentrost and G. Wight, "Investigation of UHPFRC Slabs Under Blast Loads," in *Proceedings, Ultra-High Performance Fiber Reinforced Concrete* , 2009.

[23] J. Li, C. Wu, H. Hao, "An experimental and numerical study of reinforced ultra-high performance concrete slabs under blast loads," *Materials & Design*, 82 (2015) 64-76.

[24] J. Li, C. Wu, H. Hao, "Investigation of ultra-high performance concrete slab and normal strength concrete slab under contact explosion," *Engineering Structures*, 102 (2015) 395-408.

[25] K. Fujikake, T. Senga, N. Ueda, T. Ohno and M. Katagiri, "Study on impact response of reactive powder concrete beam and its analytical model," *Journal of Advanced Concrete Technology,* vol. 4, no. 1, pp. 99-108, 2006.

[26] M. Saatcioglu, A. Lloyd and E. Jacques, "Focused Research for the Development of a CSA standard on Design and Assessment of Buildings Subjected to Blast Loads," Hazard Mitigation and Disaster Management Research Centre Publication, University of Ottawa, 2011.

[27] UFC 3-340.-02. Structures to Resist the Effects of Accidental Explosions, Unified Facilities Criteria Program: U.S. Department of Defence, 2008.

[28] K. Fujikake and P. Aemlaor, "Damage of reinforced concrete columns under demolition blasting," *Engineering Structures*, vol. 55, pp. 116-125.

[THIS PAGE IS INTENTIONALLY LEFT BLANK]

Journal Article 5:
Simplified FEM analysis of ultra-high performance fibre reinforced concrete column under blast loads

[THIS PAGE IS INTENTIONALLY LEFT BLANK]

Statement of Authorship

Title of Paper	Simplified FEM analysis of ultra-high performrance ifbre reinforced concrete columns under blast loads
Publication Status	☐ Published ☐ Accepted for Publication ✎ Submitted for Publication ☐ Unpublished and Unsubitted work written in manuscript style
Publication Details	Submitted to Advances in Structural Engineering

Principal Author

Name of Principal Author (Candidate)	Juechun Xu		
Contribution to the Paper	Carry out numerical simulations, analysis of data and preparation of manuscript.		
Overall percentage (%)	85%		
Certification:	This paper reports on original research I conducted during the period of my Higher Degree by Research candidature and is not subject to any obligations or contractual agreements with a third party that would constrain its inclusion in this thesis. I am the primary author of this paper.		
Signature		Date	21 October 2015

Co-Author Contributions

By signing the Statement of Authorship, each author certifies that:

i. the candidate's stated contribution to the publication is accurate (as detailed above);

ii. permission is granted for the candidate in include the publication in the thesis; and

iii. the sum of all co-author contributions is equal to 100% less the candidate's stated contribution.

Name of Co-Author	Chengqing Wu		
Contribution to the Paper ! !	Guidance of numerical simulation and review of manuscript.		
Signature		Date	21 October 2015

Name of Co-Author	Jun Li		
Contribution to the Paper	Review of manuscript.		
Signature		Date	22 October 2015

!

Name of Co-Author	Jintao Cui		
Contribution to the Paper	Review of manuscript.		
Signature		Date	21 October 2015

Please cut and paste additional co-author panels here as required.

!
'

Simplified FEM Analysis of Ultra-high Performance Fibre Reinforced Concrete Columns under Blast Loads

Juechun Xu[1], Chengqing Wu[1,2*], Jun Li[1], Jintao Cui[2]

[1]School of Civil, Environmental and Mining Engineering, the University of Adelaide, SA, Australia 5005

[2]TCU-UA (Tianjin Chengjian University-University of Adelaide) Joint Research Centre on Disaster Prevention and Mitigation

Abstract

Ultra-high performance fibre reinforced concrete (UHPFRC) is of exceptional mechanical properties including high compressive and tensile strength, and high strain hardening, which has been proved to have significantly high performance in resisting blast loads. In this paper, flexural behaviours of ultra-high performance fibre reinforced concrete (UHPFRC) columns were investigated through full-scale tests. Two 200 mm × 200 mm× 2500 mm columns with and without axial loading were tested under three-point bending tests; and their load–displacement relationships were recorded and moment curvatures were derived. The derived moment curvature relationships of UHPFRC columns were then incorporated into a computational efficient one-dimensional (1D) finite element (FE) model, which utilized Timoshenko beam theory, to determine flexural response of UHPFRC columns under blast loading. After that the 1D FE model was validated with the real blast testing data. The results show good correlation between the advanced FE model and experimental results. The feasibility of utilizing the 1D FE model for simulating both high strength reinforced concrete (HSRC) and UHPFRC columns against blast loading conditions is confirmed.

Keywords: UHPFRC, Static Tests, Finite element method, dynamic response

1. Introduction:

Ultra-high performance fibre reinforced concrete (UHPFRC) has been developing quickly as a modern structural material due to its superior properties in terms of high ductility, compressive and tensile behaviours (Barnett, Lataste, Parry, Millard, & Soutsos, 2010). Until now a number of pilot projects have been carried out to verify its superior material properties and demonstrate its potential for structural applications (Habel K. , Viviani, Denarié, & Brühwiler, 2006),

*[1] Corresponding author. Email: cheng.wu@adelaide.edu.au.

(Habel & Gauvreau, Response of ultra-high performance fiber reinforced concrete (UHPFRC) to impact and static loading, 2008) (Habel, Denarie, & Bruhwiler, Experimental investigation of composite ultra-high-performance fiber-reinforced concrete and conventional concrete members , 2007) (Astarlioglu & Krauthammer, 2014) (Bindiganavile, Banthia, & Aarup, 2002) (Yi, Kim, Han, Cho, & Lee, 2012). Due to the rising threat of terrorism, increasing attention has been attracted to performance and protection of concrete structures against blast loads in recent years, and UHPFRC has its potential to serve this purpose. Its blast resistant behaviours, however, have not been studied in detail. In order to promote applicability of UHPFRC structures against blasts, it is necessary to obtain relevant static and dynamic behaviours of such concrete, i.e. strength, stiffness and deformation capacity. Thus the research discussed herein focuses on both static experimental determination and modelling dynamic behaviour of UHPFRC members.

Comparing with conventional concrete, UHPFRC is a cementitious composites with outstanding material properties (Habel K. , Viviani, Denarié, & Brühwiler, 2006), and it exhibits superior compressive strength exceeding 150 MPa. However, while high strength concrete has a dramatic rise in its compressive strength, its brittleness increases as well. This behaviour will produce unpredictable and undesired brittle failure. In order to overcome this disadvantage, fibres are used to increase tensile strength and ductility of the concrete. Fehling et al. (Fehling, Schmidt, Teichmann, Bunje, Bornemann, & Middendorf, 2004) investigated fibre direction and volume fraction effect on the concrete properties. Their results showed that the descending branch for compression with pronounced differences, and typically 10% to 15% increase could be achieved by increasing fibre percentage. The research effort discussed herein focuses on determining the specific flexural behaviours which further proves that UHPFRC should have good potential for absorbing energy through large deformation under dynamic loading.

Although there have been some research efforts focused on using experimental programs and empirically-based numerical approximations to quantify mechanical properties of UHPFRC, limited research is found to derive its resistance deflection curves of UHPFRC columns due to the perceived complexity of structural behaviours of UHPFRC components as compared to conventional concrete components. Although the recent efforts have been made to find out the mechanical behaviours of UHPFRC, all the static tests are based on small size ultra-high

performance concrete (UHPC) specimens, and a lack of experimental data for quantitative assessment including information on the large size UHPC specimens with steel reinforcement under flexural testing. Current research projects are carried out for determination of flexural load carrying capacity and obtaining load–displacement relationships through consideration of combined effects of adding axial loading on UHPFRC columns.

For carrying out dynamic analysis of structural members against blast loads, there are two common approaches: single degree of freedom (SDOF) method and finite element (FE) method. Although SDOF method is computational efficient and easy to implement, it lacks of accuracy. Comparatively, commercial FE software package typically requires implementation of a three-dimensional meshing with quite a number of degrees of freedom (DOFs), and hence, it requires significant computational effort (Dragos, Visintin, Wu, & Oehlers, A numerically efficient finite element analysis of reinforced concrete members subjected to blasts, 2014). To achieve both accuracy and computational efficiency, Dragos et al. (Dragos, Visintin, Wu, & Oehlers, A numerically efficient finite element analysis of reinforced concrete members subjected to blasts, 2014) proposed a fast running one-dimensional (1D) FE approach to determine response of reinforced concrete members subjected to blast loading and the previous 1D FE method application has been successfully performed on normal reinforced concrete slabs [21] [22]. The present research effort is intended to extend applicability of the previous research into the realm of the new advanced UHPFRC columns.

In summary, the main objective of the current research is to analyse and achieve a high accuracy and computational efficient simulation for predicting response of UHPFRC columns under explosion. The first step is to experimentally obtain reliable load displacement relationships of UHPFRC columns. The load displacement relationships of both HSRC and UHPFRC columns are then incorporated into a computational efficient 1D FE model utilizing Timoshenko beam theory for further dynamic analysis. Finally, the real experimental testing data of HSRC and UHPFRC columns under blast loading are used to validate the 1D FE model for undertaking the dynamic analysis.

2. Static experimental program for testing flexural behaviour of UHPFRC columns

The experimental program is designed to derive moment curvature relationships of UHPFRC and HSRC columns, and hence, it allows investigation of their flexural behaviours with and without axial loading.

2.1 Test Specimens

The mix design of UHPFRC differs significantly from that of HSRC. UHPFRC mix compositions are characterized by high grade cement, superplasticizer, and silica fume content (Kang, Lee, Park, & Kim, 2010). The mix proportions of the UHPFRC investigated in this test program are described as follow. For aggregates, natural sand from local source was used and the aggregate size was between 0.16 mm and 2.5 mm and specific gravity of 2.58 g/cm^3. Silica fume was used as reactive material to involve in the hydration of cement as commonly used in reactive powder concrete (RPC), and silica flour was used to fill in the voids existing between the cement paste/aggregate matrix. To ensure consistency of concrete for all the specimens, steel fibres with diameter 0.12 mm and length 6 mm were incorporated in mix design of self-compacting concrete employed at a dosage from 2.5% by volume. The material properties of UHPFRC are listed in Table 1. The base mixture of HSRC was the same as UHPFRC except the addition of silica fume and steel fibre material.

Table 1- Composition of UHPFRC

Constituent	Cement (kg)	Silica fume (kg)	River Sand (kg)	Glenium (l)	Water (kg)	Water /Binder (%)	Steel fibre (%)	Nano $CaCO_3$ (%)
1m^3 mixture	995	229	1051	60	197	16	2.5	3

Both HSRC and UHPFRC columns had a square cross-section of 200 mm × 200 mm with a height of 2500 mm. The longitudinal reinforcement consisted of 8screw thread Φ16 mm bars (bar yield stress and ultimate strength are 1350 MPa and 1600 MPa) and had 90° hooks extending 75 mm at each extremity to ensure full development of the reinforcement into the support region. The transverse reinforcement consisted of roller steel 12 mm diameter ties (f_y = 1600 MPa) with 135° hook extensions and the clear concrete cover was kept as a constant of 35 mm. The dimension of UHPFRC and HSRC columns is shown in Figure 1.

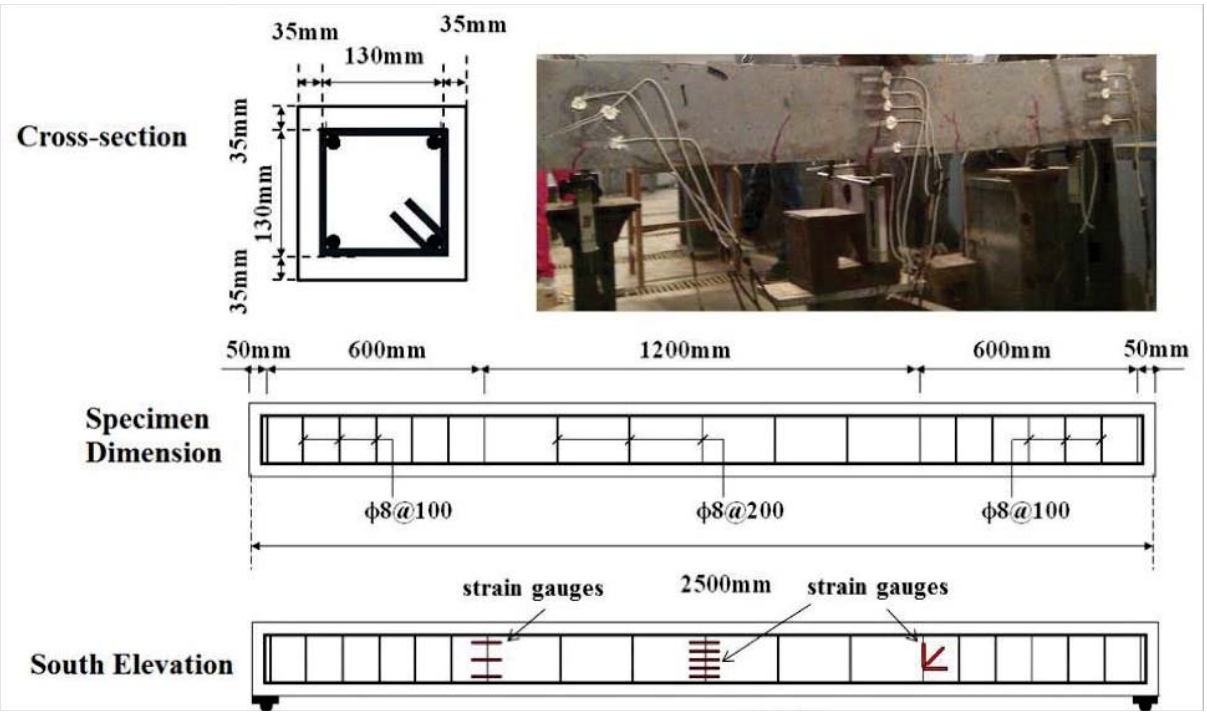

Figure 1 Cross section, column dimension, elevation and instrumentation plan

2.2 Quasi-static bending test set up

As shown in Figure 2, columns were tested under electromechanical servo hydraulic pressure testing machine by displacement control in 3000 kN capacity testing machine [24], with the standard procedures conforming to the Chinese standard GB/T 50081-2002 test method [23]. The 2500 mm long specimen was tested in flexure with a 2400 mm clear span. The column was loaded in three points bending, with the point load located at mid-span as shown in Figure 2(a) for specimen without axial loading and Figure 2(b) for specimen with axial loading. The supported conditions were best described as simply supported with one edge under pure axial load. The simply support (Figure 2(c)) was designed to restrain the lateral movement. The axial loading was applied using hydraulic jacks located axially to the specimen (Figure 2(d)).

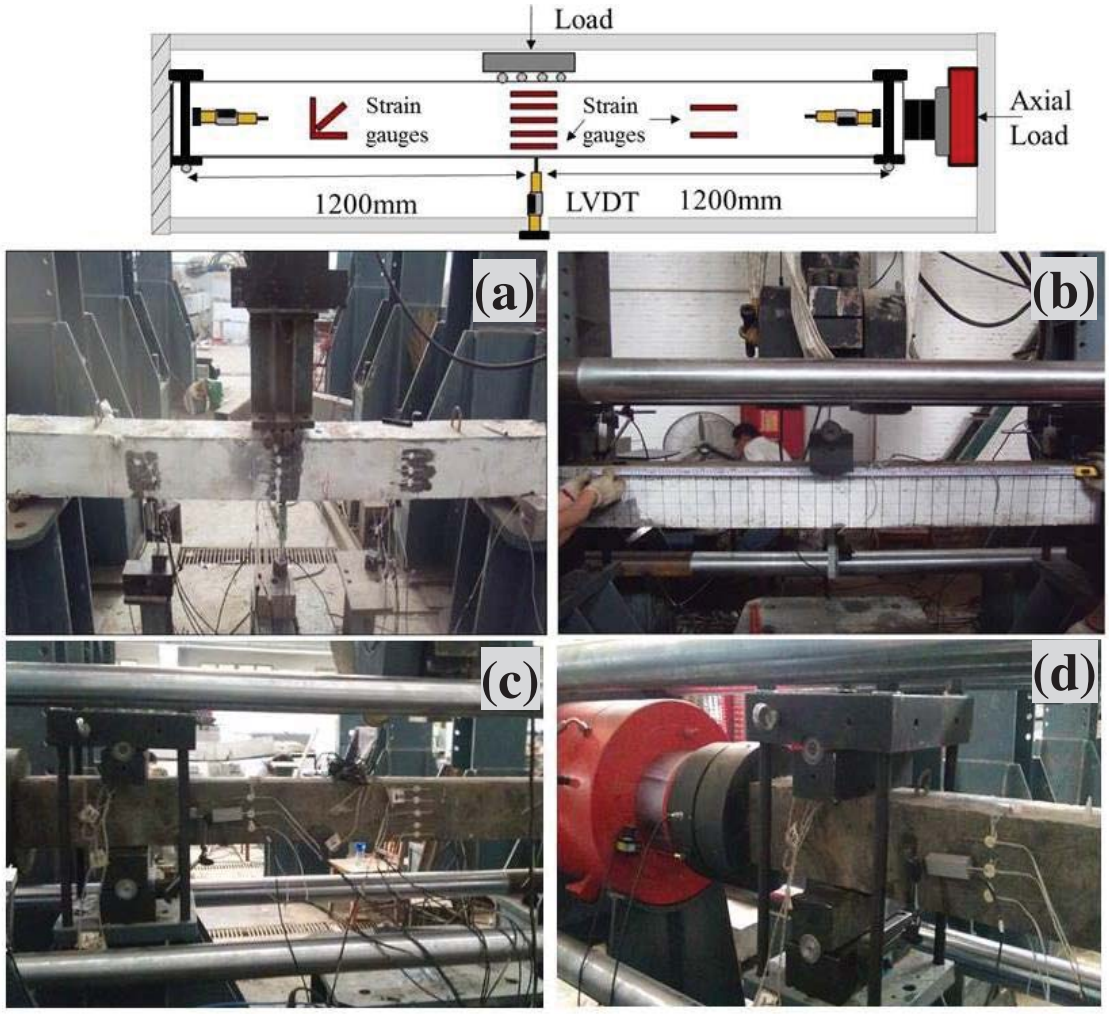

Figure 2 Test set up (a) Testing without axial loading (b) Testing with axial loading (c) Support of specimen (d) Axial loading equipment

Instrumentation for flexural test is shown in Figure 2. LVDT with a stroke of 100 mm was installed to measure the central deflection during the test. Load was applied through displacement control at a speed of 1/1500 of the specimen span length (2400 mm) per minute. In addition strain gauges were installed to obtain strain profile in height direction of column, and hence, curvature of cross section could be determined and then used in Section 3 from the strain profile. The deformations occur when a cross-section is subjected to axial force and bending moment will be planar on elastic regime, and it is customary to assume that the deformations remain planar after yielding has occurred, therefore, the curvature could be determined by using the strain profile results [29].

2.3 Static testing results

Due to the increased tensile capacity of cementitious composite matrix and rack-bridging behaviour of fibre reinforcement, UHPFRC exhibits significant, sustained post cracking flexural tensile capacity prior to crack localization, fibre pull-out, and loss of tensile capacity (Graybeal, 2008). The current section will discuss the flexural behaviour by analysing the experimentally obtained load–displacement curves.

2.3.1 Effectiveness of axial loading

The force-displacement relationships describing non-linear inelastic response of UHPFRC columns with and without axial loading are shown in Figure 4. The bending response of UHPFRC columns is characterized by a pronounced non-linear behaviour due to multi micro cracking and propagation of macro cracks at failure. Two groups of UHPFRC columns were tested and each group contained three curves represented the response at middle of the specimen. First of all, based on the deformation states of the critical section the overall shape of load-displacement curves of UHPFRC columns is primarily characterized as four behaviour regimes: (1) Linear-elastic behaviour; (2) Non-linear inelastic behaviour before macro crack opening; (3) Non-linear behaviour with macro crack opening, and increase in load-bearing capacity; (4) Post-peak behaviour. For regime (1), there was no significant crack pattern or surface appearance observed under the loading. Afterwards, the non-linear phase before macro crack opening (regime 2) was characterized by the presence of multi-micro cracking. Beyond the level of deformations corresponding to macro crack opening, deformations continued to increase with a very slight change in force level, indicating that the crack opening allows a plastic like behaviour to develop. Lastly, regime 4 showed very ductile post peak behaviour after formation of a major crack, with fibres bridging the crack helping the column to sustain load as a crack opened and the fibres were slowly pulled out.

For mid-span load-deflection curves of columns with and without axial loads in Figure 4, at loads below approximately 90 kN (for specimen without axial loads) and 150 kN (for specimen with axial load), the cracks on column were not visible. Significant visible cracking, showed up when loads reached 150 kN and 250 kN for specimens without and with 1000 kN axial loads. Column with axial load application sustained a peak load of 502 kN at a deflection of 24 mm before entering into a softening regime. The column with axial loading exhibited significantly additional load-carrying capacity after initial cracking. Two reasons can be

accounted for this observation. Firstly, axial load application generated an initial compressive stress state within the column, and therefore a large lateral force was required to induce sufficient tensile strain on the column bottom surface and initiate concrete cracking. Secondly, the application of axial load changed boundary condition of the column in the current test setup, when the column was loaded with axial force, and the end restrains could generate compressive membrane effect when column lateral deformation was small, and this effect was beneficial for enhancing column lateral resistance.

From the post failure cracking pattern (Figures 4(a) and 4(b)), it was noticed that one obvious large crack existed for the column without axial loading, and the fibre played the most important role in bridging two crack surfaces. For column with axial load, more severe damage was observed at column mid-span, and this is because the secondary P-Delta effect. Given both columns suffered the same flexural deflection, the axial load generated additional bending moment on the column and thus promoted the mid-span deflection and damage.

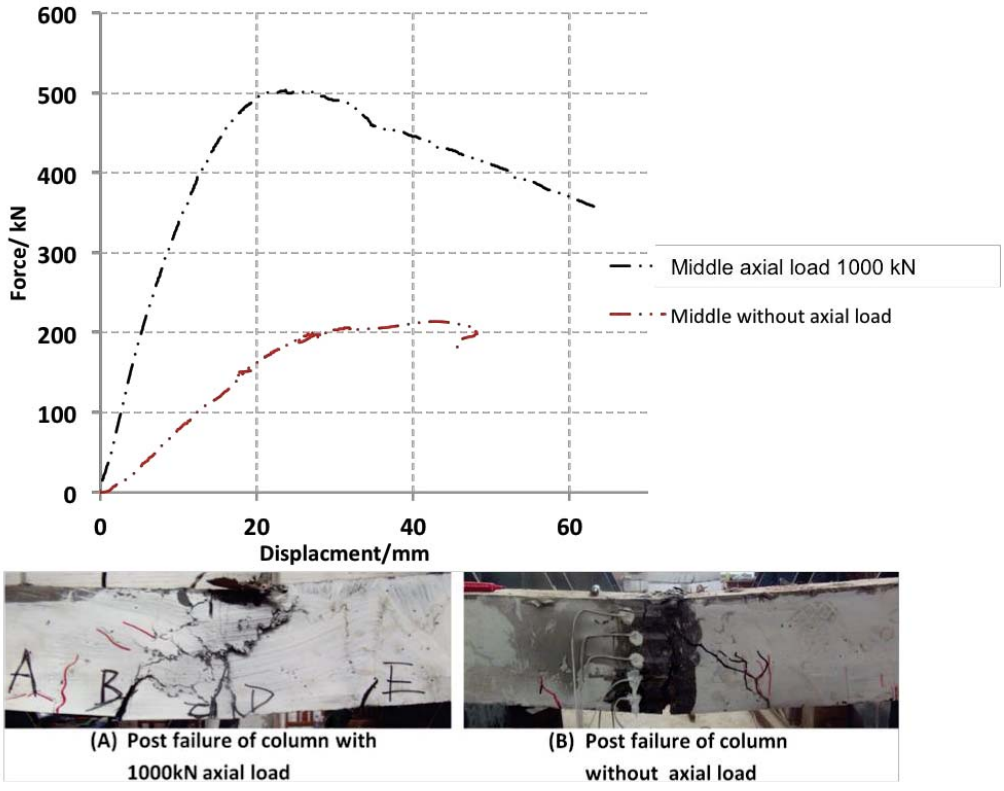

Figure 4 Force-displacement behaviours of UHPFRC columns, post failure crack pattern of UHPFRC column a) with 1000kN axial load and b) without axial load

2.3.2 Comparison with high strength reinforced concrete column

The load-displacement behaviour of HSRC column was observed to be significantly different from UHPFRC column, and the summary of comparison is shown in Table 2. In general, under the same 1000 kN loading, UHPFRC specimen was able to develop approximately 13.4% higher load level over HSRC specimen. Both UHPFRC specimens with/without axial load displayed a very ductile behaviour in Figure 5 where the specimen continued to carry load up to displacement far greater than the displacement corresponding to peak load. For HSRC column, it showed a linear behaviour up to cracking; however, soon after the maximum load (432kN) was reached, a sudden drop in load occurred which was induced by e brittle compressive failure of concrete in contact with the lateral load cell. The lateral load resistance then rebounded due to the contribution from the longitudinal reinforcement.

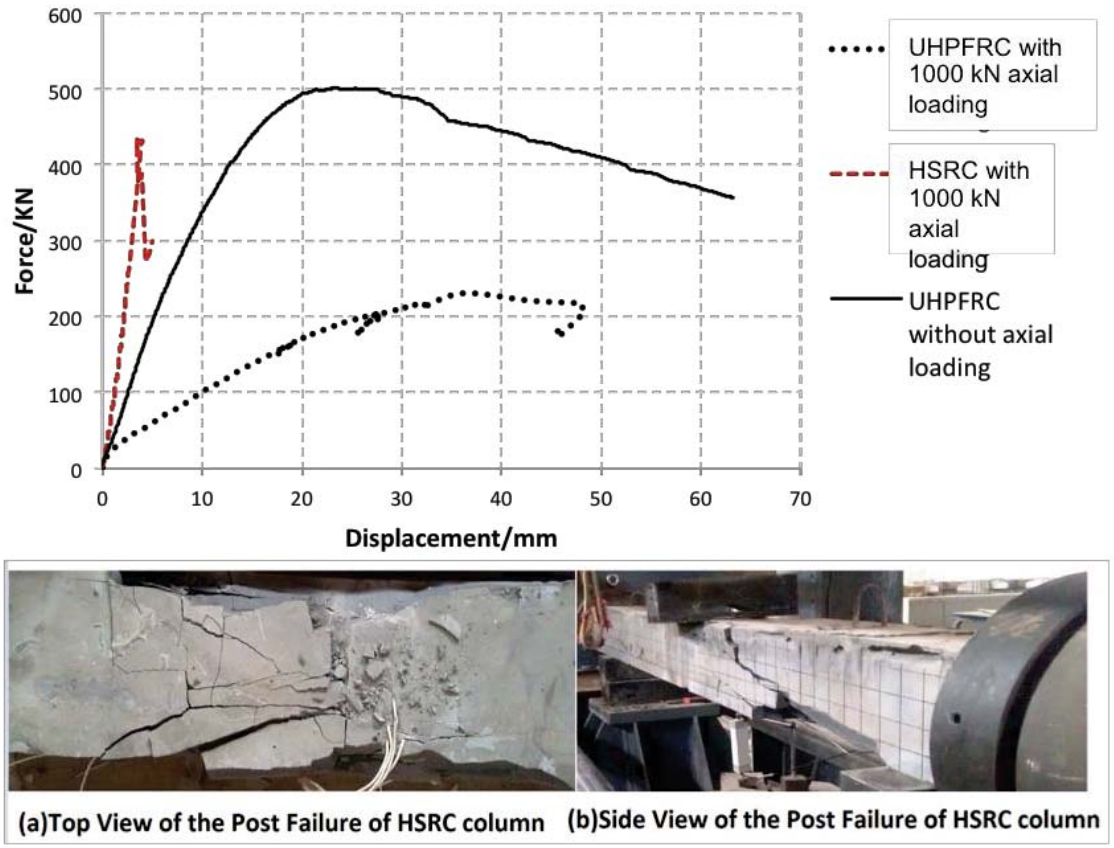

Figure 5 Force-displacement behaviours of HSRC and UHPFRC columns, a) top and b) side view of the post failure crack pattern of the HSRC column

Regarding to post failure photographs of UHPFRC (Figures 4(a) and 4(b)) and HSRC (Figures 5(a) and 5(b)) columns, two distinct failure modes were observed in the tests. HSRC specimen displayed a very brittle behaviour with a catastrophic failure after the peak load was reached. There was no warning before collapse; the specimen lost their integrity and breaking into

several pieces. However, UHPFRC specimens failed in a more ductile manner, in which diagonal cracks at the failure plane were developed, and due to the fibre bridging effect, no fragments were found on UHPFRC columns.

All the above static tests were conducted at the Structures Laboratory at TCU-UA (Tianjin Chengjian University-University of Adelaide) Joint Research Centre on Disaster Prevention and Mitigation. As a summary, the results from three-point bending tests of UHPFRC and HSRC columns are listed in Table 2.

Table 2- Summary of results from three point bending tests

Specimen	Axial loading (kN)	Peak Load	Peak Displacement (mm)	Crack width at Failure (mm)
UHPFRC	0	231	28	7.8
UHPFRC	100	502	21	2.79
HSRC	100	432	4.5	21

3. Structural response using a finite element model

A simplified finite element FE model has been developed to simulate dynamic response of UHPFRC and HSRC columns against blast loads in this section. The structural response along the column was modelled by considering the column to be comprised of a series of segment elements developed based on Timoshenko's beam theory. Timoshenko's beam theory considers both shear deformation and bending deformation as well as rotational inertia, as shown in Equations (1) and (2) and this theory has been demonstrated useful for blast loading problem by previous researchers in the literature (Dragos, Visintin, Wu, & Oehlers, A numerically efficient finite element analysis of reinforced concrete members subjected to blasts, 2014)[25].

$$\frac{\partial M}{\partial x} - Q = -\rho_m I \frac{\partial^2 \rho}{\partial t^2} \tag{1}$$

$$\frac{\partial Q}{\partial x} + q + P_a \frac{\partial \beta}{\partial x} = \rho_m A I \frac{\partial^2 v}{\partial t^2} \tag{2}$$

where M = the applied bending moment, Q = the applied shear force, q = the distributed blast loading acting transverse to the beam, P_a = the column axial load, A = the cross sectional area, I = the moment of inertia of the beam, ρ_m = the mass density of the beam, β = the rotation and ν = the transverse displacement. The FE method solves Equations (1)

and (2) in their weak forms. The governing weak form equation can be expressed in matrix form as:

$$\left(\left[K\right]+P_a\left[K_G\right]\right)\left\{\delta\right\}+\left[M\right]\left\{\ddot{\delta}\right\}=\left\{P\right\} \tag{3}$$

where [K] is the stiffness matrix, P_a is the axial load on column, [K_G] is the geometric stiffness matrix, [M] is the mass matrix, {δ} is the displacement vector, { $\ddot{\delta}$ } is the acceleration vector, and {P} is the load vector. Equation (3) is solved using Newmark method at each time interval. It should be noted that in Equations (2) and (3) P_a is negative, thereby, reducing stiffness of column via P-Δ effect.

For solving displacement at each time step of Equation (3), Newmark's method was implemented. By using this approach, the solution process is step by step in nature, and this implies that at each discrete time intervals within the solution time domain, the stiffness matrix [K] and mass matrix [M] in Equation (3) which both in global level need to be specified first. To achieve a high accuracy while maintain an appropriate level of calculation efficiency, a three node isoperimetric beam element which maps into axis system (ξ) ranging from -1 to +1 having a quadratic shape functions is adopted. At each time integral, the mass and stiffness matrices are determined at element level by using the principle of virtual work and then assembled them to the global level by undertaking the Gauss quadrature (Dragos, Visintin, Wu, & Oehlers, A numerically efficient finite element analysis of reinforced concrete members subjected to blasts, 2014). The stiffness matrix and mass matrix at the element level can be shown in Equations (4) and (5).

$$\left[K\right]=\int_{-1}^{1}\left[B\right]^{T}\left[D\right]\left[B\right]\left|J\right|\partial\xi \tag{4}$$

$$\left[M\right]=\int_{-1}^{1}\left[N_m\right]^{T}\left[R_m\right]\left[N_m\right]\left|J\right|\partial\xi \quad \text{where} \tag{5}$$

$$\left[R_m\right]=\begin{bmatrix}\rho_m A & 0\\ 0 & \rho_m I\end{bmatrix} \tag{6}$$

where [B] is the strain displacement quadratic shape matrix, [N_m] is the quadratic shape matrix for the mass matrix, |J| is the Jacobian determinant which is equal to half the length of the beam element, [D] are the elasticity matrix, ρ_m is density, A is cross sectional area and I is moment of inertia.

In order to determine the stiffness matrix at each time interval, the non-linear curvature dependent flexural rigidity and linear shear rigidity need to be known for calculating the elasticity matrix [*D*]. For determining flexural rigidity, moment curvature relationships are directly applied for loading phases. For unloading phases, it is assumed that the unloading curve has a slope as the same as the elastic region of moment curvature relationship. For shear rigidity, a linear shear stress strain theory is applied as shown in Equation (4). This linear shear strain relationship is considered sufficient because the present study is dealing for the members with large span to depth ratio, where failure is usually governed by flexural damage.

$$Q = KA_w\sigma_{xz} = KA_wG\gamma_{xz} \tag{7}$$

where σ_{xz} is shear stress, γ_{xz} is shear strain, G is the shear stiffness and A_w is the cross sectional area. Timoshenko beam theory relies on the assumption that the distribution of shear stress over the cross section is a constant. To account for the fact that the distribution of shear stress along the depth of the section is parabolic, Equation (7) contains a correction factor, K, where $K=\pi^2/12$ for rectangular cross sections [26].

It can be seen from above, to be able to model the structural response of a member subjected to a blast load using ab 1D FE model requires to determine moment curvature relationship of a member. As discussed in the previous section that, many previous studies, have not adequately characterized UHPFRC resistance model. In the present research it is achieved towards derivations of resistant capability of UHPFRC by using static testing. By taking into account mechanics of concrete cracking and softening behaviour, flexural response of UHPFRC columns can be derived. Therefore, following up the next section, research is devoted to simulating UHPFRC specimen under different blast experimental tests by incorporating the derived moment curvature relationships into the 1D FE model.

4. Blast experiments

The experimental results described below were obtained from a series of tests carried out by PLA University of Science and Technology, Nanjing, China. The series of tests consisted of three UHPFRC specimens and two HSRC specimens. The experimental results were used to calibrate and validate the 1D FE simulation code that aimed at stimulating large-scale UHPFRC and HSRC events and better designing protective structures.

The same UHPFRC and HSRC specimens used in the Section 2.1 are used in this section. The detailed charge weights, scaled distance, specimen geometry of the experiment setup are provided in Table 3.

Table 3 - Summary of results from three blast tests with various charge weights

Column Name	Description	Axial Force (KN)	Scaled distance ($m/kg^{1/3}$)	TNT equivalent charge weight (kg)	Peak Pressure (MPa)
U1A	UHPFRC	0	1.5	1	1.86
H1B	HSRC	1000	0.75	8	Faulty value
U1B	UHPFRC	0	0.58	17.5	29.08
U1A	UHPFRC	0	0.46	35	43.1

4.1 Experimental set-up and data acquisition

The standoff distance between charge centre and centre of specimen was 1.5 m. The support apparatus used in the blast program is shown in Figure 5(a). The galvanized pipe frame was 2.6 m high and 2.5 m wide. The base of the frame was bolted to the concrete ground slab, 4 galvanized pipes more were also fixed between the top and bottom of the frame to stabilize it. A specified steel frame with dimensions 2600 mm × 400 mm × 1000 mm was built with a clamping system to ensure that the test specimens could be firmly placed inside the frame for preventing the column from uplifting as shown in Figure 5(b). After placing the column between the supported frames, all the data acquisition devices should be connected and checked for proper functioning.

The data acquisition devices used during the blast experiments included: Linear Variable Displacement Transducers (LVDTs), Pressure Transducers and Digital Cameras. Prior to the blast test, the whole frame with specimen and LVDTs was placed in a horizontal position and then lowered to the ground level as shown in Figure 5(c). This was done to prevent damage to the frame and connected apparatuses caused by the blast load. For testing the specimen under axial loading condition, one support was connected with the hydraulic jack as shown in Figure 5 (d), which was installed and buried beneath the ground at one side of the test pit. Before testing the column, the axial load was slowly and gradually increased to 1000

kN, when the desired axial load was reached, the pneumatic jack maintained a constant applied load to make sure the axial load condition applied to the column remained constant during the blasts.

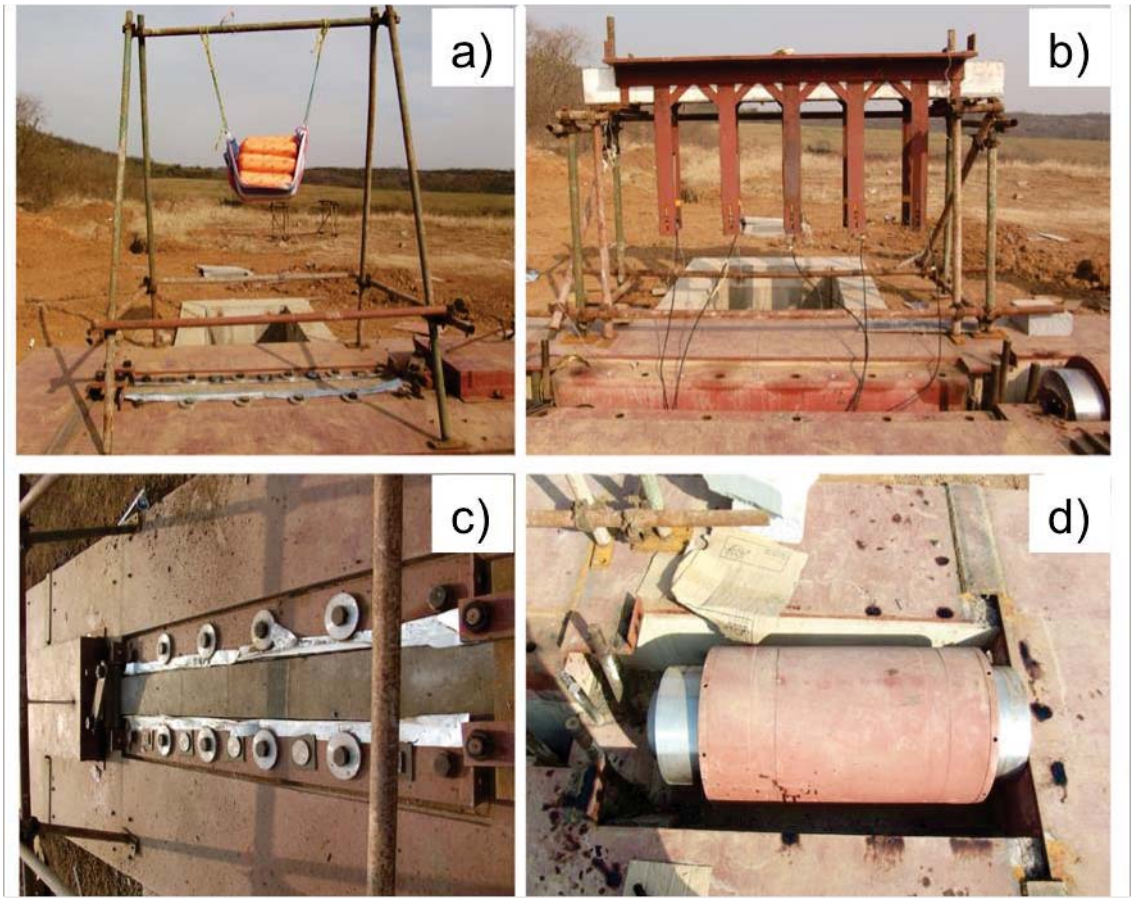

Figure 5: Blast test setup

4.2 Experimental results

In this section a synopsis of the experimental results of pressure-time history is presented. According to TM 5-1300 (superseded by UFC 3-340-02 [27]), for a structure subjected to a blast wave, the load is applied to the surface as a time-dependent boundary load, where the pressure is often simplified as a triangular pressure-time curve. For all of the events the incident pressures were measured from the point of the greatest interest to be located 1.5 m directly beneath the charge, and the experimental results are compared with the empirical pressure predicted by UFC 3-340-02 [27]. Cylinder emulsion explosive charge weights of 1.4 kg to 48 kg were used in the test, and for convenience, it was referred as an equivalent weight of TNT. The nominal TNT equivalence factor for emulsion explosive charge is 0.71. The TNT equivalent explosive charge weights of 1 kg, 8 kg, 17.5 kg and 35 kg were placed at

1.5 m height above the specimens. The summary of the experimental and prediction results of three different charge weights is shown in Table 3.

The incident pressure was successfully recorded for all the events except the case with 8 kg TNT equivalence. Figure 6 shows the time incident pressure history for the three cases. As expected, the greater the charge weight tends to cause the larger reflected pressure. In general, it can be observed that the average peak overpressure and impulse recorded have a dramatic increase from 1 kg to 17.5 kg and finally 35 kg explosive loading. Specimen U1A with charge weight 1 kg loading obtained a peak pressure of 1.86 MPa. As a result of charge weight of 17.5 kg, the peak pressure increased to 29.01 MPa. Finally the largest peak pressure occurred with charge weight 35 kg, the highest peak pressure was 43.1 MPa.

Plotted against the experimental pressure in dash line is the empirical pressure predicted by UFC 3-340-02 [27] with linear decaying trend. The negative pressure measured after the positive phase of the impulse was neglected. It was found that UFC 3-340-02 [27] yielded smaller peak reflective pressure as compared with experimental observations. These results indicated that reflected pressure is highly dependent on experimental variations and environmental conditions (i.e., charge shape, charge angle, wind velocity, humidity, etc.), and the difference may be attributed to the limitations of this simplified UFC method lies in neglecting the true physics of the blast wave – structure interaction phenomena in that it assumes the load – time history is applied to all parts of the surface at the same time [29]. Nevertheless, the approximation of the blast results is still within a reasonable tolerance range, thus the current prediction will be further used into the 1D FE analysis in the next section.

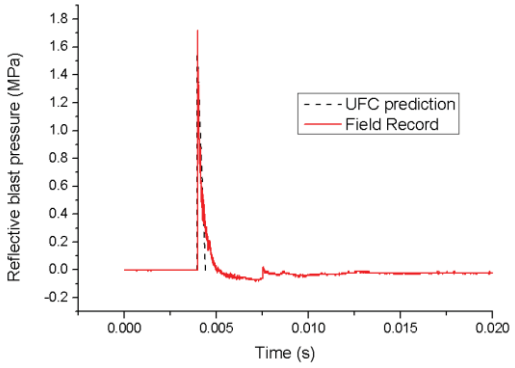

1 kg TNT equivalence

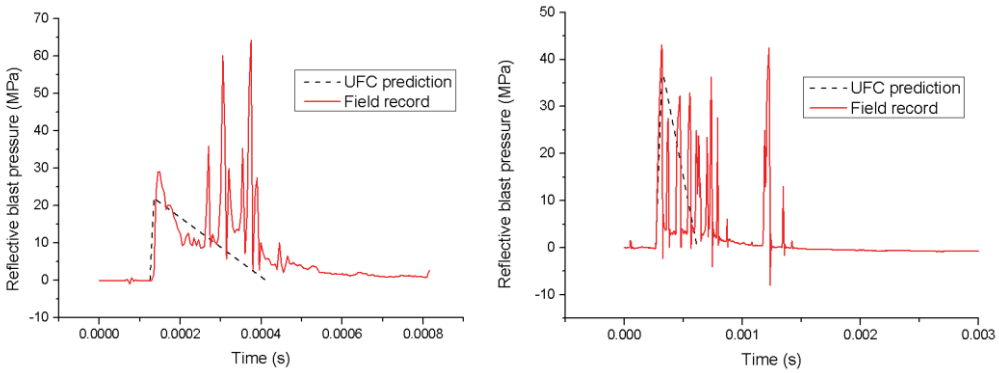

17.5 kg TNT equivalence 35 kg TNT equivalence

Figure 6 Pressure time histories of experimental data and UFC prediction

5. Validation of the 1D FE Model

To evaluate the reliability of the 1D FE model, the results of FE model are compared with the measured displacement histories obtained from UHPFRC and HSRC columns under blast testing. There are two main input data that need to be defined first before running the program, the blast loading and structural material properties. As discussed previously, the approximation of Pressure-Time histories by using UFC 3-340-02 [27] shown in Section 4.2 are within the acceptable tolerance range; thus in the FE simulation, the blast load applied to the surface as a time-dependent boundary load was considered as an idealized triangular Pressure-Time history for the analysis and solution procedures. When considering the material properties as the input data, in order to obtain the moment curvature relationship from the experimental results, it is necessary to transform the load to moment and to determine the curvature of the model. Individual gauges were used until their readings became unreliable due to cracking in the underlying concrete. The process required comparing the pressure time histories produced from the 1D FE model and the experimental results obtained from the LVDTs, which were attached to measure the central deflection of the column. In the modelling of support, because there is no special element used to relieve the uplift forces during rebound, for this reason, in the comparison process between modelling and test results, the deflection and reaction force time histories are only presented up to the first peak.

The mid-span displacement time histories of UHPFRC and HSRC columns against blast loading from the experiment are presented in Figure 7 to Figure 9 together with the calibrated

FE model simulation results. In the first phase of validation as shown in Figures 7 and 8, the same UHPFRC columns against 1 kg and 17.5 kg charge weight were analysed under different levels of axial loads. Generally, the FE model curve shows a good agreement with the experimental results up to the peak response. Although there was a slight discrepancy between the FE and experimental data at the peak displacements, the magnitude of the discrepancy was less than 10% for charge weight 1 kg and 20% for charge weight of 17.5 kg, respectively. Thus it is believed that the results obtained from the 1D FE model are reasonably accurate. It was noted that there was a better agreement between the peak displacements calculated by the 1D FE model in the blast cases, which had the smaller level of axial load. While the largest discrepancy between the peak displacements predicted by the FE model and the experimental data was as high as 17% in the case of a 1000 kN axial load and a transverse blast loading with a peak pressure of 29.01 MPa.

Figure 9 shows further validation of the results obtained from UHPFRC and HSRC columns. It focuses on predicting both UHPFRC and HSRC columns under the same axial and blast loading condition. As shown in the figure, the period of oscillation predicted by the 1D FE model also has a good agreement with the period of the column determined from the experimental data for both UHPFRC and HSRC columns. However, the maximum deflection discrepancy between the FE simulation and the experimental results of HSRC column was 18.6%. This may be attributed to both the inability of the material model developed from the previous static tests in the 1D FE model to capture the hysteretic behaviour of HSRC column and the idealization of the blast pressure; thereby it needs to highlight the potential underestimation of the results predicted by FE simulation for HSRC column in this section.

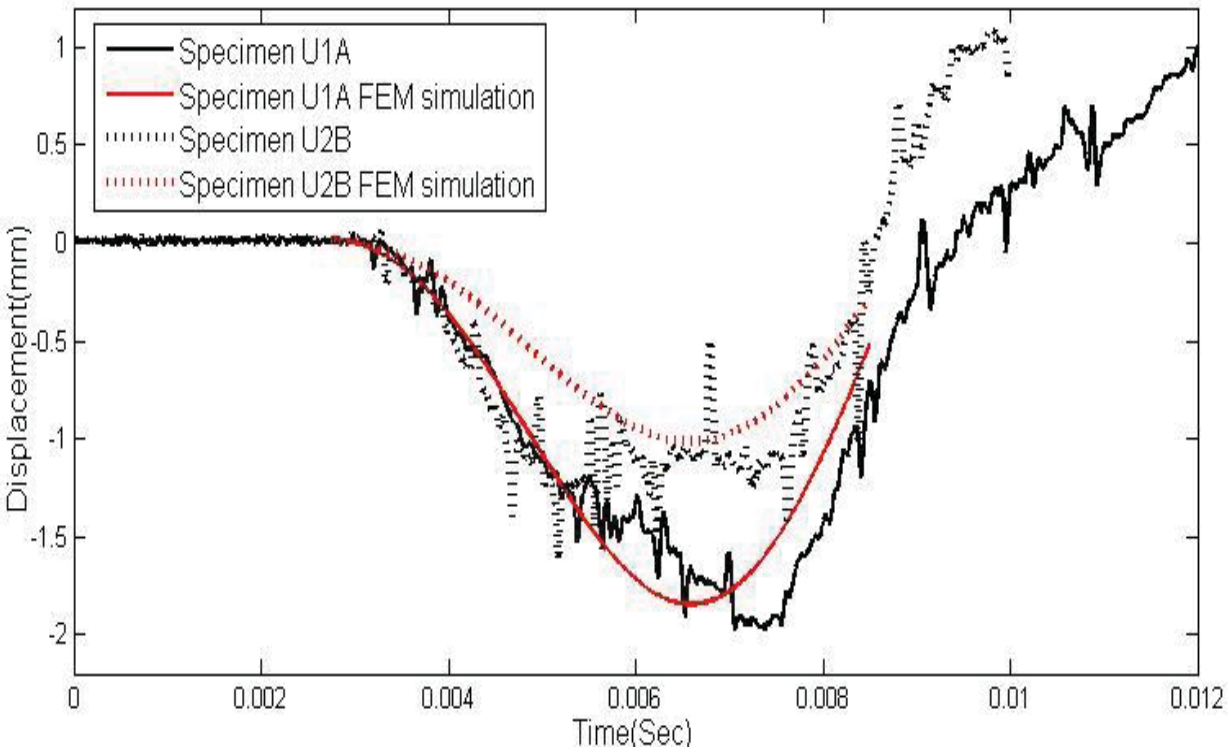

Figure 7 Deflection time histories of experimental data and FE prediction of UHPFRC columns under 1 kg charge weight

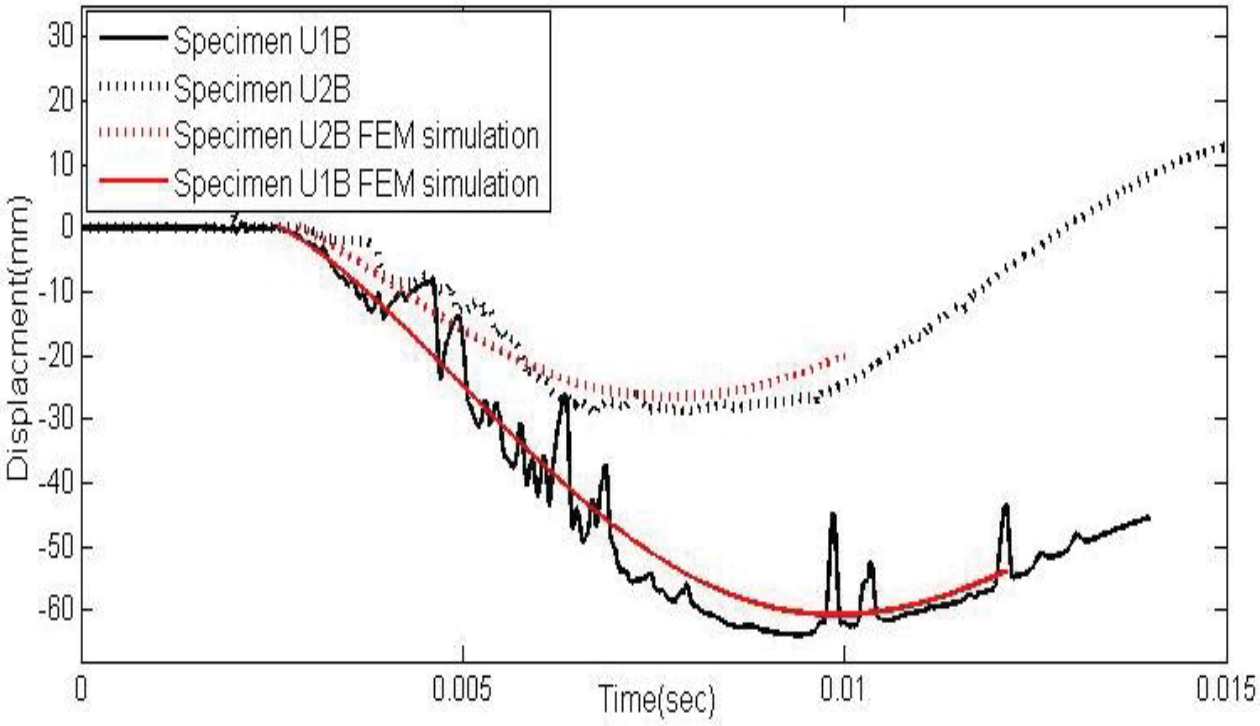

Figure 8 Deflection time histories of experimental data and FE prediction of UHPFRC columns under 17.5 kg charge weight

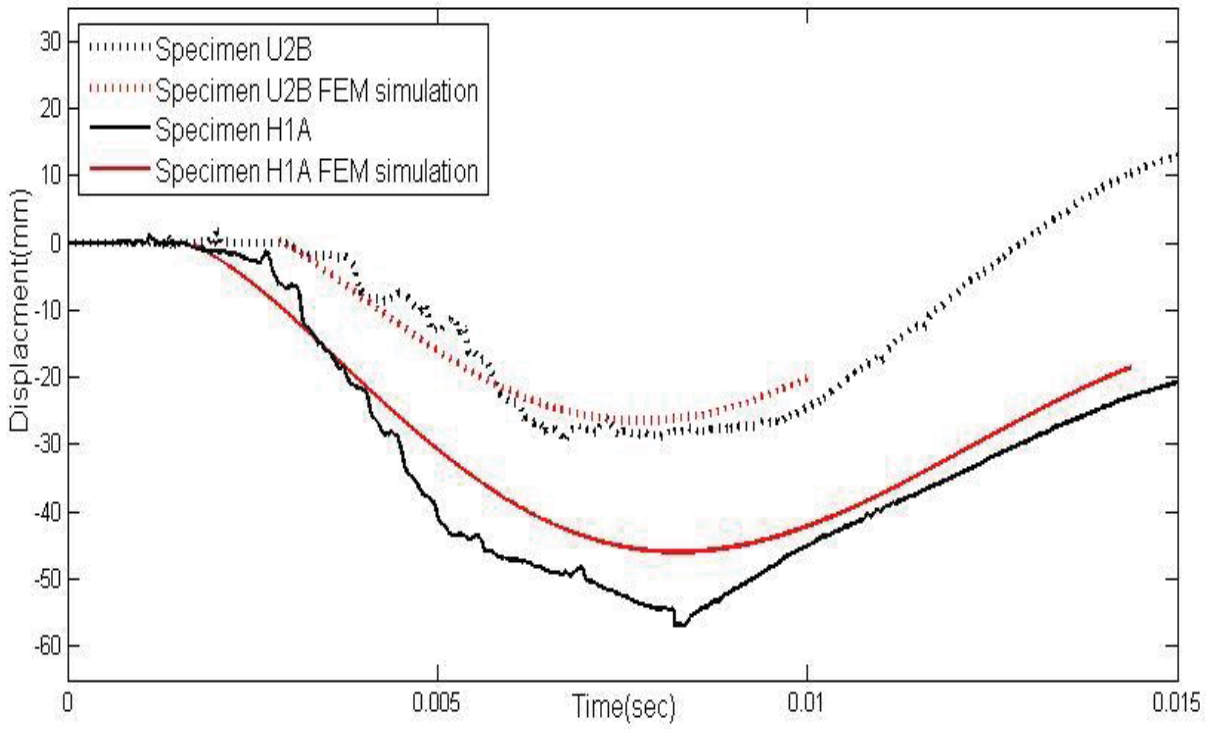

Figure 9 Deflection time histories of experimental data and FE prediction of UHPFRC and HSRC columns under 17.5 kg charge weight

For comparison purposes, the peak mid-span displacements from both experimental and FE simulation are shown in Table 4. Generally, the FE simulation results follow the experimental results closely; the discrepancy of the results was less than 20% from the measured peak displacements. The peak displacement calculated by the 1D FE model was slightly smaller. One possible reason is that the blast loading shapes on the structures has been simplified into a triangular shape based on the UFC 3-340-02 [27], and hence, it under estimates shock velocity, pulse duration and the time to the end of impulse.

Table 4-Validation of the 1D FE model with experimental program

Specimen	Charge weight (kg)	Axial load (KN)	Experimental maximum deflection (mm)	FEM modelling max deflection (mm)	Error %
U1A	1	0	1.96	1.84	5.1
U1B	17.5	0	63.74	59.2	7.1
U2A	1	1000	1.14	1.04	8.7
U2B	17.5	1000	29.27	24.3	17
H1A	17.5	1000	56.04	45.6	18.6

6. Application of the 1D FE model for rest of columns

During the experimental testing, due to the recording system malfunction, the displacement data was not recorded for the specimen under charger weight of 8 kg and 35 kg. With the FE model calibrated and validated against the experimental data in the previous section, it was then possible to predict their response using the validated FE model for different charge weights. The previous experimental peak overpressure, impulse and overpressure duration were used as the input data and the effects of adding external axial loading can be further studied.

Figures 10 and 11 present the deflections of UHPFRC and HSRC specimens generated under charge weights 8 kg and 35 kg loading, respectively. It is obvious that the curves are quite similar to the previous discussed responses where the data of HSRC and UHPFRC columns without axial loading has similar displacement magnitudes, and UHPFRC column with 1000 kN axial loading has the smallest magnitude of displacement.

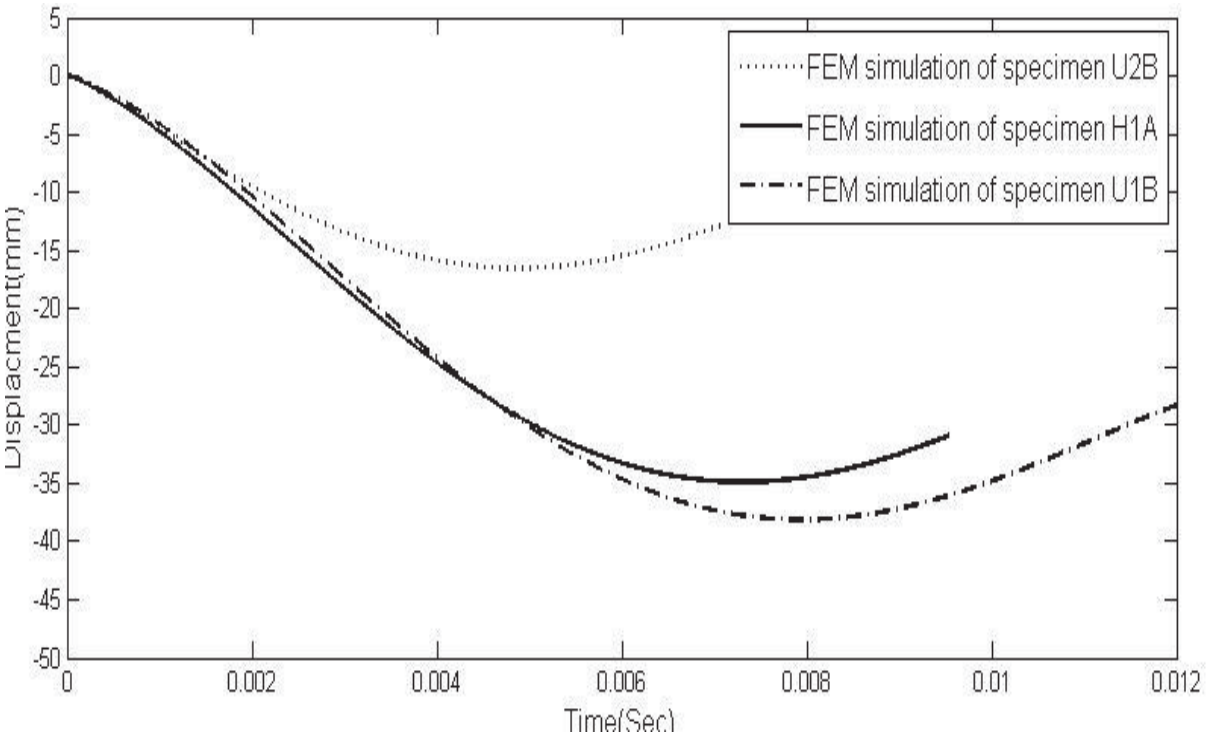

Figure 10 Deflection time histories of FEM prediction of UHPFRC and HSRC columns under 8 kg charge weight

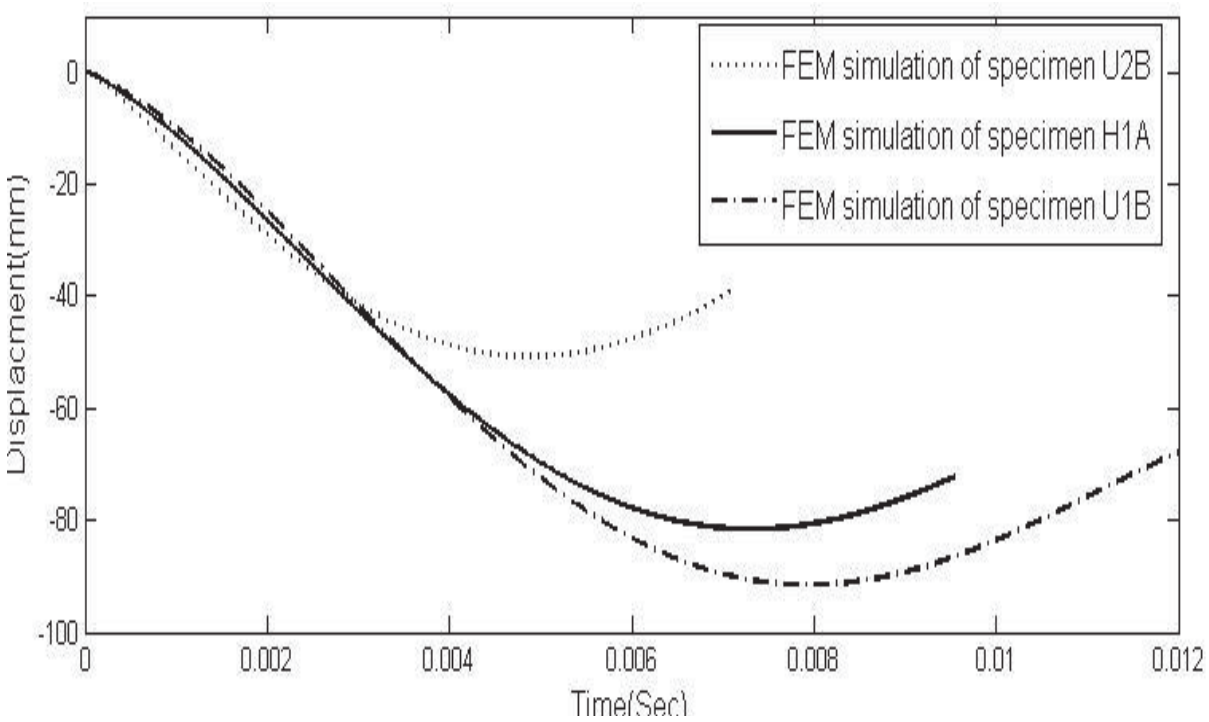

Figure 11 Deflection time histories of FEM prediction of UHPFRC and HSRC columns under 35 kg charge weight

Comparing with the average deflections of U1B and U2B in Figure 10, the average displacement of U2B is approximate 57% less than that for the U1B as axial loads can effectively reduce the mid-span deflections. Comparing the results of U2B with H1A in Figure 11, it is obvious that with the steel fibre and magnitude of the axial loading, it dramatically increases the blast resistance. Also, U2B specimen performs extremely well in the 35 kg blast, in which it has the smallest deflection magnitude (48 mm). HSRC column H1A with 1000 kN axial loading and data of UHPFRC column U2B without axial loading display a similar peak displacement of 81 mm and 87 mm, respectively.

7. Conclusions

This study achieves the aims of characterizing response of HSRC and UHPFRC columns through both static and dynamic analysis. The resistance deflection curves of UHPFRC columns with and without axial loads have been studied by using a quasi-static bending test, and the dynamic response of UHPFRC columns under blast loads have been simulated using the 1D FE model. The study leads to the following conclusions:

- Static testing results show that addition of axial loading produces enhancement of flexural properties of UHPFRC columns.

- The computational efficient 1D FE model was validated by simulating dynamic response of columns against blasts and the simulated results had a good agreement with the experiment data.
- The validated 1D FE model developed based on Timoshenko's beam theory could be used to predict the behaviour of UHPFRC columns under blast loads.

Acknowledgements

The research presented in this paper jointly supported by The National Basic Research Programme (2015CB058002), General Projects in Tianjin Research Program of Application Foundation and Advanced Technology (13JCYBJC39100), and the ARC Discovery Grant DP140103025, is gratefully acknowledged.

References

[1] S. Barnett, J. Lataste, T. Parry, S. Millard and M. Soutsos, "Assessment of fibre orientation in ultra high performance fibre reinforced concrete and its effect on flexural strength," *Materials and Structures*, vol. 43, p. 1009–1023, 2010.

[2] K. Habel, M. Viviani, E. Denarie and E. Bruhwiler, "Development of the mechanical properties of an ultra-high performance fiber reinforced concrete (UHPFRC)," *Cement and Concrete Research*, vol. 36, pp. 1362-1370, 2006.

[3] K. Habel and P. Gauvreau, "Response of ultra-high performance fiber reinforced concrete (UHPFRC) to impact and static loading," *Cement & Concrete Composites* , vol. 30, pp. 938-946, 2008.

[4] K. Habel, E. Denarie and E. Bruhwiler, "Experimental investigation of composite ultra-high-performance fiber-reinforced concrete and conventional concrete members," *ACI structural journal*, Vols. no.104-s11, pp. 93-101, 2007.

[5] S. Astarlioglu and T. Krauthammer, "Response of normal-strength and ultra-high performance fiber-reinforced concrete columns to idealized blast loads," *Engineering structures* , vol. 61, pp. 1-12, 2014.

[6] V. Bindiganavile, N. Banthia and B. Aarup, "Impact response of ultra-high strength fiber reinforced cement composite," *ACI materials journal* , Vols. no.99-M55, pp. 543-548, 2002.

[7] N.-H. Yi, J.-H. J. Kim, T.-S. Han, Y.-G. Cho and J. H. Lee, "Blast resistant characteristics of ultra-high strength concrete and reactive powder concrete," *construction and building materials* , vol. 28, pp. 694-707, 2012.

[8] K. Habel, M. Viviani, E. Denarié and E. Brühwiler, "Development of the mechanical properties of an ultra-high performance fiber reinforced concrete (UHPFRC)," *Cement and Concrete Research* , vol. 36, no. 7, pp. 1362-1370, 2006.

[9] D. Lavenhagen, "A numerical assesssment of direct shear behaviour in concrete," University of

Florida, Florida, 2012.

[10] E. Fehling, M. Schmidt, T. Teichmann, K. Bunje, R. Bornemann and B. Middendorf, "Entwicklung,Dauerhaftigketi und Berechnung Ultrahochfester Betone(UHPC):Forschungsbericht DFG FE497/1-1," Kassel University Press, 2004.

[11] B. Graybeal, "Flexural Behavior of an Ultrahigh-Performance Concrete I-Girder," *Journal of Bridge Engineering, ASCE*, vol. 13, pp. 602-610, 2008.

[12] J. Wuest, E. Denarié and E. Brühwiler, "Model for predicting the UHPFRC tensile hardening response," *Second International Symposium on Ultra High Performance Concrete*, vol. 10, no. 10, pp. 153-160, 2008.

[13] S. Kang, Y. Lee, Y. Park and J. Kim, "Tensile fracture properties of an Ultra High Performance Fiber Reinforced Concrete (UHPFRC) with steel fiber," *Composite Structures*, vol. 92, pp. 61- 71, 2010.

[14] E. Denarié, K. Habel and E. Brühwiler, "Structural Behavior of Hybrid Elements with Advanced Cementitious Materials (HPFRCC)," in *High Performance Fiber Reinforced Cement Composites (HPFRCC-4)*, RILEM, Ann Arbor, Mich, 2003.

[15] P. Rossi, A. Arca, E. Parant and P. Fakhri, "Bending and compressive behaviors of a new cement composite," *Cem. Concr. Res*, vol. 35, no. 1, pp. 27-33, 2005.

[16] L. Mao, S. Barnett, D. Begg, G. Schleyer and G. Wight, "Numerical simulation of ultra high performance fibre reinforced concrete panel subjected to blast loading," *International journal of impact engineering* , vol. 64, pp. 91-100, 2014.

[17] T. Ngo, P. Mendis and T. Krauthammer, "Behaviour of ultra high strength prestressed concrete panels subjected to blast loading," *Journal of Structural Engineering*, vol. 133, p. 1582–1590, 2007.

[18] C. Wu, D. Oehlers, M. Rebentrost, J. Leach and A. Whittaker, "Blast testing of ultra-high performance fibre and FRP-retrofitted concrete slabs," *Engineering Structures*, vol. 31, p. 2060–2069, 2009.

[19] S. Millard, T. Molyneaux, S. Barnett and X. Gao, "Dynamic enhancement of blast-resistant ultra high performance fibre-reinforced concrete under flexural and shear loading," *International journal of impact engineering* , vol. 37, pp. 405-413, 2010.

[20] M. Rebentrost and G. Wight, "Investigation of UHPFRC Slabs Under Blast Loads," in *Proceedings, Ultra-High Performance Fiber Reinforced Concrete* , 2009.

[21] S. Astarlioglu and T. Krauthammer, "Response of normal-strength and ultra-high-performancefiber-reinforced concrete columns to idealized blast loads," *Engineering Structures*, vol. 61, pp. 1-12, 2014.

[22] J. Dragos, P. Visintin, C. Wu and D. Oehlers, "A numerically efficient finite element analysis of reinforced concrete members subjected to blasts," *International journal of protective* structures , vol. 5, pp. 65-82, 2014.

[23] China Standard, "GB/T, 50081-2002 Method for testing mechanical properties of normal concrete," Beijing, China, 2002.

[24] X. J and W. C, “Experimental Study on Blast Resistance of Ultra High Performance Fiber Reinforced Concrete Columns,” 2014.

[25] C. Wu and H. Sheikh, “A finite element modelling to investigate the mitigation of blast effects on reinforced concrete panel using foam cladding,” *international journal of impact engineering* , vol. 55, pp. 24-33, 2013.

[26] T. Krauthammer, A. Assadi-Lamouki and H. Shanaa, “Analysis of Impulsively Loaded Reinforced Concrete Structural Elements – I. Theory,” *Computers & Structures*, vol. 48, no. 5, pp. 851-860, 1993.

[27] Unified Facilities Criteria (UFC) 3-340-02, DoD Minimum Antiterrorism Standards for Buildings, Department of Defense, US, 2013.

[28] A. Remennikov, “A Review of Methods for Predicting Bomb Blast Effects on Buildings,” *Journal of Battlefield Technology*, vol. 6, no. 3, pp. 5-10, 2003.

[29] I. H. Yang, C. Joh and B.-S. Kim, “Structural behavior of ultra high performance concrete beams subjected to bending,” *Engineering structures*, vol. 32, no. 11, pp. 3478-3487, 2010.

Chapter 4
Conclusions & Future Research

Conclusions

In this Chapter, the main conclusions drawn from the work presented in this thesis are summarized.

In Chapter 2 of the thesis, a numerical method for the dynamic analysis of reinforced concrete members subjected to air blast loadings was presented in this study. The proposed method adopts the Single-Degree-of-Freedom (SDOF) approach, where two loosely coupled SDOF systems are considered to model the flexural and direct shear mode of structural response. The proposed procedure is implemented in a computer programming language and the results are validated using experimental data from a number of explosive tests. The numerical results compare very well with experimental data. Afterwards, a series of parametric studies have been conducted for the pressure-impulse curves of the direct shear failure model of RC members under an external blast loading and finally equations have been proposed for quickly evaluating which offer a valuable information in preliminary design for the RC members against blasts. Regarding to the second paper of the research, a FEM based model has been developed for simulating the shear transfer across the reinforced concrete members and this model has been validated with the results of initially un-cracked push-off test specimens under quasi-static loading. This study has provided strength and load to slip characteristics of push-off specimens in a complete analysis of RC members under direct shear loads. The simulation is essentially static but the proposed shear strength and shear to slip relationship models can be used for dynamic conditions.

In Chapter 3 of the thesis, two papers address the blast-resistant capacities of UHPFRC and high strength reinforced concrete (HSRC) columns. The results showed that they have outstanding blast-resistant capacities. The conclusions of this experimental program are summarized as the UHPFRC columns have much higher blast resistance than the HSRC columns embodied in lower mid-span deflection and reduction of concrete spalling in an average sense. The last part of the chapter is focusing on presenting the results of numerical investigations that are conducted in order to examine the blast resistant capabilities of HSRC

and UHPFRC columns. The resistance deflection curve of HSRC/UHPFRC columns with and without axial loads has been studied by using a quasi-static bending test, and the dynamic response of UHPFRC columns under blast loads are simulated by using a one-dimensional (1D) finite element model (FEM). The dynamic response of the test columns under blast loading, as predicted by 1D FEM, shows that an accurate numerical simulation of the experimental observations is possible using the present FE numerical method.

Future Research

In the view of the shear failure cracks captured in the blast investigation, it will be very useful to study direct shear behaviour of steel fibres combination with steel stirrups in UHPFRC members. More push off tests can be conducted for UHPFRC, in order to develop better models for the direct shear behaviour of this composite. While the push off experiment program can be developed for analysing shear strength and slip of UHPFEC members, investigation into using a finite element code together with material model for UHPFRC should be completed to see if any improvements can be made in the behaviour of the push-off specimens. Introducing UHPFRC material properties into the new FEM model should also be investigated and results confirmed with test data to see if good results can be accomplished. Based on the validated model, a new parametric study can be performed in the shear transfer of fibre reinforced concrete, and based on the simulated results, equations for estimating the shear strength and shear stress to slip relationships of UHPFRC can be derived as a preliminary design tool for evaluating the shear transfer in structure design works.

Further research also can be carried out for incorporating the shear resistance function of UHPFRC members discussed in the previous paragraph into the dynamic analysis. The single degree of freedom (SDOF) method, has not been extended to account for, failure mechanisms of UHPFRC members such as direct shear failure. Thus new SDOF approach can be developed which analyses the direct shear and flexural responses separately using two differential equations for UHPFRC members. In further research, both the moment-curvature flexural behaviour and the direct shear behaviour of UHPFRC members can be incorporated into a numerically efficient one dimensional finite element model, utilizing Timoshenko Beam Theory, to determine the member and direct shear response of UHPFRC members subjected to blasts. Finally, by following the investigation of the direct shear response of UHPFRC members subjected to blasts using the 1D FEM, simplified equations can be developed to

efficiently determine direct shear PI curves for such members. Such equations would be very valuable for the purposes of preliminary analysis and design.